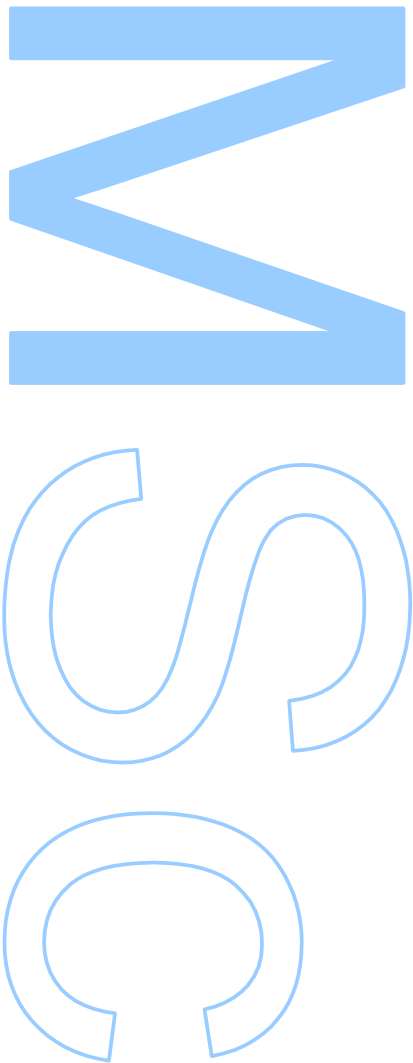
Customization of Thermal Expansion in Nanowires

Sofia Gonçalves
Mestrado Integrado em Engenharia Física
Departamento de Física e Astronomia
2021

Orientador
Dra. Arlete Apolinário, Faculdade de Ciências

Coorientador
Dr. João Horta Belo, Faculdade de Ciências



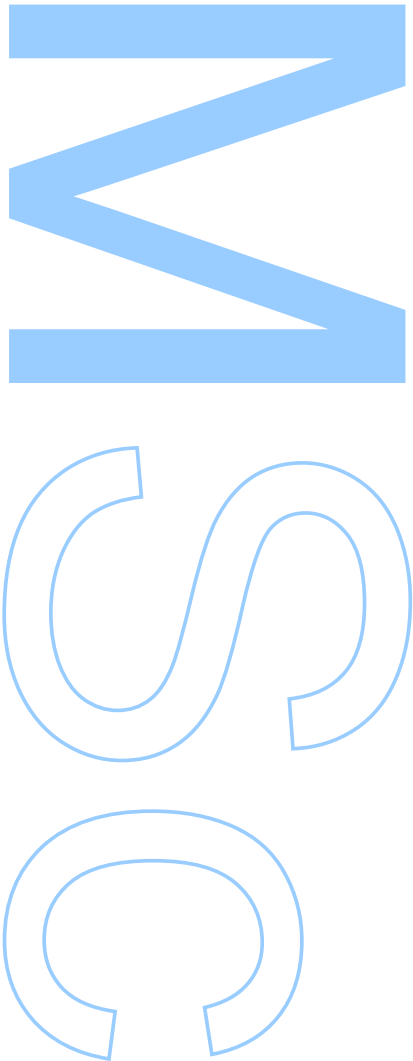
U.PORTO

FACULDADE DE CIÊNCIAS
UNIVERSIDADE DO PORTO

Todas as correções determinadas pelo júri, e só essas, foram efetuadas.

O Presidente do Júri,

Porto, _____/_____/_____



UNIVERSIDADE DO PORTO

MASTERS THESIS

Customization of Thermal Expansion in Nanowires

Author:
Sofia GONÇALVES

Supervisor:
Arlete APOLINÁRIO

Co-supervisor:
João HORTA BELO

A thesis submitted in fulfilment of the requirements
for the degree of MSc. Engineering Physics

at the

Faculdade de Ciências da Universidade do Porto
Departamento de Física e Astronomia

December 7, 2021

“ We were born to make history. ”

Make History by *Dean Fujioka*, written by Dean Fujioka, Tarou Umebayashi and Yuuta Bandou

Acknowledgements

This dissertation is the result of all the work I developed during this year at IFIMUP-IN. During this time, I had the privilege to meet new people and have new experiences as I finished this chapter in my life. I would like to express my gratitude to all who directly or indirectly contributed and supported me during this thesis.

Firstly, I would like to express my deepest thanks to both my supervisors Doctor Arlete Apolinário and Doctor João Horta Belo, for everything they did for me and for believing in me. This project would not have been possible without their support and guidance.

I also have to thank Doctor Vivian Andrade and Doctor Célia Sousa for helping me in the laboratory and providing their insight throughout this work.

I would also express my gratitude to Doctor Mariana Proença and Professor Jonh Evans for all the help with samples measurements and availability.

Additionally, as this also represents the end of my master's degree, I would like to thank my colleagues and friends that have been with me since the begging.

Finally, I am grateful to my parents, sister and boyfriend for always being there for me even in the toughest times. For their unconditional love and encouragement. And also to all of my family for always being there and supporting me.

There is much more that I want to express, but words are not enough.

This work was supported by the Portuguese Fundação para a Ciência e Tecnologia (FCT) and COMPETE 2020 (FEDER) under the project POCI-01-0145-FEDER-028676; "SMARTX – SMART materials transitions probed by X-ray diffraction" bilateral research fund between Faculty of Sciences of Porto University and Durham University and funded by PARSUK in 2021/2022; Advanced Photon Source "Unveiling first-order transition kinetics via fast Synchrotron radiation diffraction", reference "GUP-69910"; and A. Apolinário, would like to acknowledge FCT for her DL57 contract (Ref º SFRH/BPD/87430/2012).

UNIVERSIDADE DO PORTO

Abstract

Faculdade de Ciências da Universidade do Porto
Departamento de Física e Astronomia

MSc. Engineering Physics

Customization of Thermal Expansion in Nanowires

by Sofia GONÇALVES

The control of thermal expansion in the technology industry is highly required to reduce degradation due to thermal expansion mismatch between materials during operation. It is common knowledge that materials expand when heated. However, some materials possess the unusual property of volume contraction upon heating. Recent advances at the nanoscale, more precisely in solids with at least one nanoscale dimension, revealed a size-dependent thermal expansion in several materials due to the surface effects rising from the dimensional reduction to 1D. FeCo alloys have diversified applications such as magnetic recording, catalysts and drug delivery. FeCo thin films have been proved to possess a giant and negative magnetostriction, and this motivated the search for NTE in this material at the nanoscale. These alloys are also considered invar alloy and possess almost no thermal expansion in the transition from ferromagnetic to paramagnetic.

In this dissertation, the first goal was to synthesize (by DC electrodeposition method) and characterize FeCo thin films with the stoichiometries of $Fe_{20}Co_{80}$, fabricated under different conditions, and transpose the same methods to the fabrication of $Fe_{20}Co_{80}$ nanowires (NWs), using a template assisted method (nanoporous alumina templates). This study was extended to FeCo thin films and NWs synthesized with different stoichiometries of $Fe_{10}Co_{90}$, $Fe_{50}Co_{50}$ and $Fe_{90}Co_{10}$. Facing several difficulties, an extensive study to find the optimal electrodeposition potential for these electrodeposition solutions was performed. At the end, we were able to have the perfect control features such as, stoichiometry, pore diameter and length of the electrodeposited NWs. With optimized parameters, FeCo NWs samples with stoichiometries of $Fe_{10}Co_{90}$ and $Fe_{50}Co_{50}$ had their thermal expansion evaluated, by X-Ray Diffraction technique, revealing that they possess

lower thermal expansion than bulk counterparts (that were also fabricated by arc melting technique). Additionally, oxidized $Fe_{10}Co_{90}$ thin films were used as a co-catalyst for the photoelectrochemical process of water splitting, where they to be a very promising material for the green hydrogen generation application.

Thermal expansion studies, using High - Resolution Synchrotron X-Ray Radiation Diffraction technique, were also perform in the system $LaFe_{11.9}Mn_{0.27}Si_{1.29}H_x$ microparticles with different sizes, obtained by ball milling technique. Because this material already shows negative thermal expansion, the reduction in size and the induced strain through ball milling led to broaden the temperature window where this phenomenon occurs.

This work proved that the customization of materials from different families, such as FeCo alloys and $LaFe_{11.9}Mn_{0.27}Si_{1.29}H_x$, is possible by modifying the size of the materials. Which demonstrates that size reduction is a key tool in the tuning of the thermal expansion of different materials.

Crystallographic analysis of the obtained XRD diffractograms for FeCo NWs and microparticles $LaFe_{11.9}Mn_{0.27}Si_{1.29}H_x$ were performed by Rietveld refinement using the Fullprof package.

Morphology, structural and magnetic characterizations were performed by Emission Scanning Electron Microscopy, X-Ray Diffraction, and Superconducting Quantum Interference Device Magnetometer and Vibrating Sample Magnetometer.

UNIVERSIDADE DO PORTO

Resumo

Faculdade de Ciências da Universidade do Porto
Departamento de Física e Astronomia

Mestrado Integrado em Engenharia Física

Costumização da Expansão Térmica em Nanofios

por Sofia GONÇALVES

O controle da expansão térmica na indústria tecnologica é altamente necessário para reduzir a degradação devido à incompatibilidade da expansão térmica entre materiais durante a operação. É do conhecimento comum que os materiais se expandem quando aquecidos. No entanto, alguns materiais possuem a propriedade incomum de contração de volume durante o aquecimento. Avanços recentes em nanoescala, mais precisamente em sólidos com pelo menos uma dimensão em nanoescala, revelaram uma expansão térmica dependente do tamanho em vários materiais devido aos efeitos de superfície aumentando da redução dimensional para 1D. As ligas FeCo têm aplicações diversificadas, como gravação magnética, catalisadores e distribuição de drogas. Ficou provado que os filmes finos de FeCo possuem magnetostricção gigante e negativa, o que motivou a busca por NTE neste material em nanoescala. Essas ligas também são consideradas ligas invar e quase não possuem expansão térmica na transição de ferromagnética para paramagnética.

Nesta dissertação, o primeiro objetivo foi sintetizar (pelo método de eletrodeposição DC) e caracterizar filmes finos de FeCo com a estequiometrias de $Fe_{20}Co_{80}$, fabricados em diferentes condições, e transpor os mesmos métodos para a fabricação de $Fe_{20}Co_{80}$ nanofios (NWs), usando um método assistido por modelo (modelos de alumina nanoporosa). Este estudo foi estendido a filmes finos de FeCo e NWs sintetizados com diferentes estequiometrias de $Fe_{10}Co_{90}$, $Fe_{50}Co_{50}$ e $Fe_{90}Co_{10}$. Enfrentando várias dificuldades, um extenso estudo para encontrar o potencial de eletrodeposição ideal para essas soluções de eletrodeposição foi realizado. Ao final, pudemos ter os recursos de controle perfeitos como estequiometria, diâmetro dos poros e comprimento dos NWs eletrodepositados. Com parâmetros otimizados, as amostras de FeCo NWs com estequiometrias de $Fe_{10}Co_{90}$

e $Fe_{50}Co_{50}$ tiveram sua expansão térmica avaliada, pela técnica de Difração de Raios-X, revelando que possuem menor expansão térmica que as contrapartes bulk (que também foram fabricadas por técnica de fusão a arco). Adicionalmente, filmes finos oxidados de $Fe_{10}Co_{90}$ foram usados como co-catalisadores para o processo fotoeletroquímico de separação de água, onde se tornaram um material muito promissor para a aplicação de geração de hidrogênio verde.

Estudos de expansão térmica, utilizando a técnica de Difração de Raios-X de Sincrotrão de Alta Resolução, também foram realizados no sistema $LaFe_{11.9}Mn_{0.27}Si_{1.29}H_x$ micropartículas de diferentes tamanhos, obtidas por bola técnica de moagem. Por esse material já apresentar expansão térmica negativa, a redução do tamanho e a deformação induzida através do moinho de bolas ampliam a janela de temperatura onde ocorre esse fenômeno.

Este trabalho comprovou que a customização de materiais de diferentes famílias, como ligas FeCo e $LaFe_{11.9}$
$Mn_{0.27}Si_{1.29}H_x$, é possível modificando o tamanho dos materiais. O que demonstra que a redução de tamanho é uma ferramenta fundamental no ajuste da expansão térmica de diferentes materiais.

A análise cristalográfica dos difratogramas de XRD obtidos para FeCo NWs e $LaFe_{11.9}$ $Mn_{0.27}Si_{1.29}H_x$ micropartículas foram realizadas por refinamento Rietveld usando o pacote Fullprof.

As caracterizações morfológicas, estruturais e magnéticas foram realizadas por Microscopia Eletrônica de Varrimento, Difração de Raios-X e SQUID e VSM.

Contents

Acknowledgements v

Abstract vii

Resumo ix

Contents xi

List of Figures xv

Glossary xxi

1 Introduction 1

2 Thermal Expansion 5
2.1 Mechanisms and Materials . . . 5
2.1.1 Structural NTE . . . 7
2.1.2 Phase Transition NTE . . . 9
2.1.2.1 Magnetic Transition . . . 9
2.1.2.2 LAFeSi Compounds . . . 11
2.1.2.3 Ferroelectric Transition . . . 12
2.1.2.4 Charge-Transfer Transition . . . 13
2.1.2.5 Metal-Insulator Transition . . . 14
2.2 Nanoscale Negative Thermal Expansion . . . 15
2.2.1 Thermal Expansion in Nanowires . . . 16

3 Fabrication Methods 19
3.1 Nanoporous Alumina Templates . . . 19
3.2 Electrodeposition . . . 25
3.2.1 Nucleation and Growth Mechanisms . . . 26

4 Iron Cobalt Alloys 31
4.1 Magnetostriction . . . 31
4.2 Thermal Expansion . . . 36
4.3 FeCo Nanowires - Properties . . . 37

5 Experimental and characterization techniques 45

5.1 Materials . . . 45
5.2 Methods . . . 46
5.2.1 Substrate Cleaning . . . 47
5.2.2 Electropolishing . . . 47
5.2.3 Electrochemical Anodization . . . 47
5.2.4 Electrodeposition . . . 48
5.2.5 Sputtering . . . 50
5.2.6 Arc-melting furnace . . . 51
5.3 Characterization Thecnique . . . 51
5.3.1 Electron Microscopy . . . 51
5.3.1.1 Scanning Electron Microscopy (SEM) . . . 52
5.3.1.2 Energy-dispersive Spectroscopy (EDS) . . . 52
5.3.2 X-Ray Diffraction (XRD) . . . 53
5.3.3 High - Resolution Synchrotron X-Ray Radiation Diffraction Technique 53
5.3.4 Superconducting Quantum Interference Device (SQUID) . . . 54
5.3.5 Vibrating Sample Magnetometer (VSM) . . . 54

6 Results and Discussion 55
6.1 Bulk FeCo alloys . . . 55
6.1.1 Structural Characterization . . . 56
6.1.2 Magnetic Characterization . . . 57
6.2 $Fe_{20}Co_{80}$ alloys . . . 59
6.2.1 $Fe_{20}Co_{80}$ Thin Films . . . 59
6.2.1.1 Morphological Characterization . . . 63
6.2.1.2 Structural Characterization . . . 64
6.2.2 $Fe_{20}Co_{80}$ Nanowires . . . 66
6.2.2.1 Morphological Characterization . . . 68
6.2.2.2 Structural Characterization . . . 72
6.3 Fe_xCo_{1-x} (x = 10, 50, 90) alloys . . . 73
6.3.1 Fe_xCo_{1-x} (x = 10, 50, 90) Thin Films . . . 74
6.3.1.1 Morphological Characterization . . . 76
6.3.1.2 Structural Characterization . . . 77
6.3.2 Fe_xCo_{1-x} (x = 10, 50, 90) Nanowires . . . 79
6.3.2.1 Morphological Characterization . . . 80
6.3.2.2 Structural Characterization . . . 82
6.4 Optimization of electrodeposition potential for Fe_xCo_{1-x} (x = 10, 50, 90) Nanowires . . . 83
6.4.1 Linear Sweep Voltammetry . . . 84
6.4.2 Sequential FeCo Electrodeposition in a Nanoporous Alumina Template . . . 85
6.5 Customization and Characterization of Fe_xCo_{1-x} (x = 10, 50, 90) Nanowires 89
6.5.1 Morphological Characterization . . . 91
6.5.2 Structural Characterization . . . 93
6.5.3 Magnetic Characterization . . . 94
6.5.4 Thermal Expansion Characterization . . . 95
6.6 FeCo Based Co-catalyst for H_2 Green Generation . . . 98

6.7 Customization of the Negative Thermal Expansion in $LaFe_{11.9}Mn_{0.27}Si_{1.29}H_x$ 100

7 Conclusions and future work **107**
7.1 Conclusion 107
7.2 Future Work 108

8 Appendix A **109**

Bibliography **117**

List of Figures

2.1 Potential energy versus interatomic distance for two bonded atoms. With increasing temperature higher states are occupied leading to a slightly increase in the bond length, adapted from [2, 4, 17] 7
2.2 Schematic of the possible lattice modes for a chain of atoms. a) Longitudinal optical mode, b) transverse optic mode where the chain is shortened, giving rise to a large NTE as the vibrational amplitude increases with temperature, and c) transverse acoustic mode that leads to a more modest NTE with increasing temperature, adapted from [2]. 7
2.3 Schematic example of anisotropic thermal expansion in the silicates. The blue layers expand and because the covalent bonds, represented as the lilac lines, do not expand, the layers are brought together causing a thermal contraction in this direction, adapted from [1]. 8
2.4 Schematic example of negative thermal expansion in a flexible network. The soft linkages rotate while the strong bonds are kept intact. A change in the vibrational mode is induced by temperature leading to a volumetric thermal contraction, adapted from [1]. 8
2.5 NTE associated with a phase transition has a direct relation with the temperature window ΔT, meaning that the CTE slope will vary with the ΔT. There is a change from large-volume low-T to a small-volume high-T state, which lead to NTE, adapted from [1]. 10
2.6 $\Delta L/L$ (reference temperature: 300 K) as a function of temperature for the compounds $LaFe_{13-x}Si_x$ (x = 1.5, 1.8, 2.1 and 2.4) in a temperature range of 77 to 300 K.[26] 12
2.7 Schematic of the change in the chain of a ferroelectric material with charge disproportion upon heating. The asymmetric chain changes to a symmetric one, adapted from [1]. 12
2.8 Summary of negative thermal expansion mechanisms and examples of materials [1]. 15

3.1 Schematic representation of an hexagonal ordered arrays in a NAT and corresponding cross-section view by SEM. [15] 20
3.2 a) Schemes of two types of alumina barrier, barrier-type on the left and porous-type on the right, with the inner and outer oxide layers indicated. b)Schematic representations of the electrochemical processes at the anode, electrolyte/oxide and oxide/metal interfaces.[15] 21
3.3 Typical current density curve with the identification of the four main pore growth stages[15]. 22

3.4 SEM images of NAT[a),b) and c) top surface; d), e) and f) cross-section] fabricated under various anodization conditions: a) and d) 0.3 M sulfuric acid with $V_{app} = 25V$; b) and e) 0.3 M oxalic acid with $V_{app} = 40V$; and a) and d) 0.1 M phosphoric acid with $V_{app} = 195V$. [15] . . . 23
3.5 Comparison of mild anodization with hard anodization. a) Interpore distance (D_{int}) versus anodization voltage (V_{app}) for MA and HA. b) Current density curves for HA and MA using 0.3 M oxalic acid as electrolyte. [57] . 24
3.6 Representation of the three different methods of electrodeposition to fill NAT [15]. . . . 26
3.7 Schematic representation of the template preparation to grow NWs using a) DC electrodeposition and b) AC or pulsed electrodeposition [15]. . . . 27
3.8 Different stages of electrodeposition: charge of the electric double layer at the electrode; nucleation/growth; and continuous deposition ,adapted from [59] . . . 27

4.1 Iron-cobalt bulk phase diagram [75] [10]. . . . 32
4.2 Magnetostriction of Fe_xCo_{1-x} thin films versus at. % of Co for differently prepared thin films, adapted from [9]. . . . 32
4.3 Magnetostriction of bulk FeCo alloys versus at. % of Co for different annealing temperatures [11]. . . . 34
4.4 The XRD patterns of Fe_xCo_{1-x} bulk alloys with fcc and bcc peaks index [10]. 34
4.5 Magnetostriction versus annealing temperature for bulk alloys a) $Fe_{35}Co_{65}$ and b) $Fe_{22}Co_{78}$, adapted from [10]. . . . 35
4.6 Temperature dependence of the CTE of $Fe_{100-x}Co_x$ x = 69, 72, 74, 77 and 79) alloys in heating and cooling [14] . . . 36
4.7 Magnetic curves of $Fe_{50}Co_{50}$ NWs with (a) diameter of 60 nm and (b) diameter modulated of 60/120 nm, with coercivities of 84 mT and 74 mT, respectively [77]. . . . 38
4.8 Magnetic hysteresis curve of equiatomic FeCo NWs with length of (a) 7 μm and (b) 27 μm, with $H_{\parallel}$ and $H_{\perp}$ [67]. . . . 39
4.9 Magnetic hysteresis curve, with $H_{\parallel}$, of equiatomic FeCo NWs, with length of 20 μm before and after annealing at 300 ºC for 20 h [67]. . . . 40
4.10 (a) H_c and (b) SQ for NWs with D_{int} of 50 nm in function of NW diameter; (c) H_c and (d) SQ for NWs with diameters of 22 nm in function of D_{int}; where hollow squares represent NWs as-deposited and solid squares represent NWs annealed at 550 ºC [79]. . . . 41
4.11 XDR patterns of $Fe_{100-x}Co_x$ NWs with diameters of a) 40 nm and b) 20 nm [66]. . . . 42
4.12 (a) Evolution of $\mu_0 H_c$ and (b) SQ with atomic percentage of Co at room temperature for NWs with diameters of 40 nm and 20 nm. Temperature dependence of $\mu_0 H_c$ for NWs with diameters of (c) 40 nm and (d) 20 nm. [66] . . . 42

5.1 (a) Experimental set-up and (b) schematic of the set-up for the electropolishing. (c) Al foil before and after the electropolishing. . . . 47
5.2 (a) Experimental set-up and (b) schematic of the set-up for the anodization. 48
5.3 (a) Al foil removal, (b) alumina barrier removal, and $c)$ NAM sputtered with Au. . . . 49

5.4 (a) Experimental set-up and (b) schematic of the set-up for the electrodeposition. . . . 49
5.5 (a) Experimental set-up and (b) schematic of the set-up for the deposition of the thin film of gold by sputtering. . . . 50
5.6 Graphic representation of the set-up for the preparation of alloys using the arc melting furnace. . . . 51

6.1 XRD patterns of Co, $Fe_{10}Co_{90}$, $Fe_{50}Co_{50}$ and $Fe_{10}Co_{90}$ and Fe bulk alloys with the respective miller indexes. . . . 56
6.2 Crystallite size (green dots) and lattice parameter (blue dots) of the bulk alloys Fe_xCo_{1-x} (x = 0,10,50,90,100). . . . 58
6.3 a) Magnetic hysteresis loops of bulk alloys Fe, $Fe_{90}Co_{10}$, $Fe_{50}Co_{50}$ and Co at 300 k, and b) the magnetic hysteresis loops of $Fe_{90}Co_{10}$, $Fe_{50}Co_{50}$ bulk alloys performed at 300 K and at 5 K. . . . 58
6.4 M_s in function of the content of Fe of the bulk alloys Co, $Fe_{90}Co_{10}$, $Fe_{50}Co_{50}$ and Fe. Pink dots correspond to the measurements at 300 K and blue dots to measurements at 5 K, whereas the dashed line is only a guide obtained through a spline. . . . 59
6.5 Electrodeposition curves of the thin films in Cu tape using the test solution obtained with V_{dep} of -0.7, -1.0, -1.1, -1.2, and -1.8 V (vs. Ag/AgCl). The inset is a zoom in the first 50 s of the electrodeposition curves. . . . 60
6.6 a) Charge transferred as a function of time and b) current density maximum dependency with V_{dep} of -0.7, -1.0, -1.1, -1.2, and -1.8 V (vs. Ag/AgCl). . . . 61
6.7 Electrodeposition curves comparison with the theoretical model of 3D progressive and instantaneous nucleation. . . . 62
6.8 Blue dots correspond to the thin films thickness obtained using the test solution and applying V_{dep} of -0.7, -1.0, -1.1, -1.2, and -1.8 V (vs. Ag/AgCl), the red dash line is the linear fit. . . . 63
6.9 SEM images from the electrodeposition in copper tape with V_{dep} of a) -1.0, b) -1.1 and c) –1.8 V. Images with lower magnification were obtained with backscattered electrons, and the images with higher magnification were obtained with secondary electrons. . . . 64
6.10 XDR diffraction patterns of the thin films electrodeposited with applied potentials of -1.0, -1.1 and –1.8 V. The peaks represented correspond to bcc (110). . . . 65
6.11 Crystallite size (green dots) and lattice parameter (blue dots) of the corresponding thin films electrodeposited with applied potentials of -1.0, -1.1 and –1.8 V. . . . 66
6.12 Electrodeposition curves of the NWs with D_p of ∼45 and ∼75 nm fabricated using the test solution with V_{dep} of -1.1, -1.2 and -1.8 V (vs. Ag/AgCl). 67
6.13 Total charge transferred in the electrodeposition of the NWs with D_p of ∼45 and ∼75 nm fabricated using the test solution with V_{dep} of -1.1 and -1.8 V (vs. Ag/AgCl). . . . 68
6.14 SEM images of the NWs electrodeposited at V_{dep} of a) -1.1, b) -1.2, and c) –1.8 (V vs. Ag/AgCl) in membranes with $D_p \sim 45$ nm (group A). . . . 69
6.15 Comparison between theoretical and experimental NWs lengths of the NWs electrodeposited at V_{dep} of -1.1, -1.2 and –1.8 (V vs. Ag/AgCl) in membranes with $D_p \sim 45$ nm. . . . 70

6.16 SEM images of the NWs electrodeposited at V_{dep} of a) -1.1 and b) –1.8 (V vs. Ag/AgCl) in membranes with $D_p \sim 75$ nm (group B). . . . 71
6.17 Comparison between theoretical and experimental NWs lengths of the NWs electrodeposited at V_{dep} of -1.1 and –1.8 (V vs. Ag/AgCl) in membranes with $D_p \sim 75$ nm. . . . 71
6.18 XDR diffraction patterns of the samples a) 1, 2, 3, 4, and b) 5, comparing with the XDR diffraction pattern of a sample with a thin film of Au and Au NWs. . . . 73
6.19 Electrodeposition curves of the thin films fabricated in Cu tape using the ($Fe_{10}Co_{90}$, $Fe_{50}Co_{50}$ and $Fe_{90}Co_{10}$) solutions at a potential of -1.8 V (vs. Ag/AgCl). . . . 74
6.20 The dots correspond to the thin films thickness obtained using the solutions with different concentrations of Fe and Co, by applying a V_{dep} of -1.8 V (vs. Ag/AgCl). . . . 75
6.21 Electrodeposition curves comparison with the theoretical model of 3D progressive and instantaneous nucleation. . . . 76
6.22 SEM images from the thin films electrodeposited in Cu tape using solutions $Fe_{10}Co_{90}$, $Fe_{50}Co_{50}$ and $Fe_{90}Co_{10}$ at -1.8 V (vs. Ag/AgCl). . . . 77
6.23 XDR diffraction patterns for peeled off thin films with stoichiometries of $Fe_{10}Co_{90}$, $Fe_{50}Co_{50}$ and $Fe_{90}Co_{90}$ (the stoichiometries of the thin films are theoretical). . . . 78
6.24 Crystalline size (green dots) and lattice parameter (blue dots) of the corresponding thin films electrodeposited using solutions $Fe_{10}Co_{90}$, $Fe_{50}Co_{50}$ and $Fe_{90}Co_{90}$ at -1.8 V (vs. Ag/AgCl). . . . 79
6.25 Electrodeposition curves of the NWs with D_p of ∼45 nm fabricated using solutions with different concentrations of Fe and Co, at a V_{dep} of -1.8 V (vs. Ag/AgCl). . . . 80
6.26 SEM images of the NWs electrodeposited at V_{dep} –1.8 (V vs. Ag/AgCl) in membranes with $D_p \sim 45$ nm using solutions with different concentrations of Fe and Co. . . . 81
6.27 Comparison between theoretical and experimental NWs lengths of the NWs electrodeposited at V_{dep} –1.8 (V vs. Ag/AgCl) in membranes with $D_p \sim 45$ nm using solutions with different concentrations of Fe and Co. . . . 82
6.28 XDR diffraction patterns of the samples 6 and 7, comparing with the XDR diffraction pattern of a sample with a thin film of Au and Au NWs. . . . 83
6.29 Linear sweep voltammetry curves obtain for each solution in NAMs (1^{st}, 2^{nd}, and 3^{rd} scans) and on Au thin film. . . . 84
6.30 Current density transients, for each solution, during FeCo electrodeposition in NAMs performed at different constant potentials, between -1.0 and -1.8 V, for 6 min. . . . 85
6.31 Linear sweep voltammetry curves obtain for each solution in NAMs (1^{st}, 2^{nd}, and 3^{rd} scans) and thin film of Au. Scattered points correspond to the current density values after 6 min of FeCo potentiostatic deposition, for each solution. . . . 86
6.32 Total charge transferred during the process of electrodeposition at the different V_{dep} for each solution. . . . 86
6.33 Total charge transferred during the process of electrodeposition at the different potentials for each solution in function of the applied potential. . . . 87

6.34 SEM images, obtained using backscattered electrons, of the multisegmented Au/FeCo NWs fabricated by electrodeposition of the three solutions at different potentials. . . . 87
6.35 NWs length versus the applied potential for the three solutions, estimated by measuring the NWs in the SEM images. . . . 88
6.36 NWs length obtained experimentally and theoretically in function of the total charge transferred. . . . 88
6.37 NWs length in function of the total charge transferred in the linear behaviour. 89
6.38 Electrodeposition curves of the samples 9, 10 and 11 with $\sim$ 40 nm, and samples 12, 13 and 14 with $\sim$ 130 nm. . . . 90
6.39 SEM images of the samples 9, 10 and 11 with $\sim$ 40 nm, and samples 12, 13 and 14 with $\sim$ 130 nm, obtained with backscattered electrons. . . . 91
6.40 SEM images of the bottom of the samples 12, 13 and 14 with $\sim$ 130 nm, obtained with secondary electrons. . . . 91
6.41 Nanowires length obtained experimentally in comparison with the theoretical values, for samples 9 to 14. . . . 92
6.42 XRD patterns of the samples 9 to 14 with the corresponding indexes and a pattern of Au NWs to compare with pure Au diffracted peaks (indexed in grey color). . . . 93
6.43 Normalized magnetic hysteresis curves of the FeCo NWs samples 9, 10 and 11 a) with $H_{\parallel}$ and b) $H_{\perp}$; and the FeCo NWs samples 12, 13 and 14 c) with $H_{\parallel}$ and d) $H_{\perp}$. . . . 94
6.44 H_c dependence on the Fe content at room temperature for FeCo NWs with D_p of $\sim$ 43 and $\sim$ 133 nm, and lengths of $\sim$ 4 and $\sim$ 9 μm, respectively. . . . 95
6.45 Variation of SQ (M_r/M_s) with Fe content at room temperature for FeCo NWs with D_p of $\sim$ 43 and $\sim$ 133 nm, and lengths of $\sim$ 4 and $\sim$ 9 μm, respectively. . . . 96
6.46 Unit cell volume as a function of temperature, in heating and cooling, obtained through Rietveld sequential fits for the samples with stoichiometries of a) $Fe_{50}Co_{50}$ and b) $Fe_{10}Co_{90}$. . . . 97
6.47 $\Delta V/V$ as a function of the temperature for the samples a) $Fe_{50}Co_{50}$ and b) $Fe_{10}Co_{90}$, with various linear interpolations. . . . 98
6.48 Thermal expansion coefficient as a function of the temperature obtained by differentiation of the various linear interpolations of $\Delta V/V$ for the samples a) $Fe_{50}Co_{50}$ and b) $Fe_{10}Co_{90}$. . . . 98
6.49 a) Electrodeposition curves of the $Fe_{10}Co_{90}$ thin films deposited in Fe thin films with thicknesses of 150 and 300 nm; b) solar measurements of current in function of the applied potential (vs. RHE) for both samples. . . . 100
6.50 SEM images of the $LaFe_{11.9}Mn_{0.27}Si_{1.29}H_x$ samples, the original and the ball milled for different times. . . . 101
6.51 Normalized M(T) curves for the samples $LaFe_{11.9}Mn_{0.27}Si_{1.29}H_x$, original and ball milled for 14, 45, 90 and 180 minutes, obtained under field-cooled. The inset represents the T_c as a function of the ball milling time. . . . 102
6.52 XRD pattern acquired for the sample of $LaFe_{11.9}Mn_{0.27}Si_{1.29}H_x$ ball milled for 180 minutes in cooling. . . . 103

6.53 Normalized unit cell volumes in the temperature range from -40 to 100 ºC, obtained through sequential Rietveld refinements for all $LaFe_{11.9}Mn_{0.27}Si_{1.29}H_x$ samples, in a) heating and in b) cooling and the c) d) derivatives in order of temperature, respectively. 104
6.54 a) Full width at half maximum (FWHM) of the derivatives of the unit cell volume in heating (red dots) and in cooling (blue dots), and the magnetization (purple dots) as a function of the ball milling time, comparing with b) the particle size, for all samples of $LaFe_{11.9}Mn_{0.27}Si_{1.29}H_x$. 105
6.55 Thermal expansion coefficient (CTE) in function of the temperature for all samples of $LaFe_{11.9}Mn_{0.27}Si_{1.29}H_x$, obtained on a) heating and on b) cooling. 106

8.1 Full XDR diffraction patterns of the thin films electrodeposited with applied potentials of -1.0, -1.1 and –1.8 (V vs. Ag/AgCl). 109
8.2 XDR diffraction patterns of the NWs samples 1, 2, 3, 4 and 5 fabricated using the test solution and a sample of only sputtered Au and Au NWs for comparison. 110
8.3 XDR diffraction patterns of a sample with a thin film deposited through sputtering and 6 min of Au electrodeposition at -1.0 (V vs. Ag/AgCl). . . . 110
8.4 XDR diffraction patterns of the NWs samples 6 and 7 fabricated using solutions with different concentrations of Co and Fe. and a sample of only sputtered Au and Au NWs for comparison. 111
8.5 SEM image, using backscatered electrons, of the multisegmented Au/FeCo NWs electrodeposited using the solution $Fe_{10}Co_{90}$. 111
8.6 Histograms with the particle size distribution of each $LaFe_{11.9}Mn_{0.27}Si_{1.29}H_x$ samples. 112
8.7 XRD pattern (in red) and Rietveld refinement (in black) for the sample of $LaFe_{11.9}Mn_{0.27}Si_{1.29}H_x$ ball milled for 180 min, at temperature 26.3 K. 112
8.8 Unit cell volumes in the temperature range from -40 to 100 ºC, obtained through sequential Rietveld refinements for all $LaFe_{11.9}Mn_{0.27}Si_{1.29}H_x$ samples, in a) heating and in b) cooling 113
8.9 XRD patterns of the samples with stoichiometries of $Fe_{50}Co_{50}$ and $Fe_{10}Co_{90}$, corresponding to the first measurement, the measurement at the highest temperature, and the last measurement. 113
8.10 Rietveld fits examples obtained for the sample with stoichiometry of $Fe_{50}Co_{50}$ at different temperatures. XRD patterns correspond to the first measurement, the measurement at the highest temperature, and the last measurement. 113
8.11 Rietveld fits examples obtained for the sample with stoichiometry of $Fe_{10}Co_{90}$ at different temperatures. XRD patterns correspond to the first measurement, the measurement at the highest temperature, and the last measurement. 114
8.12 Preliminary results obtained for the sample with stoichiometry $Fe_{50}Co_{50}$ with Rietveld fits. These include the height of the sample, lattice parameter of the FeCo and the lattice parameters of the Au. 114
8.13 Unit cell volume of the Au obtained from the sequential Rietveld fits of the sample with stoichiometry $Fe_{50}Co_{50}$. 115
8.14 Bulk FeCo alloys thermal expansion from the literature such as for Fe and Co [86, 87], and $Fe_{21}Co_{79}$ and $Fe_{31}Co_{69}$ [14]. 116

Glossary

CTE	Coefficient of Thermal Expansion
D_p	Pore Diameter
D_{int}	Interpore Distance
EDS	Energy-dispersive Spectroscopy
FC	Field-cooled
FM	Ferromagnetic
HA	Hard Anodization
MA	Mild Anodization
NAM	Nanoporous Alumina Membrane
NW	Nanowire
NTE	Negative Thermal Expansion
PAA	Porous Anodic Alumina
PM	Paramagnetic
PTE	Positive Thermal Expansion
SEM	Scanning Electron Microscopy
SQUID	Superconducting Quantum Interference Device
RT	Room Temperature
Tc	Curie Temperature
V_{app}	Applied Voltage
XRD	X-Ray Diffraction
ZFC	Zero-field-cooled

ZTE Zero Thermal Expansion

δ_b Oxide Barrier Layer

Chapter 1

Introduction

There is an urge to control thermal expansion in the technology industry, where small distortions can degrade high-precision devices and instruments due to thermal expansion. For a device with several constituents, there will likely be a thermal expansion mismatch between its materials. This can cause mechanical cracks and disrupted electrical connections. In recent years the control of thermal expansion has been extended to advanced electronics such as power semiconductor devices, thermoelectric conversion systems, fuel cells[1] and telescopes. In addition to this usage of controlled thermal expansion, it is also useful for simpler applications like ceramic cooker hobs [2], dental materials [3], large structures such as railroad tracks and bridges [4]. With this being, controllable thermal expansion undeniably enhances and reliability of devices while prolonging their lifetime. [4]

Most materials expand when heated, showing a positive thermal expansion (PTE). However, some materials possess the unusual property of volume contraction upon heating. Therefore, these are said to have a negative thermal expansion (NTE). This is a phenomenon that occurs naturally, and it is more often observed in solid state materials.

The customization of thermal expansion is possible using materials with NTE, since these can be combined with PTE materials, one can obtain the desired thermal expansion. Also, zero thermal expansion composites can be achieved by combining materials or composites with symmetric thermal expansions. However, some materials already possess ZTE, being these called invar. This term originated from 1897 when Ch. E. Guillaume found that the ferromagnetic fcc $Fe_{65}Ni_{35}$ alloy showed an almost invariant TE in a wide range of temperatures around room temperature. This discovery granted Guillaume the Nobel Prize in Physics in 1920. [5]

The discovery of the large isotropic NTE in ZrW_2O_8, in 1996 by Mary et al. [6], has encouraged the subsequent development and discovery of other giant NTE materials, leading to the remarkable progress of research in this field. Recent advances have been made at nanoscale, more precisely in solids with at least one nanoscale dimension. Nanosolids exhibit peculiar functional properties due to the size effect, leading to a size-dependent thermal expansion and behaving differently from bulk counterparts. Therefore, size tuning presents itself as an efficient tool-technique in the customization of the thermal expansion. [7]

FeCo alloys have diversified applications such as magnetic recording, catalysts, pigments and drug delivery [8]. Also, it has been proven that this alloy possesses both giant and negative magnetostriction, in the form of thin-film [9] or bulk alloys [10–12]. In solid oxide fuel cells (SOFCs), the large difference between the TE of the cathode and the electrolyte easily cause degradation and fractures during thermal cycles, the same happens in batteries. Using materials with a compatible TE is crucial and can be achieved by combining the cathode or other components with an NTE material.[13] Because FeCo alloys are used as catalysts and cathodes in both these applications, these are one of the many applications where the customization of the TE comes in handy. Therefore, FeCo alloys arise as great candidates to customize the TE. The FeCo alloys presents similar proprieties as FeNi alloys. Therefore they are also considered invar alloys [5, 14]. Due to these reasons, this work intends to produce nanowires of FeCo with different features that can be controlled by simple technique of electrodeposition in nanoporous alumina templates. This method is inexpensive and very versatile, making it possible to tailor the dimensions of the nanowires [15, 16]. Herewith, it is expected to customize the TE in FeCo nanowires.

This dissertation will be divided into seven chapters, starting with this introductory chapter. A general view of TE in materials and the motivation to customize this property in FeCo alloys is presented. Chapter 2 includes a brief explanation of the mechanisms behind the TE. Chapter 3 presents the fabrication methods of the nanoporous alumina templates and the mechanisms of the electrodeposition method used to fabricate NWs and thin films. In chapter 4, the general characteristic of FeCo alloys is described, from the bulk to nanoscale. Chapter 5 presents the fabrication and characterization techniques used throughout this dissertation. Chapter 6 presents the results obtained and their discussion. These results include an analysis of bulk FeCo alloys; initial tests performed to

optimize the fabrication of the FeCo nanowires alloys; the characterization of the thermal expansion in the nanowires synthesized; an application of FeCo as co-catalyst for the generation of green H_2; and the characterization of the size-induced thermal expansion in LaFeSi alloy. Finally, chapter 7, where the main conclusion of this work is present.

Chapter 2

Thermal Expansion

2.1 Mechanisms and Materials

Thermal expansion is an intrinsic property of all materials, and it is quantified through the coefficient of thermal expansion (CTE). This coefficient may be expressed in terms of linear CTE:

$$\alpha_L = \frac{1}{L}\frac{dL}{dT} \tag{2.1}$$

or volume CTE:

$$\alpha_V = \frac{1}{V}\frac{dV}{dT} \tag{2.2}$$

respectively correspond to the change in length L or volume V of an object with temperature T at constant pressure p. The CTE units are usually represented in parts per million ($10^{-6}\ K^{-1}$). [2]

Materials can be isotropic, like liquids, glasses, polycrystalline ceramics, and cubic crystals, and these typically expand equally in any direction. In this case, the CTE, α_L, is the same in all directions and $\alpha_V = 3\alpha_L$. However, suppose the material is a uniaxial (tetragonal, hexagonal, or trigonal) crystal. In that case, it may have different CTE's depending on the direction of the measurement, giving rise to an anisotropic thermal expansion. In this case $\alpha_V = \alpha_{\parallel} + 2\alpha_{\perp}$, where $\alpha_{\parallel}$ and $\alpha_{\perp}$ are the CTE's parallel and perpendicular to the unique symmetry axis. And for crystals with orthorhombic or lower symmetry there are three different values of α mutually perpendicular, α_1, α_2 and α_3, so $\alpha_V = \alpha_1 + \alpha_2 + \alpha_3$. [2]

In solids, the thermodynamic origin of thermal expansion is expressed through the following relation:

$$\alpha_V = \frac{\gamma C_V}{\beta V} \tag{2.3}$$

where the C_V is the heat capacity at constant V and β represented as:

$$\beta = -V\frac{dp}{dV} \tag{2.4}$$

is the bulk modulus and γ being the weighted or macroscopic Grüneisen parameter summed over values for the active phonon frequencies ω_i as:

$$\gamma_i = -\frac{d(ln\omega_i)}{d(lnV)} \tag{2.5}$$

A phonon represents a mode of vibration [17] that arises from the oscillating atoms in a crystal lattice and contributes to ω_i. γ translates how the volume of the crystal is influenced by the changes in its vibrational modes, ω_i, that is driven by temperature changes. Since C_V and β are always positive values, the variations in the sign of CTE are caused by variations in the sign of γ. [2]

Most materials that show a positive CTE have a positive γ due to the anharmonic shape of the potential energy versus interatomic distance diagram, as schematically shown in figure 2.1. [2] As the temperature rises, the vibrational energy also rises, higher vibrational states become more populated, leading to an increase in the mean interatomic distance as the atoms move in the direction of the chain. The movement of the atoms is represented in figure 2.2 a). [17] In other words, the rising of the temperature implies a rise in the thermal vibration of an atom. To avoid colliding with other atoms, the mean bond length increases, characteristic of longitudinal optical phonons. [1, 2]

However, sometimes a more complex vibrational mode arises as the temperature increases, the transverse mode, where the atoms start to move perpendicularly to the direction of the atoms chain. In this mode, the phonons can be acoustic if the atoms move together, as showed in figure 2.2 c), or optical if the atoms move against each other, represented in figure 2.2 b) [2]

The origin of the NTE within a homogeneous solid can be broadly divided into two mechanisms, structural and electronic. The structural NTE corresponds to the said conventional NTE and is characterized by the atomic vibrational motion. As for the electronic NTE, this mechanism is accompanied by a phase transition and can have several origins. [2]

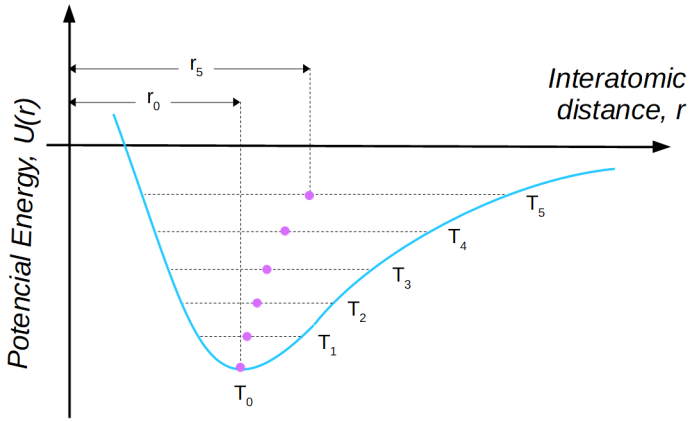


FIGURE 2.1: Potential energy versus interatomic distance for two bonded atoms. With increasing temperature higher states are occupied leading to a slightly increase in the bond length, adapted from [2, 4, 17]

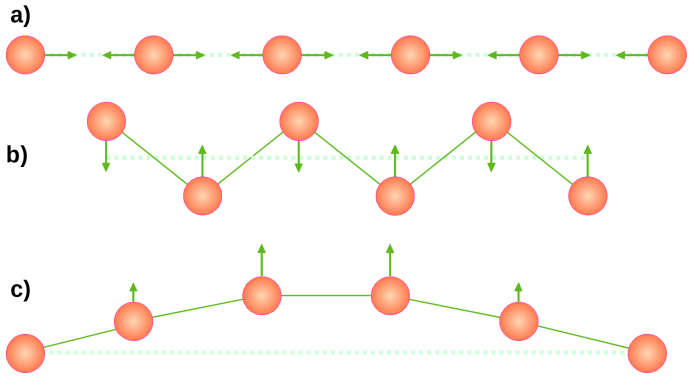


FIGURE 2.2: Schematic of the possible lattice modes for a chain of atoms. a) Longitudinal optical mode, b) transverse optic mode where the chain is shortened, giving rise to a large NTE as the vibrational amplitude increases with temperature, and c) transverse acoustic mode that leads to a more modest NTE with increasing temperature, adapted from [2].

2.1.1 Structural NTE

The so-called conventional NTE materials usually possess strong covalent bonds and not-so-strong ionic bonds. Upon heating, the ionic bonds expand. Because the strong covalent bonds do not expand, the layers in the material are brought together, giving rise to an anisotropic NTE, see figure 2.3. This phenomenon is characteristic of the silicon oxide family. [1]

From another perspective, displacement is induced when the material is heated, filling open spaces within the crystal structure. This process occurs by distorting the strong covalent bonds, see figure 2.4. This phenomenon occurs in flexible-network materials, consisting of rigid units, the covalent bonds, connected by soft linkages, the ionic bonds. It results in a volumetric NTE greater than the anisotropic thermal expansion. [1]

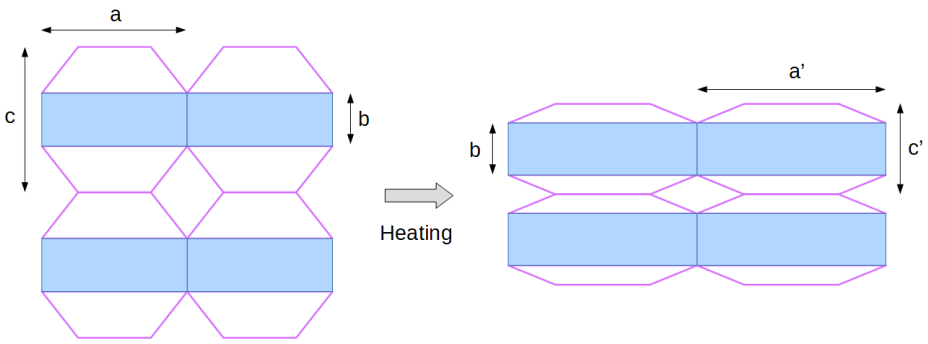


FIGURE 2.3: Schematic example of anisotropic thermal expansion in the silicates. The blue layers expand and because the covalent bonds, represented as the lilac lines, do not expand, the layers are brought together causing a thermal contraction in this direction, adapted from [1].

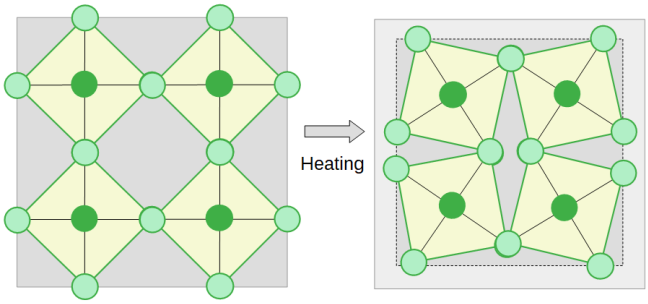


FIGURE 2.4: Schematic example of negative thermal expansion in a flexible network. The soft linkages rotate while the strong bonds are kept intact. A change in the vibrational mode is induced by temperature leading to a volumetric thermal contraction, adapted from [1].

One must conclude that the existence of both strong and not-so-strong chemical bonds is fundamental for conventional NTE. [1] Furthermore, the change from longitudinal optical phonons to transverse optical phonons, which lead to a shorting of the atoms chain and consequent NTE, can be excited at high temperatures. While the change to transverse acoustic phonons is excited at lower temperatures, it promotes a more modest NTE. [2, 17]

Some representative materials that have conventional NTE are the silicates $LiAlSiO_4$ (β-eucryptite) and $Mg_2Al_2Si_5O_{18}$ (cordierite). Both these materials have strong covalent bonds like Al−O and Si−O bonds and not-so-strong ionic bonds such as Li−O and Mg−O [1]. In the (β-eucryptite), the direction where the Li−O bond predominates expands 0.62 %, and the direction where the Si−O bond predominates expands 1.39 %. Leading to an overall volume contraction of 0.15 % and a linear coefficient of $\alpha_L = -7 \times 10^{-6}\ K^{-1}$, for temperatures between 293 K and 1073 K. [1, 18, 19]

Other materials with this type of NTE are the flexible-network ones as said previously. These include the ZrW_2O_8 that exhibit a volumetric NTE, $\alpha_V = -9 \times 10^{-6}\ K^{-1}$

below 1443 K, in which the W−O covalent bonds are strong, so the WO_4 are rigid. In contrast, the Z−W−O linkages are soft. [1, 6, 20, 21] Another examples of flexible-networks materials are: NZP family, AM_2O_7 (A = Ti, Zr, Hf; M = P, V), $Sc_2(WO_4)_3$, etc. [4]

Some more examples of materials that possess conventional NTE, are the fluoride group like ScF_3 and ZnF_2, Ag_2O, ZrV_2O_8, zeolitic forms of SiO_2 [1, 17], $Cd(CN)_2 \cdot xCCl_4$ ($\alpha_L = -34 \times 10^{-6}\ K^{-1}$ between 175 K and 375 K), etc. [1, 17, 22]

2.1.2 Phase Transition NTE

Phase transition NTE type is usually for dense metal alloys or ceramics which present a volume contraction upon a phase transition at a certain temperature. The NTE associated with a magnetic transition in the Fe−Pt invar alloy, 1990 by Wasserman [5], and ferroelectric transition in the $PbTiO_3$, 1952 by Shirane and Takeda [23], were identified a while ago. However, research for other materials with phase transition NTE has only been motivated after the discovery of the antiferromagnetic antiperovskite $Mn_3Zn_{1-x}Ge_xN$ with $\alpha_L = -25 \times 10^{-6}\ K^{-1}$ [1, 24]. This lead to the finding of materials with magnetic, ferroelectric, charge-transfer, and metal-insulator phase transitions accompanied by a reduction in volume. [1]

A phase transition occurs at a certain temperature. Consequently, there will only be a temperature window ΔT, around the phase transition temperature, where the material can present an NTE (figure 2.5. With this being said, there is a strong correlation between the slop of α_V and ΔT, meaning that the wider is the ΔT, the smaller is the α_V slope. Therefore, it is common to express the total volume change $\Delta V/V$ as a function of the temperature because the CTE is not intrinsic to the phase transition materials, but the total volume change is. There is the following relation:

$$\Delta V/V = \alpha_V \Delta T \tag{2.6}$$

where for isotropic materials $\alpha_V = 3\alpha_L$. [1]

2.1.2.1 Magnetic Transition

A magnetic transition is related to the magnetovolume effect, where a variation in the magnetic moment leads to a change in the crystal volume. However, not all materials that possess a magnetic transition have a significant magnetovolume coupling. This effect explains the interaction between magnetism and the volume of a crystal. It is quantified by

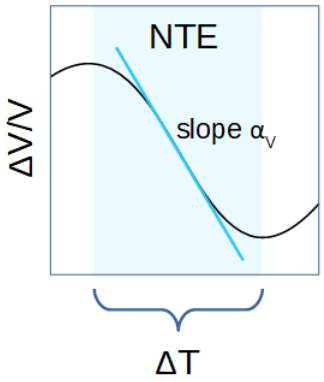


FIGURE 2.5: NTE associated with a phase transition has a direct relation with the temperature window ΔT, meaning that the CTE slope will vary with the ΔT. There is a change from large-volume low-T to a small-volume high-T state, which lead to NTE, adapted from [1].

the spontaneous volume magnetostriction, ω_s, which is caused by exchange interaction, and shows the volume change caused by modifications in the magnetic ordering with temperature change. [4, 13]

Magnetic materials typically present a volume change in the transition from the order-to-disorder magnetic configurations. Because the NTE related to these materials occurs around the Curie temperature T_C, the control of this parameter can tune the temperature range of NTE. [1, 4, 13]

One of the most important materials in this category is the invar $Fe_{35}Ni_{35}$ alloy because it shows an almost invariant thermal expansion ($\alpha_L = 1.5 \times 10^{-6}\ K^{-1}$, $193 - 373\ K$). [13] One of the most famous models to explain the mechanisms of the invar effect is the "2γ-state model". [4] This model assumes the existence of two different magnetically ordered states: a state γ_1 ferromagnetic and high volume with the magnetic spins parallel and aligned, and a γ_2 state the magnetic spins antiparallel and aligned. As the temperature increases, the γ_2 state becomes thermally excited, inducing a volume contraction that compensates for the thermal expansion of the lattice thermal vibration, which results in a low or zero thermal expansion. [4, 25] The invar effect is a property of several ferromagnetic alloys such as FeMn, CoMn, CoFe, CrFe, etc.[4, 5]

Some examples of materials that belong to this category are: $MnCo_{0.98}Cr_{0.02}Ge$, Fe_3Pt and YMn_2. [1] There is also the $La(Fe, Si, Co)_{13}$ family with $LaFe_{10.5}Co_{1.0}Si_{1.5}$ ($\alpha_L = -26 \times 10^{-6}\ K^{-1}$, $240 - 360\ K$) [26], for example.[4] Another well-known family is the antiperovskite Mn_3AN [24], where A is a transition metal or semiconductor element. The Mn atoms lie in the face-centred positions and the A atom in the body-centred position. This

type of antiperovskite sometimes presents an instantaneous lattice contraction caused by a magnetic transition from ferromagnetic or antiferromagnetic to paramagnetic. Representative examples of these family can be $Mn_3Cu_{0.5}Ge_{0.5}N$ ($\alpha_L = -12 \times 10^{-6}\ K^{-1}$, $280 - 365\ K$) [24] and $Mn_3Zn_{0.5}Sn_{0.5}N$ ($\alpha_L = -450 \times 10^{-6}\ K^{-1}$, $381 - 428\ K$) [27]. [4] The NTE in this type of transitions is significantly higher than the one that has origin only in a structural transition.

In this thesis, the materials FeCo and $La(Fe, Si)_{13}$ will be further explored.

2.1.2.2 LAFeSi Compounds

The $LaFe_{13-x}Si_x$ compounds are very well known for their giant magnetocaloric effect [28]. The NTE in this compounds occurs accompanied by a first-order magnetic transition without structural changes. In this ferromagnetic-to-paramagnetic transition, the variation in volume can reach up to 1.3%, with a sharp lattice contraction at the magnetic transition temperature. The volume contraction can be attributed to spin fluctuations leading to a reduction of magnetization.[28, 29] Besides, by increasing the Si content, the magnetic transition evolves from first-order, sharp and discontinuous transition, to second-order, smooth and continuous transition, and the Curie temperature increases as well. [26, 30] Because of the magnet volume effect, even if there is not an applied magnetic field, the crystal lattice still undergoes a change accompanied by the magnetic phase transition ferromagnetic-to-paramagnetic. Therefore, $LaFe_{13-x}Si_x$ compounds are extraordinary candidates for NTE. [4, 13, 26, 29, 30]

Huang et al. studied the $LaFe_{13-x}Si_x$ compounds aiming to convert the first-order phase transition into a second-order one. [26] In other words, to modified the sharp volume change into a continuous expansion, with the purpose of tuning the NTE operation-temperature window as desirable, namely by encompassing the room temperature. include room temperature. Compounds $LaFe_{13-x}Si_x$ (x = 1.5, 1.8, 2.1 and 2.4) were studied and the evolution from a first-order to a second-order transition occurred for x = 1.8. With this being, the compound $LaFe_{11.5}Si_{1.5}$ presents an abrupt volume change in the temperature range from 170 to 240 K and a CTE of $-50.1 \times 10^{-6}\ K^{-1}$. By contrast, the compound $LaFe_{10.6}Si_{2.4}$ shows a gradual volume contraction in the temperature range from 160 to 270 K and a CTE of $-11.2 \times 10^{-6}\ K^{-1}$ ($\Delta T = 110\ K$). For the temperature range from 77 to 300 K, all the compounds in this study show a NTE, with CTEs of $-15.2 \times 10^{-6}\ K^{-1}$ and $-5.4 \times 10^{-6}\ K^{-1}$ for $LaFe_{11.5}Si_{1.5}$ and $LaFe_{10.6}Si_{2.4}$, respectively.

Despite the work already developed with these materials, parameters such as particle size have not yet been studied as a form to customize the NTE. Due to this reason, we intend to study this dependency.

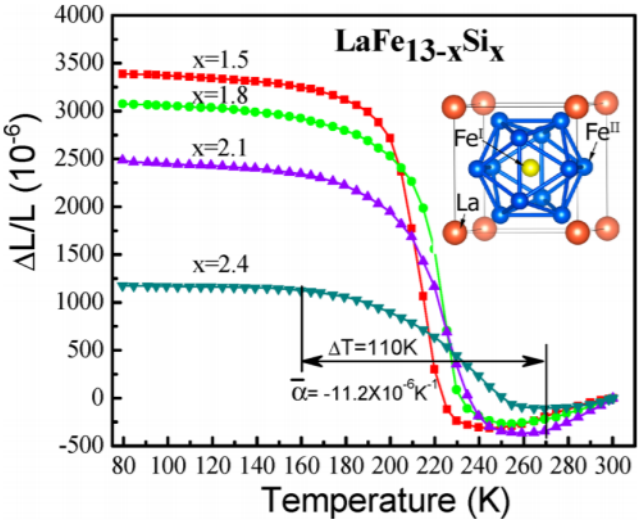


FIGURE 2.6: $\Delta L/L$ (reference temperature: 300 K) as a function of temperature for the compounds $LaFe_{13-x}Si_x$ (x = 1.5, 1.8, 2.1 and 2.4) in a temperature range of 77 to 300 K.[26]

2.1.2.3 Ferroelectric Transition

NTE can appear in ferroelectric materials with charge disproportion, associated with off-center cations that create a net polarization. In these materials, the NTE commonly appears below their phase transition temperature. When heating below T_C, the polarized and asymmetric chain $O\cdots M-O\cdots M-O$ changes to a symmetric one $O-M-O-M-O$, as seen in the figure 2.7. The length of the bond $O\cdots M$ is because the electrons are localized in antibonding states. [1, 2]

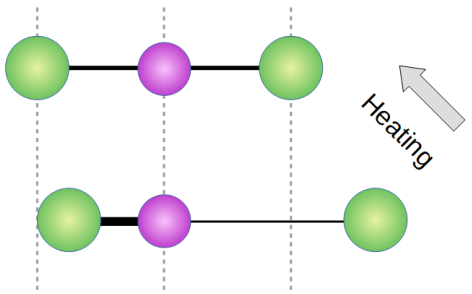


FIGURE 2.7: Schematic of the change in the chain of a ferroelectric material with charge disproportion upon heating. The asymmetric chain changes to a symmetric one, adapted from [1].

Phase transitions between antiferroelectric, ferroelectric and paraelectric imply crystal lattice changes. NTE usually arises in phase transitions of ferroelectric to antiferroelectric and ferroelectric to paraelectric.

Materials that possess this kind of NTE are for example perovskite oxides of lead, such as $PbTiO_3$ ($\alpha_V = -19.9 \times 10^{-6}$ K^{-1}, 298-763 K) [31, 32],for short PT, and $Pb(Zn_{0.66}Nb_{0.33}O_3$ ($\alpha_V = -3 \times 10^{-6}$ K^{-1}, 340-384 K) [33]; PT-based compounds such as $0.4\,PT - 0.6\,BiFeO_3$ ($\alpha_V = -39.2 \times 10^{-6}$ K^{-1}, 298-948 K) [34] and $0.7\,PT - 0.3\,Bi(Zn_{0.5}Ti_{0.5})O_3$ ($\alpha_V = -6 \times 10^{-6}$ K^{-1}, 298-773 K) [35]; and other materials such as $Sn_2P_2S_6$ ($\alpha_V = -188 \times 10^{-6}$ K^{-1}, $306 - 332$ K) [36] and $(NH_4)_2SO_4$ ($\alpha_V = -150 \times 10^{-6}$ K^{-1}, $170 - 223$ K) [37]. [4]

2.1.2.4 Charge-Transfer Transition

Charge transfer between atoms implies that one atom gives up valence electrons, becoming smaller, and the other atom that receives those electrons becomes bigger. This exchange will vary the atomic radius of both atoms. The modification of the atomic radii depends on the atomic species, electronic configuration, etc., and its effect within the crystal will depend on its position in the structure. [1]

In this category, there is a very known family, the bismuth-nickel oxides. In these oxides, upon heating, charges are transferred from Ni to Bi, which means that the Ni atomic radius contracts and that the Bi expands. Being that the atomic radius of Ni dominates the structure, due to the octahedron domination of $Ni-O$ in the lattice, it presents an NTE. [1] For example, $Bi_{0.95}La_{0.05}NiO_3$ has $\alpha_V = -413 \times 10^{-6}$ K^{-1} between 300 K and 370 K, being denominated as a colossal NTE. [2, 4, 38]

Other materials with this type of NTE are the compounds with the rare earth Sm such as $Sm_{1-x}Y_xS$ (x = 0.33, $\alpha_L = -30 \times 10^{-6}$ K^{-1}, 10-255 K) [39], $Sm_{2.75}C_{60}$ ($\alpha_V = -400 \times 10^{-6}$ K^{-1}, $T \leq 32$ K) [40] and $Sm_{1-x}Gd_xS$; and with the rare earth Yb such as $Yb_8Ge_3Sb_5$ ($\alpha_V = -1550 \times 10^{-6}$ K^{-1}, 5-15 K) [41], YbCuAl and $YbInCu_4$. In these compounds there is a charge-transfer intra-atomic that decreases the $4f$ electron number with increasing temperature. [4]

Some more examples are the A-site-ordered $A'Cu_3Fe_4O_{12}$ double perovskites where A' is a large rare earth element like La to Tb, or Sr and Bi. In this type of material, the NTE mechanism occurs due to a charge transfer transition induced by temperature. For example, in the material $LaCu_3Fe_4O_{12}$ with increasing temperature there is a charge transfer transition of $3Cu^{3+} + 4Fe^{3+} \rightarrow 3Cu^{2+} + 4Fe^{3.75+}$. However, the NTE associated with this

transfer is instantaneous, in the value of $\Delta V \approx 1.0\%$, instead of through a temperature window. [4, 42]

2.1.2.5 Metal-Insulator Transition

The Metal-Insulator Transition (MTE) occurs in the Mott transition and usually takes place at lower temperatures. In this transition, the increase of temperature leads the material to undergo a transition from an insulating state to a metallic state where its volume suffers contraction. [1]

The materials discovered with this type of transition are only as few, such as: V_2O_3, NiS and the $Ca_2(Ru_{1-x}M_x)O_4$ (M = Cr, Mn, Fe, and Cu) family. The Ca_2RuO_4 presents a colossal NTE, it has a metal-insulator transition at 357 K [43]. While heating from 150 K to 340 K, the c axis expands by 4.6 % and the axis a and b shrinks by 0.6 % and 5.0 %, respectively. Resulting in a $\Delta V/V \approx 1.0$ % [1]. Ca_2RuO_4 based compounds are for example $Ca_2(Ru_{0.933}Cr_{0.067})O_4$ ($\alpha_V = -80 \times 10^{-6}$ K^{-1}, 90-210 K) [44], $Ca_2(Ru_{0.9}Mn_{0.1})O_4$ ($\alpha_V = -32 \times 10^{-6}$ K^{-1}, 150-400 K) [45] and $Ca_2(Ru_{0.92}Fe_{0.08})O_4$ ($\alpha_V = -37 \times 10^{-6}$ K^{-1}, 150-390 K [45].[43]

Figure 2.8 resumes the different mechanisms of NTE while providing materials examples included in each category.

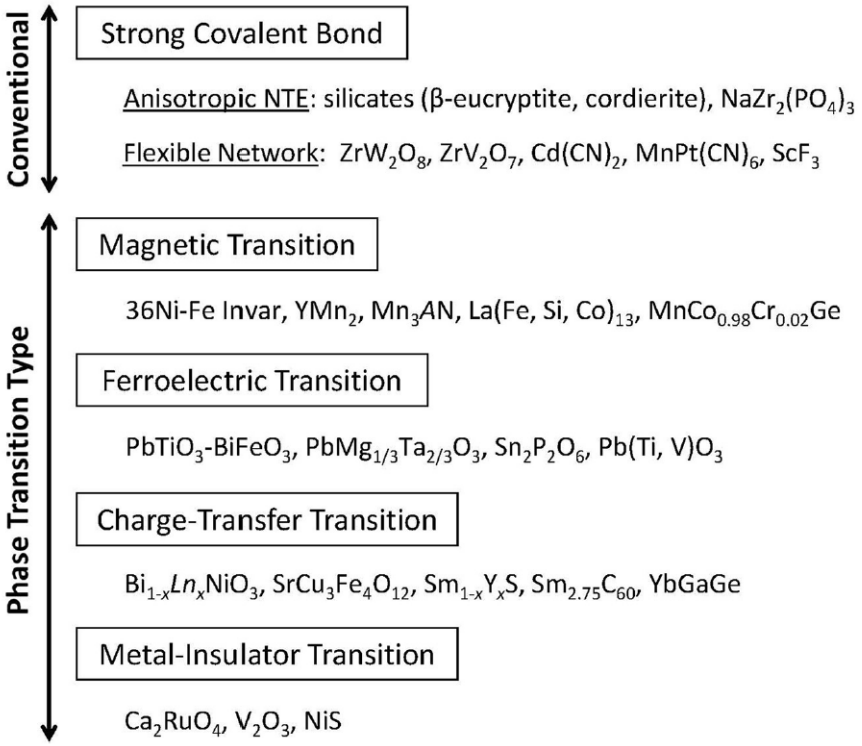


FIGURE 2.8: Summary of negative thermal expansion mechanisms and examples of materials [1].

2.2 Nanoscale Negative Thermal Expansion

Confining a material down to the nanometer scale can lead to the appearance of new physical properties due to size-induced effects. In particular, several materials that present bulk PTE have been found to exhibit NTE when presenting at least one nanoscale dimension. [2, 7]

Several characteristics can be changed by the materials size reduction, such as spontaneous polarization, superficial/interfacial coordination, local lattice symmetry, and elemental distribution. Nanomaterials own several distinctive physical properties like the peculiarities of lack of long-range coherence, abnormal superficial/interfacial bonding, lattice imperfections, and distribution of local phases. These size-dependent properties, between bulk and nanoscale, give rise to the possibility to tailor features like the lattice thermal expansion by balancing the long-range coherence and the short-range chemical bonding. However, a universal theoretical model for tailoring the thermal expansion in nanomaterials is not yet available due to the limited knowledge gathered so far. [7]

Several nanoparticles that reported NTE are magnetic insulators-based materials, e.g., CuO and MnF_2. Both these materials show NTE below their Néel temperature T_N when

reduced to 5 nm particles [2, 46]. In particular, CuO shows a giant NTE, $\alpha_V = -110 \times 10^{-6}$ K^{-1}, in the temperature range from 20 to 170 K in comparison with a CTE of its bulk counterpart ($\alpha_V = 2.1 \times 10^{-6}$ K^{-1}, 20-210 K). This means that the NTE observed in CuO nanoparticles is four times larger than the one observed in ZrW_2O_8. However, above T_N, both bulk and nanoparticle CuO present approximately the same thermal expansion [4, 46].

Au is another material with a crossover from PTE to NTE as its size and dimensions diminish to the nanoscale. With dimensions of 4 nm, nanoparticles show a $\alpha_L = -25 \times 10^{-6}$ K^{-1} between 150 K and 400 K. Whereas, Au bulk state presents a PTE of $\alpha_L = 14 \times 10^{-6}$ K^{-1}. It is also worthy of notice that the transition from PTE to NTE occurs without a transition of the atomic structure in the Au nanoparticles. However, Au nanoparticles also present a PTE more than two times larger than its bulk counterpart in the range of 15 K to 100 K, $\alpha_L = 32 \times 10^{-6}$ K^{-1}. [4, 47]

Some more examples include the PtFe alloy, as bulk shows an NTE ($\alpha_3 = -4.4 \times 10^{-6}$ K^{-1}) in one of the three axis of symmetry, and when reduced to 3.5 nm particles the NTE is enhanced in this symmetry axis ($\alpha_3 = -15.8 \times 10^{-6}$ K^{-1}) [48]. In magnetic $Gd_5(Si, Ge)_4$ it is also observed a crossover from PTE at bulk state to a NTE on nanoparticles ($\alpha_V = -32.2 \times 10^{-6}$ K^{-1}, 90-160 K; $\alpha_V = -69 \times 10^{-6}$ K^{-1}, 255-340 K) [13, 49]. Also the magnetic antiperovskite of $Mn_{3-x}Cu_{0.5}Ge_{0.5}N$ possesses NTE when reduced to a grain size of $\sim$ 2.0 μm (x = 1000, $\alpha_V = -17.1 \times 10^{-6}$ K^{-1}, 260-340 K), $\sim$ 30 nm (x = 878, $\alpha_V = -3.89 \times 10^{-6}$ K^{-1}, 160-260 K), and shows ZTE when the grain size is $\sim$ 12 nm (x = 787, $\alpha_V = -0.118 \times 10^{-6}$ K^{-1}, 12-230 K) [50]. [4]

Other materials where the CTE can be tuned by particle size and morphology include $PbTiO_3$-based compounds, $BaTiO_3$, TiO_2, ScF_3, CeO_2, etc. [7]

2.2.1 Thermal Expansion in Nanowires

There are also materials where it is possible to tune the CTE by changing the material morphology, specifically passing from bulk to NWs. A computational study performed by Ho et al. shows a "smaller is smaller" trend for the CTE of NWs when compared with their bulk counterparts. [51]

One example is that the Co NWs with 30 nm diameter were also reported to possess a lower CTE than their bulk counterpart. Also, instead of showing a linear CTE, they

revealed a quadratic CTE. The first-order CTE of $\alpha_V = 4.3 \times 10^{-6}$ K^{-1} and a second-order CTE of $\alpha_V = 5.9 \times 10^{-6}$ K^{-1} in the temperature range of 25-700 K. Whereas its bulk counterpart has a CTE of $\alpha_V = 17 \times 10^{-6}$ K^{-1}. [52]

Another case is the Cu bulk that shows a CTE of $\alpha_V = 14.8 \times 10^{-6}$ K^{-1} and when reduced to nanowires with 40 nm diameter, it has a CTE of $\alpha_V = 1.2 \times 10^{-6}$ K^{-1}, both in the temperature range of 300-700 K [53].

Ag also showed a CTE that is highly size-dependent, where the NW diameter by influencing the number of atoms on the surface also influences the CTE of the NWs [54, 55].

Bulk SnO_2 possess a positive CTEs of $\alpha_1 = 4.90 \times 10^{-6}$ K^{-1} and $\alpha_3 = 5.42 \times 10^{-6}$ K^{-1}, for axis 1 and 3 respectively, in the temperature range from room temperature to 623 K. Nanoparticle SnO_2 with grain size of $\sim$ 4 nm also have positive CTEs close to those of the bulk, $\alpha_1 = 3.45 \times 10^{-6}$ K^{-1} and $\alpha_3 = 4.70 \times 10^{-6}$ K^{-1}, for axis 1 and 3 respectively. However, SnO_2 NWs with 5nm of diameter show a near ZTE behaviour with CTEs of $\alpha_1 = 1.20 \times 10^{-6}$ K^{-1} and $\alpha_3 = 0.84 \times 10^{-6}$ K^{-1}, for axis 1 and 3 respectively. [56]

Chapter 3

Fabrication Methods

Nanowires have attracted a lot of attention through the years due to their potential applications in multidisciplinary fields, such as nanoscale electronics and microelectromechanical systems, chemical and biomedical sensors. This type of 1D nanostructures possesses other physical-chemical properties when compared to their bulk, 3D counterparts. This happens because, at the nanoscale, the quantum effects rule the properties of the materials.

1D Nanowires can be fabricated through a wide variety of techniques like laser-assisted chemical vapor deposition (CVD), oxide-assisted CVD, thermal evaporation, metal-catalyzed molecular beam epitaxy (MBE), chemical beam epitaxy (CBE), and template filling by sol-gel or electrodeposition techniques. [16]

3.1 Nanoporous Alumina Templates

The anodization of aluminum is a technique where one obtains nanoporous alumina templates (NATs). NATs can be obtained by the electrochemical oxidation of the Al under controlled anodization conditions, where it is possible to tune the size and shape of the porous arrays to the desired dimensions. These membranes have diversified applications since it is possible to fabricate arrays of nanostructures such as nanowires (NWs), nanotube (NTs), nanodots, or antidots of several materials. Also, the fabrication process is low cost and highly scalable. The PAA membranes possess highly ordered hexagonal pore arrays where pore diameter (D_p) and its corresponding interpore distance (D_{int}) vary from 6 to 200 nm and from 65 to 500 nm, respectively. [15]

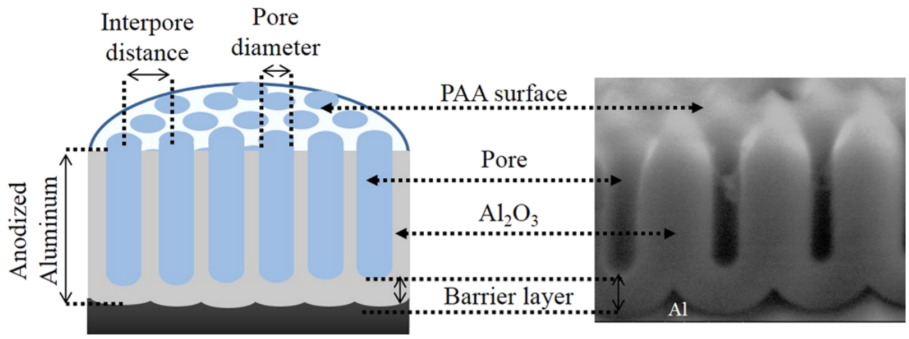


FIGURE 3.1: Schematic representation of an hexagonal ordered arrays in a NAT and corresponding cross-section view by SEM. [15]

The anodization parameters like the anodization applied voltage (V_{app}), pH, type-/concentration of the electrolyte, and temperature determines the NAM characteristics such as D_p, D_{int} and thickness of the oxide barrier layer δ_b and length of the NAT.

When a potential is applied between the cathode and the anode, an oxide layer at the top of the Al foil starts to form. The H^+ and OH^- ions concentration increase due to the water-splitting reaction at the electrolyte/oxide interface:

$$H_2O(l) \rightarrow 2H^+(aq) + O^{2-}(oxide) \tag{3.1}$$

At the same time the Al foil is oxidized at the oxide/metal interface:

$$Al(s) \rightarrow Al^{3+}(oxide) + 3e^- \tag{3.2}$$

and it reacts with the O^{2-}/OH^- ions, that because of the electric field generated, migrate across the oxide layer:

$$Al^{3+}(oxide) + 3OH^- \rightarrow Al_2O_3(s) + 3H^+ \tag{3.3}$$

$$Al^{3+}(oxide) + 3O^{2-} \rightarrow Al_2O_3(s) \tag{3.4}$$

Meanwhile, H_2 bubbles are being released at the cathode due to the migration of H^+ ions:

$$2H^+(aq) + 2e^- \rightarrow H_2(g) \tag{3.5}$$

The growth of NAT depends on the balance between the oxide formation rate at the oxide/metal interface and the of oxide dissolution rate at the electrolyte/oxide interface. The formation of oxide at the anode corresponds to the following general oxidation equations:

$$2Al(s) + 3H_2O(l) \rightarrow Al_2O_3(s) + 6H^+(aq) + 6e^- \tag{3.6}$$

and the dissolution of the oxide corresponds to:

$$Al_2O_3(s) + 6H^+(aq) \rightarrow 2Al^{3+}(s) + 3H_2O(l) \tag{3.7}$$

The NAT is composed of two types of oxide, an inner layer of dense-pure alumina and an outer layer of alumina at the pore walls (anion-contaminated), as shown in figure 3.2.

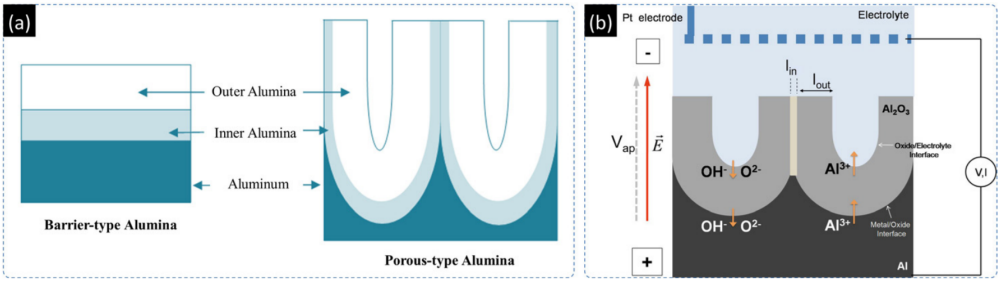


FIGURE 3.2: a) Schemes of two types of alumina barrier, barrier-type on the left and porous-type on the right, with the inner and outer oxide layers indicated. b)Schematic representations of the electrochemical processes at the anode, electrolyte/oxide and oxide/metal interfaces.[15]

In the alumina formation, there is a volume expansion that causes mechanical stress. This leads to the formation of small irregularities in alumina formed at the electrolyte/oxide interface. In the regions where alumina is thinner, there will be a concentration of the electric field. Consequently, H^+ ions concentration increases leading to the field-enhanced oxide dissolution in those regions, and the pores start to nucleate. After the nucleation, there is a pore competition where bigger pores encompass smaller pores, improving organization. With the mechanical stress, the pores continuously grow downwards at a constant rate and form hexagonally ordered arrays through a self-assembling process. The oxidation rate is equivalent to the dissolution rate leading to a constant oxide layer barrier at the bottom of the pores.

Figure 3.3 represents the typical curve of the anodization time-dependent current density transient. These characteristic curves are well established and provide an insight into the NAT formation, where one can observe the main growth mechanisms stages of the pore growth. In the first stage (I), an accentuated drop of current is caused by forming a thin layer of oxide that increases the resistivity. The second stage (II) corresponds to the pores nucleation stage, where the pores start to nucleate where the oxide layer is thinner due to filed-enhanced the dissolution of the oxide. In this stage, the rate of oxide growth and its dissolution are matched. In the third stage (III), the current increases due to an increase in the dissolution rate of alumina. As the conducting paths appear, the resistance

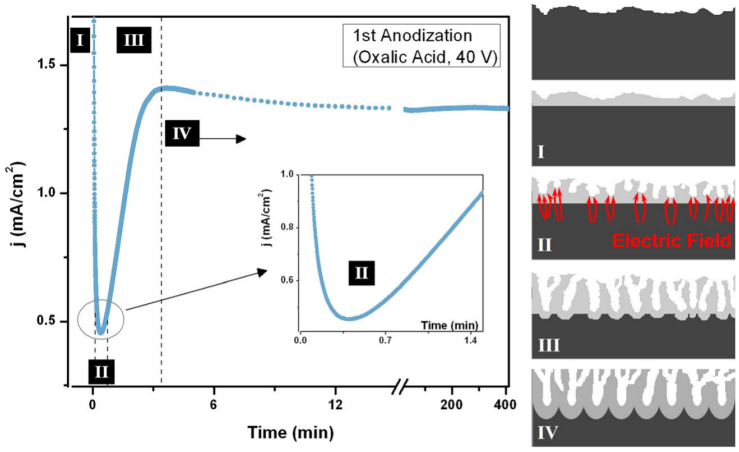


FIGURE 3.3: Typical current density curve with the identification of the four main pore growth stages[15].

of the system decreases. The fourth stage (IV) is characterized as a slight drop of current corresponding to the pore competition. Finally, a steady-state current value is achieved, where the oxidation and dissolution rate equilibrium is reached, resulting in a constant growth rate of the nanopores.

In order to obtain a highly organized NAT, a two-step anodization method is used. This method consists of long first anodization that allows the formation of organized nanopores at the interface oxide/metal. The pores nucleate randomly on the Al surface in the first anodization, mostly in places with defects. After a certain amount of time, the pores start to self-assemble due to mechanical stress caused by neighboring pores. By removing the formed NAT by a chemical etching, a pattern is left established at the surface of the Al foil. Then, second anodization, in the same conditions, is performed, obtaining highly ordered NATs. This happens because the pore nucleation sites are already well defined in a pattern at the Al surface, creating preferential conditions to the pore growth. So the pores grow already aligned and organized due to the field enhanced dissolution at these sites.

The most common fabrication process of NATs is through the conventional 'mild-anodization' (MA) conditions. Under MA, the fabrication requires several days of processing time, presenting a slow oxide growth rate, $2 - 6\mu m h^{-1}$, depending on the electrolyte. There is an alternative process using 'hard-anodization' (HA) conditions. The HA has a high-speed oxide growth, $50 - 100\mu m h^{-1}$, depending on the electrolyte, which enables a simple and fast fabrication of NATs. [57]

The typical MA uses three well-studied types of electrolytes (see table 3.1) sulfuric

(H_2SO_4, 0.3 M), oxalic ($C_2O_4H_2$, 0.3 M) and phosphoric (H_3PO_4, 0.1 M) acids, with suitable potentials of 25, 40 and 195 V, respectively. On those regimes, one can obtain PAA membranes with pore diameters of 20, 35 and 200 nm, and D_p of 65, 105 and 500 nm, respectively.

Electrolyte	Concentration (M)	Potential (V)	Temperature (°C)	D_p (nm)	D_{int} (nm)	Anodization Rate (μ m h^{-1})
H_2SO_4	0.3	25	1	25	65	5
$C_2O_4H_2$	0.3	40	4	40	105	2.5
H_3PO_4	0.1	195	1	180	480	5

TABLE 3.1: Mild anodization typical conditions.

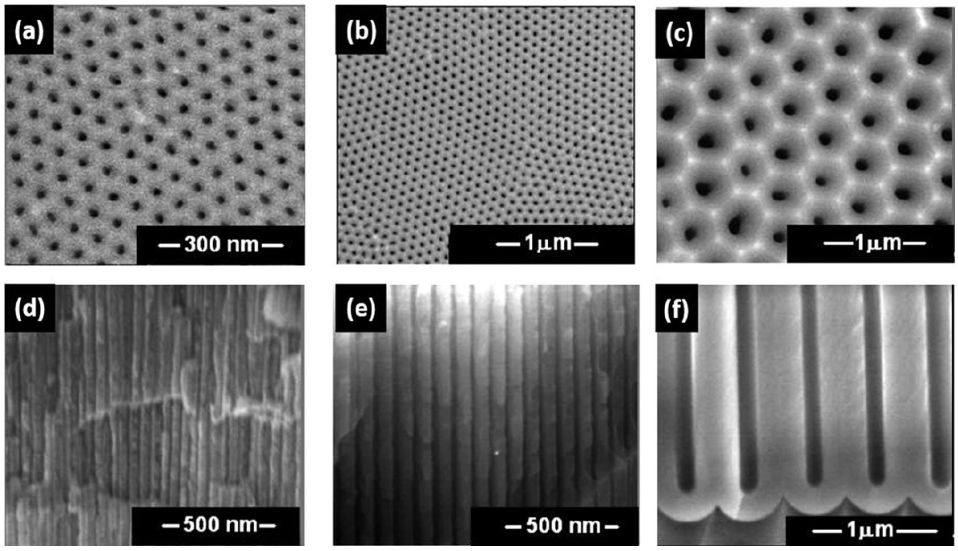


FIGURE 3.4: SEM images of NAT[a),b) and c) top surface; d), e) and f) cross-section] fabricated under various anodization conditions: a) and d) 0.3 M sulfuric acid with $V_{app} = 25V$; b) and e) 0.3 M oxalic acid with $V_{app} = 40V$; and a) and d) 0.1 M phosphoric acid with $V_{app} = 195V$. [15]

The fabrication of PAA membranes through HA requires first forming an oxide layer at MA conditions. This first process is fundamental to prevent dielectric breakdown effects. Then, the anodization voltage can be increased until it reaches the chosen voltage (100-150 V, for oxalic acid at 0.3 M) at a constant rate. The HA is finally carried at a constant potential that is usually chosen depending on the desired D_p and D_{int} geometric parameters. The typical anodization curve of a HA differs from the one of MA. The time-dependent current density transient of the HA shows a nearly exponential decrease. Due to the rapid growth of a homogeneous film, there is diffusion-limited electrochemical oxidation of aluminum at the pore bottom, which causes this unusual behavior. The anodization current is correlated with the movement of the ionic species (O^{2-}, OH^-,

Al^{3+}) between the electrolyte and the oxide/metal interface. The mobility of ions determines the current density during the anodization process. With this being, as the pores grow, extending the diffusion path, it is expected that the current density slowly decreases over time. So, the HA does not possess a linear growth rate of PAA due to its diffusion-limitation. [57]

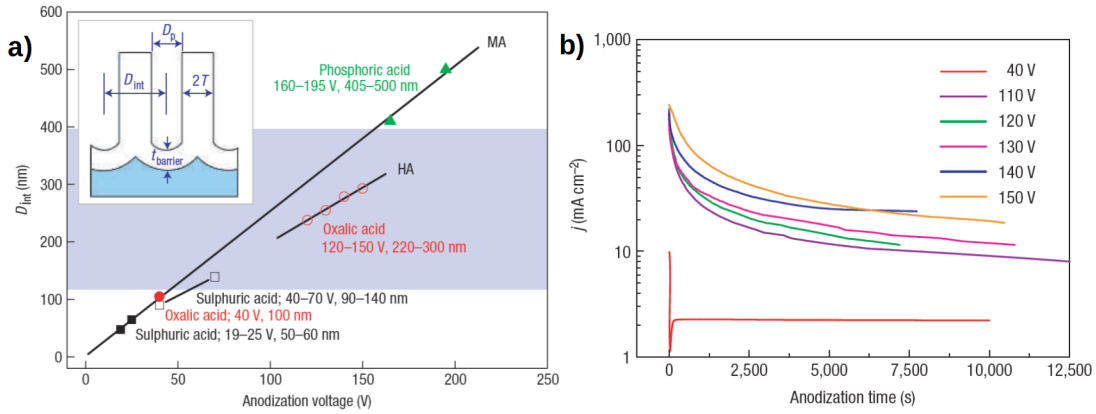


FIGURE 3.5: Comparison of mild anodization with hard anodization. a) Interpore distance (D_{int}) versus anodization voltage (V_{app}) for MA and HA. b) Current density curves for HA and MA using 0.3 M oxalic acid as electrolyte. [57]

The porosity of the NATs obtained through MA and HA process is given by the equation:

$$P = \frac{2\pi}{\sqrt{3}} \left(\frac{D_p}{2D_{int}} \right)^2 \tag{3.8}$$

Eq. 3.8 is the so called 10 % porosity rule proposed bt Nielsch et al., according to this, a porosity of $\sim$ 10% is required for an hexagonal pore distribution for membranes fabricated under MA conditions. This value ensures a self-ordering regime, independently of the anodization conditions. [58] Under HA conditions, Lee et al. suggests that the optimum porosity should be $\sim$ 3.3% for a self-ordering regime. [57]

Additionally, for HA, the barrier oxide layer (δ_b) is remains constant throughout the anodization process, as previously stated for MA. This parameter is also correlated with the applied voltage (V_{app}), since $D_{int} \approx 2\delta_b$ and $D_{int} = k\ V_{app}$. However, the proportionality constant, k, differs between MA and HA. Accordingly to Lee et al. $k = 2.5nmV^{-1}$ for MA and for HA $k = 2.0nmV^{-1}$.

3.2 Electrodeposition

One of the most commonly used methods for the growth of metallic NWs in templates is electrochemical deposition, also called electrodeposition. It can also be used for the growth of thin films in conducting substrates. This method involves applying a voltage between the cathode, conducting substrate (working electrode), and the anode, Pt mesh (counter electrode). A third electrode (reference electrode) can also be used. The system is immersive in an ionic electrolyte with the metallic ionic species. Due to the applied potential, the metallic ions are driven to the conducting substrate, where they are electrochemically reduced, resulting in the metallic material growth on top of the substrate. The reduction of the metallic ions corresponds to the general expression:

$$(M_x W_y)^z + nxe \rightarrow xM^0 + yW \tag{3.9}$$

where M is the metallic ion and W is a molecule, ion, or radical bounded to M, both forming the complex species $(M_x W_y)^z$, n represents the number of electrons involved in the reaction.

For the electrodeposition of one atom of metal, n electrons are required, corresponding to a charge of ne Coulombs. By measuring the amount of current (I) that flows through the circuit, one can estimate the net charge (Q) used to reduce the metal ions. This process follows Faraday's law of electrolysis. Thus the deposited metal mass (m, in g) can be estimated using the following expression:

$$m = \frac{QM}{nF} \tag{3.10}$$

where M is the atomic weight of the metal and F is the Faraday's constant (96485 C mol^{-1}). This equation is highly important because it allows the estimation of the amount of metal material of the electrodeposited in the working electrode.

The electrodeposition of NWs into a template can be performed with three different methods: direct-current (DC) electrodeposition, alternating-current (AC) electrodeposition and pulse electrodeposition (PED), as represented in the figure 3.6.

DC electrodeposition requires a free-standing membrane of alumina, which is called nanoporous alumina membrane (NAM), which means that the Al needs to be removed as well as the bottom of the pores of alumina (figures 3.6 and 3.7). Also, because an electric contact is needed for electrodeposition, a thin metal film is deposited on one of the

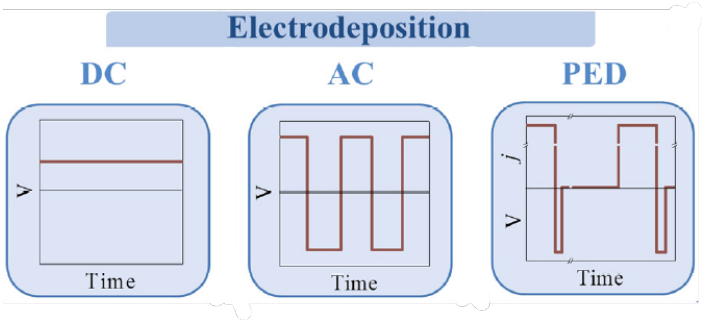


FIGURE 3.6: Representation of the three different methods of electrodeposition to fill NAT [15].

membrane surfaces. Then electrodeposition (potentiostatic applied potential) can occur, using a three-electrode method.

For the AC electrodeposition (figures 3.6 and 3.7), the alumina barrier must have a thickness less than 10 nm. To achieve that thickness, a decreasing potential in successive steps is applied. Since the barrier layer thickness (δ_b) depends on the applied potential (V_{app}). This process of thinning the barrier creates dendrites at the bottom of the pores. The electrodeposition using alternating current is then able to occur through such a thin barrier.

The pulsed electrodeposition (figures 3.6 and 3.7) also requires the alumina barrier to be thinned, so the same process from the AC electrodeposition is used. In this type of electrodeposition, consecutive cycles with three different pulses are applied: the first pulse at constant current, a second pulse with opposite polarity and then a resting pulse (V=0).

3.2.1 Nucleation and Growth Mechanisms

When electrodeposition in plan substrates is performed, there are two growth stages, nucleation and growth. The growth occurs after the nucleation when the nuclei increase beyond their critical size. These two mechanisms are decisive of the grain size of the electrodeposited material. Besides that, they can also be classified into diffusion (or mass) controlled and interfacial (or charge) controlled processes. The mass transfer process presupposes the movement of species from one location to another within the solution. So, the growth of the material is limited by the rate at which the species are transported through the solution to the electrode surface. However, the growth in a charge-transferred reaction is controlled by how fast two species can be brought together. This case is related to how fast metallic ions are driven to the electrode to be reduced by the electrons.[59]

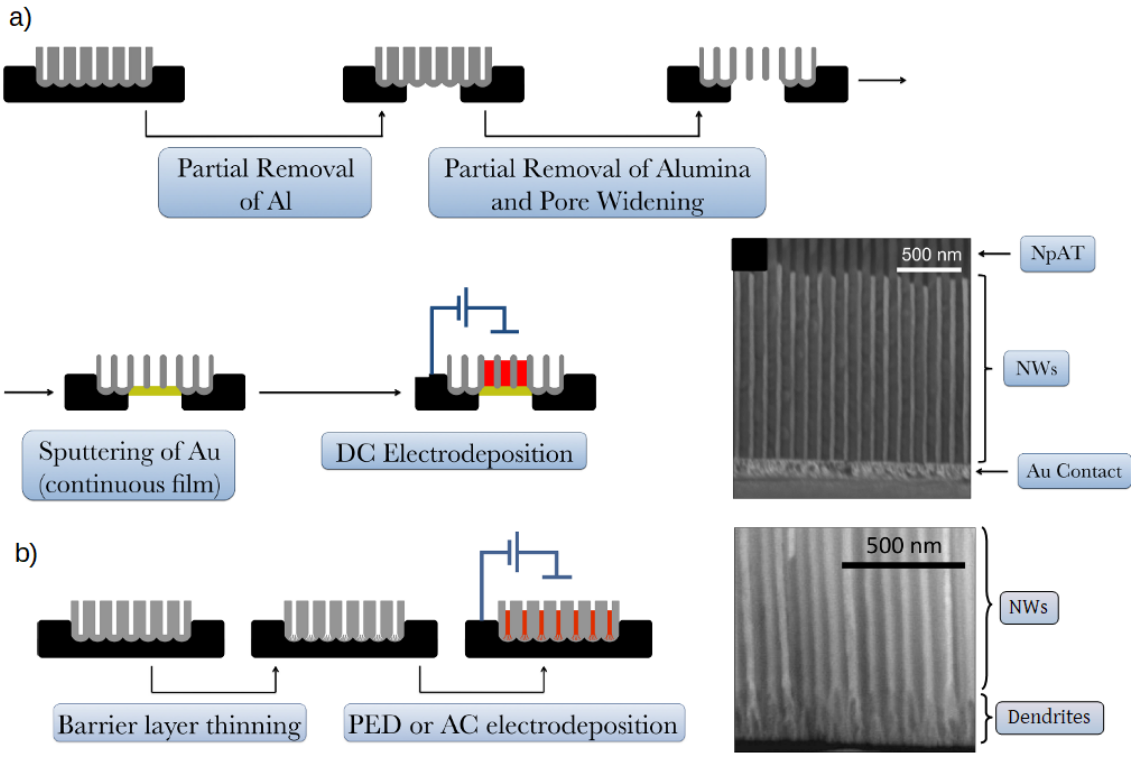


FIGURE 3.7: Schematic representation of the template preparation to grow NWs using a) DC electrodeposition and b) AC or pulsed electrodeposition [15].

Electrodeposition curves have a characteristic behavior which is presented in the figure 3.8. Firstly, there is the decline of current density corresponding to the double layer charge on the electrode surface. Then, the current density increases until it reaches its maximum value. This corresponds to the process of nucleation and growth. And finally, the current density decreases slowly due to the diffusion of the species from the electrolyte to the interface electrode/solution. [59, 60]

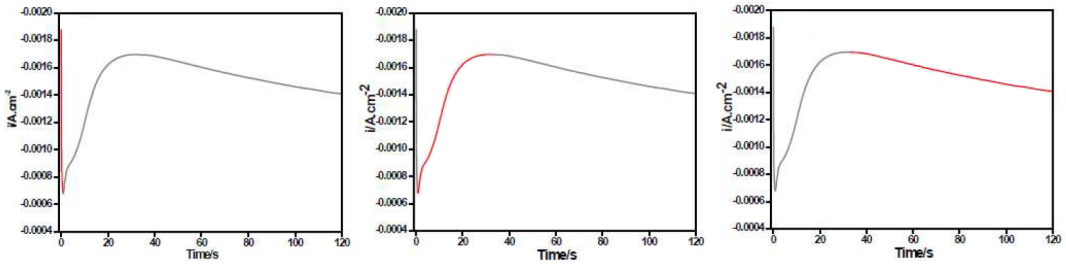


FIGURE 3.8: Different stages of electrodeposition: charge of the electric double layer at the electrode; nucleation/growth; and continuous deposition ,adapted from [59]

Theoretical models for the nucleation phase consider two extreme cases: instantaneous and progressive nucleation. Instantaneous nucleation assumes that all the nuclei are formed simultaneously, at the beginning of the electric pulse, and grow slowly. In the

progressive case, new nuclei are continuously formed during the electrodeposition, and the growth is relatively fast. Besides the nucleation being classified as instantaneous or progressive, it can also be classified as a 2D or 3D type of nucleation. The theoretical models for the 2D nucleation mechanism and kinetics were developed by Bewick and Thomas and are given by:

$$\frac{j}{j_m} = \frac{t}{t_m} exp\left(\frac{1}{2}\left[1 - \left(\frac{t}{t_m}\right)^2\right]\right) \tag{3.11}$$

for a 2D instantaneous nucleation, and:

$$\frac{j}{j_m} = \left(\frac{t}{t_m}\right)^2 exp\left[\frac{2}{3}\left[1 - (\frac{t}{t_m})^3\right]\right) \tag{3.12}$$

for a 3D progressive nucleation. The 3D models were developed by Scharifker and Hills and are given by:

$$\frac{j^2}{j_m^2} = \frac{1.9542t}{\frac{t}{t_m}}\left(1 - exp\left[-1.2564\left(\frac{t}{t_m}\right)\right]\right)^2 \tag{3.13}$$

for a 3D instantaneous nucleation, and:

$$\frac{j^2}{j_m^2} = \frac{1.2254t}{\frac{t}{t_m}}\left(1 - exp\left[-2.3367\left(\frac{t^2}{t_m^2}\right)\right]\right)^2 \tag{3.14}$$

for a 3D progressive nucleation. For all equations, j represents the current density throughout the electrodeposition time t, j_{max} represents the maximum current density obtained which has a corresponding t_{max}. [61, 62]

The equations presented above usually are only accurate in the first two stages of electrodeposition, according to the figure 3.8. When $t > t_m$ the theoretical curves tend to deviate from the experimental ones, this happens because the theoretical models presuppose that the nucleation/growth occurs on a smooth surface. However, normal electrode surfaces have dislocations and scratches that provide additional active nucleation sites. [63] Besides this reason, there may also be the presence of other electrochemical processes that contribute to the total current, for example, a proton reduction process. [63, 64] Therefore, Palomar-Pardavé et al. proposed a nucleation/growth model that takes into account further reactions that take place on the surface of interacting growing nuclei [65]. With this being, the overall current density for a diffusion-limited 3D growth is given by:

$$j_{Total}(t) = \left(P_1 + P_4 t^{-1/2}\right) \times \left(1 - exp\left[-P_2\left(t - \frac{1 - exp(-P_3 t}{P_3}\right)\right]\right) \tag{3.15}$$

where:

$$P_1 = z_{PR} F k_{PR} \left(\frac{2cM}{\pi\rho}\right)^{1/2}$$

$$P_2 = N_0 \pi k D$$

$$P_3 = A$$

$$P_4 = \frac{2FD^{1/2}c}{\pi^{1/2}}$$

$$k = \left(\frac{8\pi c}{\rho}\right)^{1/2}$$

where c is the concentration of the metal ions in the bulk of the solution; F is the Faraday constant (C mol^{-1}); $z_{PR}F$ is the molar charge (C mol^{-1}) in the hydrogen ion reduction; k_{PR} is the rate constant of hydrogen evolution reaction (mol cm^{-2} s^{-1}); A is the nucleation rate (s^{-1}); N_0 is the largest nuclear number density or surface active site number (cm^{-2}). [63, 65]

Chapter 4

Iron Cobalt Alloys

FeCo alloy has drawn attention in the last years due to several appealing magnetic properties like high saturation magnetization, high Curie temperature (T_c) and permeability [8, 66, 67], low coercivity and low hysteresis losses [68]. Since magnetic nanostructures have attracted great interest in the industry due to their diversified applications in microwave devices, thermo-magneto-electric devices [66], magnetic recording head, drug-delivery [8], magnetic hyperthermia [69], etc., FeCo alloys are promising candidates for all these applications. However, the magnetic properties of FeCo alloys are highly affected by their stoichiometry. Besides these magnetic applications, these alloys are also used for catalysts for water splitting [69–72] and also for batteries such as zinc-air batteries [73] and alkaline flow batteries [74]. With this, the functionalities of the FeCo alloys are highly dependent on their stoichiometry. [68]

4.1 Magnetostriction

As previously seen in chapter 2, one of the mechanisms of NTE arises from a magnetic transition, which is associated with magnetovolume coupling. As stated before, the alloy FeCo is considered an invar alloy by Wasserman in the composition range of Fe_xCo_{1-x} $0.05 \leq x \leq 0.25$, where it shows a transition from an fcc structural phase to a bcc one as shown in the phase diagram of the FeCo bulk alloys in figure 4.2. [5] The magnetostriction in Fe_xCo_{1-x} was intensively studied in order to understand its underline mechanisms.

In 2011, Hunter et al. published a study on the dependence of magnetostriction with the composition and thermal process of Fe_xCo_{1-x} ($0.1 \leq x \leq 0.9$) thin film alloys. The study was performed in thin films with thickness of 0.50 ± 0.01 μm at room temperature

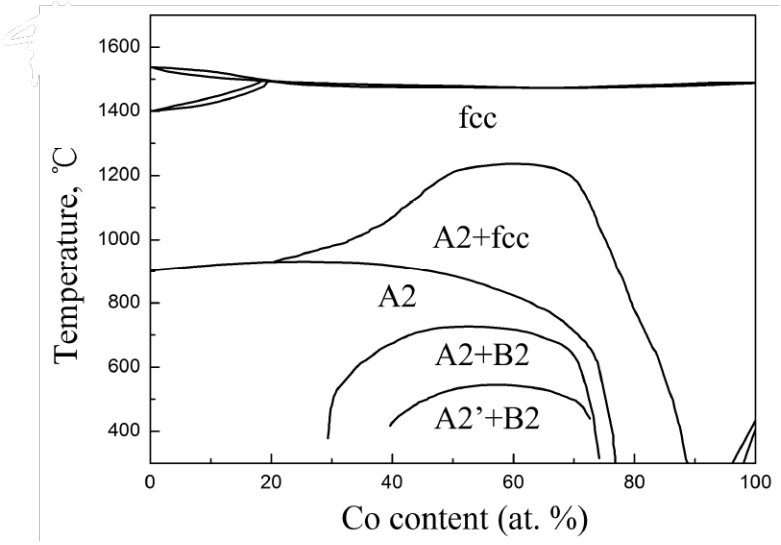


FIGURE 4.1: Iron-cobalt bulk phase diagram [75] [10].

under a low magnetic field. Three types of sample preparation were also studied: as-deposited, annealed and slow-cooled, and annealed and water-quenched. The last two were annealed at 800 °C for 1h. Measurements of magnetostriction revealed that all water-quenched samples possess higher values for this quantity, having a maximum of 260 ± 10 p.p.m. for the composition $Fe_{34}Co_{66}$, as shown in figure 4.2. The slow-cooled samples have two maximums being them 103 ± 6 p.p.m. and 156 ± 7 p.p.m., for compositions of $Fe_{60}Co_{40}$ and $Fe_{34}Co_{66}$, respectively. And the as-deposited samples also possess two maximums in magnetostriction, 67 ± 5 p.p.m. and 84 ± 5 p.p.m., for compositions of $Fe_{56}Co_{44}$ and $Fe_{22}Co_{73}$, respectively (figure 4.2).

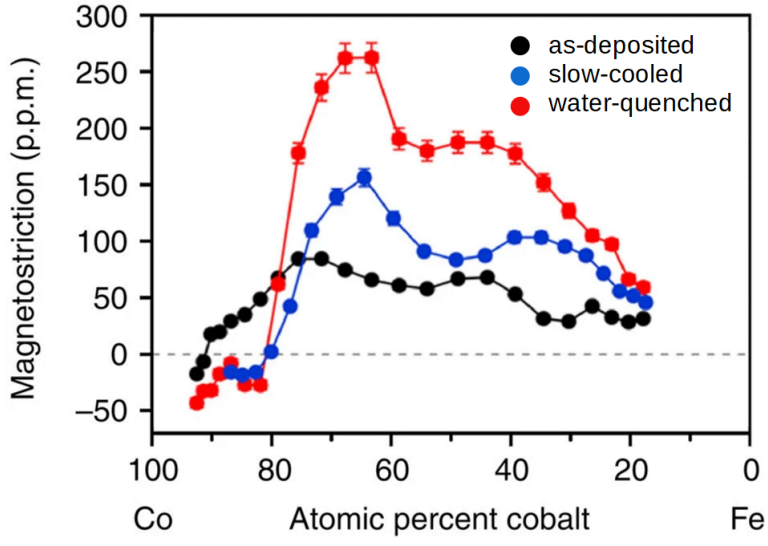


FIGURE 4.2: Magnetostriction of Fe_xCo_{1-x} thin films versus at. % of Co for differently prepared thin films, adapted from [9].

In this work, it was also shown that the FeCo alloy magnetostriction was profoundly connected to their structural phase, as well as to thermal treatments being the enhancement of magnetostriction linked to the phase diagram region where the phase interface (fcc+bcc)/bcc lies. Evolving from the bcc α-Fe phase (represented as A2 in the phase diagram) to an fcc+bcc phase, corresponding to the precipitation of fcc Co into the α-Fe matrix. The precipitates cause tetragonal distortions in the matrix that are at the origin of the magnetostriction. So, with increasing Co content, Co precipitates firstly increase the magnetostriction until it reaches a peak and then induce a magnetostriction signal shift, from positive to negative at approximately at. % of Co of 90 for as-deposited and 80 % for water-quenched and slow-cooled.

The slow-cooled samples present the B2 phase, which implies order, and according to the experimental results, suppresses the magnetostriction. However, the magnetostriction is still higher than for the as-deposited samples. The samples that were water-quenched do not exhibit the B2 phase. Nevertheless, both samples, slow-cooled and water-quenched, possess fcc precipitates. The peak of magnetostriction for both these samples was dislocated when compared with the as-deposited sample. This happened because they were annealed at 800 ºC, which is in the boundary transition bcc to bcc+fcc and corresponds to a composition of $Fe_{34}Co_{36}$. Hunter et al. proposed that the magnetostriction of FeCo alloys arises from the reorientation of the fcc tetragonal precipitates in the A2 matrix due to a magnetic field where a mixture of the bcc phase with the fcc enhances the magnetostriction.

Yamaura et al. presented a study of magnetostriction in Fe_xCo_{1-x} $(0.1 \leq x \leq 0.5)$ bulk alloys, where it was revealed that the appearance of the fcc phase cause the magnetostriction to decrease and even turn negative for Co content over 80% [12], as shown in figure 4.3. The maximum of magnetostriction, 108 ± 5 p.p.m., was obtained for the as-forged $Fe_{25}Co_{75}$ alloy. The annealed samples possess higher magnetostriction in the 50 - 70 *at*. % Co range, similarly to the results obtained by Hunter et al. for the slow-cooled samples. This enhancement may be caused by microstructure change with the release of strain and internal stress. Also, the peaks for magnetostriction of the annealed alloys are dislocated compared to the forged alloy, as previously seen.

Han et al. studied the influence of B2 and fcc nano inclusions in the magnetostriction. The Fe_xCo_{1-x} bulk alloys were prepared by arc melting and then annealed at 1000 ºC. The XRD patterns of Fe_xCo_{1-x} bulk alloys is presented in figure 4.4. One can observe that

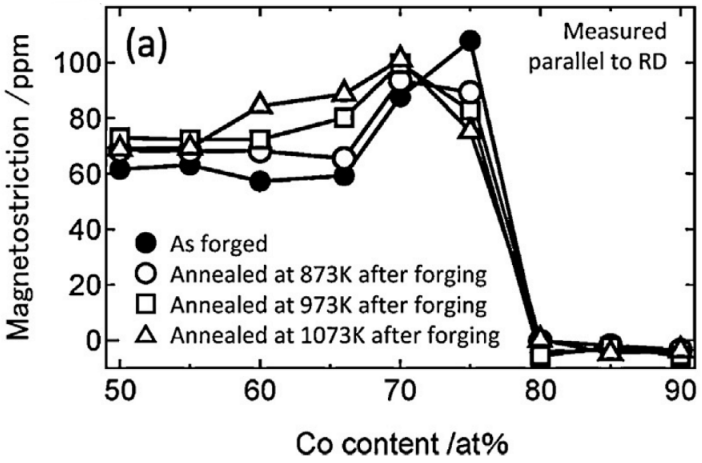


FIGURE 4.3: Magnetostriction of bulk FeCo alloys versus at. % of Co for different annealing temperatures [11].

compositions with $10 < x < 78$ present a single bcc structure, but the x = 80 sample is a mixture of fcc and bcc, and the samples with $x \geq 85$ are single-phase fcc.

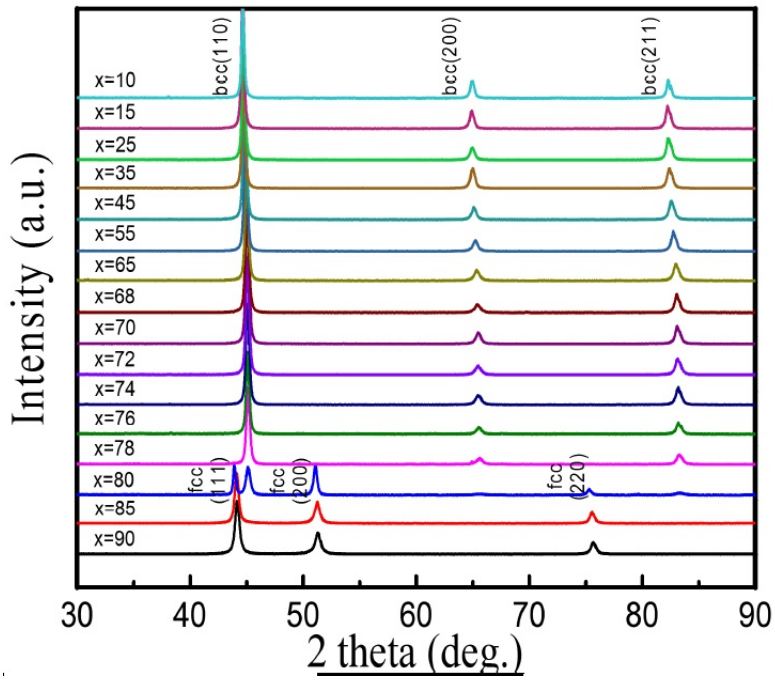


FIGURE 4.4: The XRD patterns of Fe_xCo_{1-x} bulk alloys with fcc and bcc peaks index [10].

Results show that the magnetostriction starts to increase for x = 35, with the appearance of the B2 phase. A maximum of 137 p.p.m. is obtained for $Fe_{30}Co_{70}$. Then a sharp drop for $x > 78$ occurs, associated with the fcc + A2 phase region. Both changes in magnetostriction reflect the appearance of nano inclusions, B2 or fcc, in the disordered bcc A2 matrix.

Analyzing the as-cast $Fe_{35}Co_{65}$ alloy, they observed that the ordered B2 structure can induce anisotropic tetragonal lattice distortions of the matrix and is responsible for the magnetostriction enhancement. By annealing these alloys at several temperatures then brine quenched them, they registered that annealing temperatures of 500 ºC, 700 ºC and 800 ºC correspond to B2 nano inclusions of 15 nm, 3-5 nm and > 2 nm, respectively. As represented in figure 4.5 a), the maximum magnetostriction was obtained for the alloy annealed at 700 ºC because the B2 and A2 phases only coexist until 700 ºC. Also, alloys with B2 nano inclusions with a surface/volume ratio of $3/r$, where r is the radius of the nanoinclusion, show higher magnetostriction.

Several $Fe_{22}Co_{78}$ alloys were annealed then brine quenched. The magnetostriction was almost the same until annealing temperatures of 500 ºC, and then it starts to drop (see figure 4.5 b). This is consistent with the phase transition from A2 to A2 + fcc for this stoichiometry, where the fcc volume fraction starts to increase.

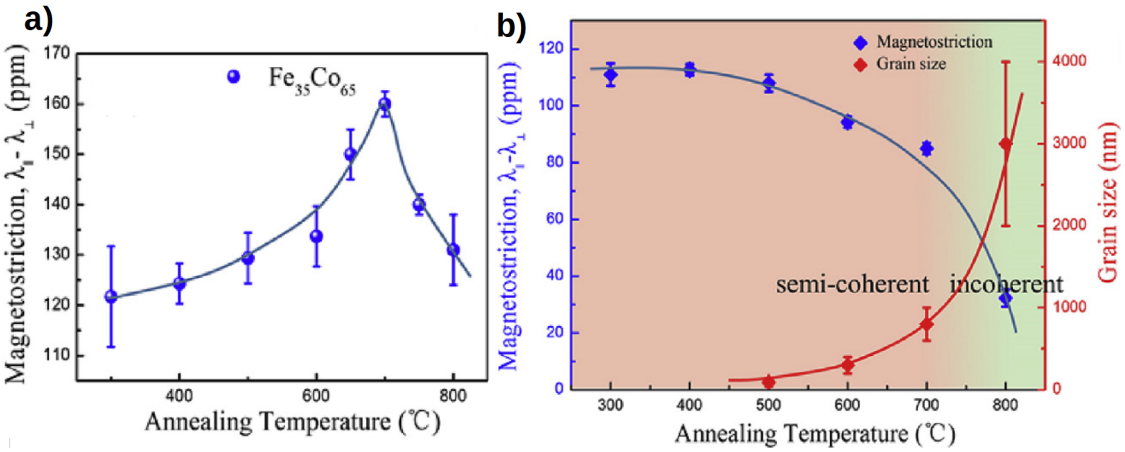


FIGURE 4.5: Magnetostriction versus annealing temperature for bulk alloys a) $Fe_{35}Co_{65}$ and b) $Fe_{22}Co_{78}$, adapted from [10].

This study is very important for explaining the magnetostriction in FeCo alloys, where they establish a correlation between the tetragonal deformations and magnetostriction. By demonstrating that it is possible to change the magnetostriction by tuning the size of B2 and fcc nano inclusions in the A2 matrix.

4.2 Thermal Expansion

Thermal expansion of FeCo alloys is a topic, to the best of our knowledge, only explored by Takahashi et al. in 1976 where they explored the invar characteristics of FeCo bulk alloys [14]. A magnetovolume coupling was registered for alloys with different stoichiometries, wherein the fcc + bcc $\rightleftharpoons$ fcc ($\alpha + \gamma \rightleftharpoons \gamma$) phase transformation is observed spontaneous magnetostriction leading to an abrupt and gradual contraction of the material. As observed in figure 4.6, the thermal expansion of the different alloys is almost invariant in a wide range of temperatures. Then, a decrease in CTE appears and apparently, NTE arises. By comparing this figure in the phase diagram of bulk FeCo (figure 4.1), one can observe that it is for the composition of 77 % of Co that the transition occurs in a wider range of temperatures. This is because, for this composition, the structural phase fcc + bcc is present for a longer range of temperatures.

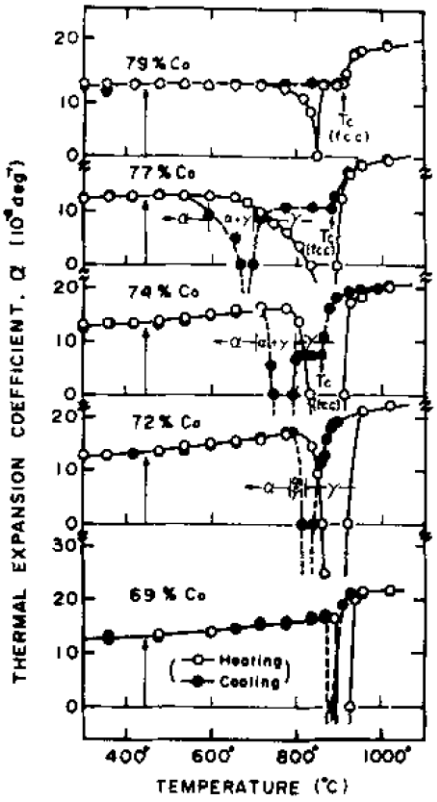


FIGURE 4.6: Temperature dependence of the CTE of $Fe_{100-x}Co_x$ x = 69, 72, 74, 77 and 79) alloys in heating and cooling [14]

Considering this topic, there is still a lot to unravel, being that little to no studies have been done to present a model of the TE in FeCo alloys.

4.3 FeCo Nanowires - Properties

$Fe_{52}Co_{48}$ NWs fabricated by electrodeposition in NAMs with D_p of 200 nm, using a constant current density, and a solution consisting of cobalt sulfate heptahydrate ($CoSO_4 \cdot 7\,H_2O$), iron sulfate heptahydrate ($FeSO_4 \cdot 7\,H_2O$), vanadium oxide sulfate hydrate ($VOSO_4 \cdot xH_2O$), and ascorbic acid($C_6H_8O_6$) and, additionally, nitric acid (HNO_3) to adjust the pH, were studied magnetically and structurally. Magnetic properties of $Fe_{52}Co_{48}$ nanowire arrays with approximately 200 nm diameter shown magnetic hysteresis curves typical of soft ferromagnetics with an easy axis parallel to the array direction due to strong shape anisotropy. The coercivity (H_c) value registered under magnetic field applied parallel ($H_{\parallel}$) was 326 Oe, and applied perpendicular ($H_{\perp}$) 150 Oe. The structural analysis revealed a bcc structural phase exhibiting the peaks corresponding to FeCo (110), (200) and (211), which is identical to what is observed for the bulk (figure 4.4). [76]

The influence of diameter modulation on magnetic properties was studied for straight $Fe_{50}Co_{50}$ NWs with a diameter of 60 nm and diameter modulated $Fe_{50}Co_{50}$ NWs with a diameter of 60/120 nm. NATs were fabricated by HA, where the ones with modulated pores were obtained by alternating the HA potential in consecutive intervals. The NWs were produced by AC-pulse electrodeposition on NATs, a sinusoidal AC wave of 18 V. The electrolyte contained 0.3 M $CoSO_4 \cdot 7\,H_2O$, 0.3 M $FeSO_4 \cdot 7\,H_2O$, 1 g/l $C_6H_8O_6$ and 45 g/l boric acid (BH_3O_3) with pH $\sim$ 5 at 30 ºC. The structural analysis showed a bcc structural phase with (110) orientation and a lattice parameter of 2.85 $\AA$. Magnetic analysis revealed that the squareness (SQ) of the magnetic hysteresis loop from the NWs with modulated diameter is significantly improved when compared with straight diameters. NWs with modulated diameters presented $H_c = 74$ mT and $SQ = 92$ % while the straight NWs presented $H_c = 84$ mT and $SQ = 60$ %. [77]

Although there is no demagnetizing field (H_d) in a single long wire magnetized along its axis, in an array of NWs, the summation of all the wires produces a demagnetizing field like a normal uniform magnetized piece of material. The demagnetizing field is proportional to the average saturation magnetization (M_s):

$$H_d = -fM_s \tag{4.1}$$

where M_s is 1.5 MAm^{-1} for FeCo accordingly to Esmaeily et al. and f is the fill factor of the template. Here they considered that the fill factor would be the ratio of the NW cross-section to the area of a hexagonal unit cell in alumina. So, for NWs of radius r and

spacing d, there's:

$$f = \frac{2}{\sqrt{3}}\pi(\frac{r}{d})^2 \tag{4.2}$$

In diameter modulated NWs, there is a H_d that acts on the center of the segments due to the magnetic charge on the rims of the wide segments. This demagnetizing field is also proportional to the M_s:

$$H_d = gM_s \tag{4.3}$$

Here, f is replaced by the g factor that can be estimated as:

$$g = 1.2(r_1^2 - r_2^2) \cdot \frac{l_1}{(l_1 + l_2)^3} \tag{4.4}$$

where r_1 and r_2, l_1 and l_2 are the radii and length of thick and thin segments, respectively. The factor 1.2 is derived from $\sum(1/n^3)$. A $f = 0.052$ and $g = 0.0005$ was obtained.

The authors concluded that the stray field of modulated wires reduces the demagnetizing field while improving the SQ. So, it is possible to tune the soft magnetic properties of the NWs by modifying their diameter profile, and the SQ of the magnetic hysteresis loop can be improved (figure 4.7). [77]

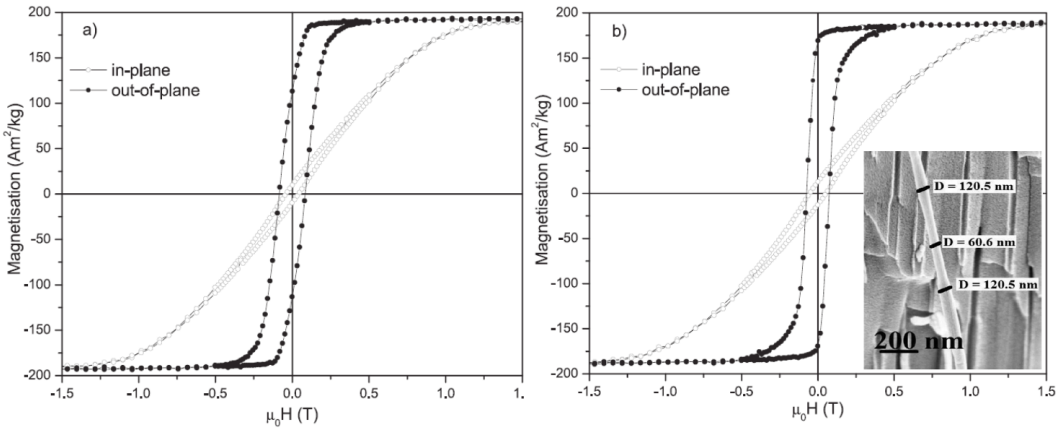


FIGURE 4.7: Magnetic curves of $Fe_{50}Co_{50}$ NWs with (a) diameter of 60 nm and (b) diameter modulated of 60/120 nm, with coercivities of 84 mT and 74 mT, respectively [77].

Equiatomic FeCo NW array were synthesized by electrochemical deposition using a potential of -1 V at $\sim$ 25 ºC in NAMs with pore diameters of 70 nm and D_{int} of 100 nm. The electrolyte consisted in 0.2 M $CoSO_4 \cdot 7\,H_2O$, 0.15 M $FeSO_4 \cdot 7\,H_2O$, 0.01 M $C_6H_8O_6$. XRD measures, performed in NWs with length of 20 μm, revealed a bcc structural phase exhibiting two peaks at (110) and (211). [67]

The influence of NW length L in the magnetic properties of an equiatomic FeCo NW array was also studied [67]. Starting with the study of effective magnetic anisotropy, this

property can be influenced by the shape anisotropy that depends on the aspect ratio and favors the easy axis along the NW; the dipolar interaction that results in a magnetostatic coupling among NWs and favors the alignment of the magnetization perpendicular to the NWs; the magnetocrystalline anisotropy (M_{mc}); and the magnetoelastic anisotropy (M_{me}) that depends on the mechanical stress in the NW array. The effective magnetic anisotropic field (H_A) of an NW array is given by:

$$H_A = 2\pi M_s - 6.3\pi M_s \frac{L\, r^2}{d^3} + M_{mc} + M_{me} \tag{4.5}$$

With small contributions of the M_{mc} and the M_{me} and a much higher shape anisotropy than dipolar interaction, the SQ of the magnetic hysteresis loop will be close to 1. As the dipolar interaction increases, becoming much higher than the shape anisotropy, the magnetic hysteresis loop tends to tilt, leading to a SQ decrease and a M_s increase in the saturation field. The parallel and perpendicular magnetizations curves are superimposed for a constant diameter and inter-spacing at a critical NW length. However, it is very difficult to predict a trend for the coercivity versus NW length because it depends on many factors such as aspect ratio and NW microstructure. [67, 78]

Analyzing the M(H) loops corresponding to the external field applied parallel ($H_{\parallel}$) to the NWs, from NWs with 7 μm to NWs with 27 μm there is a decrease in the H_c (530 Oe to 320 Oe), and in the SQ (0.12 to 0.07) (figure 4.8).

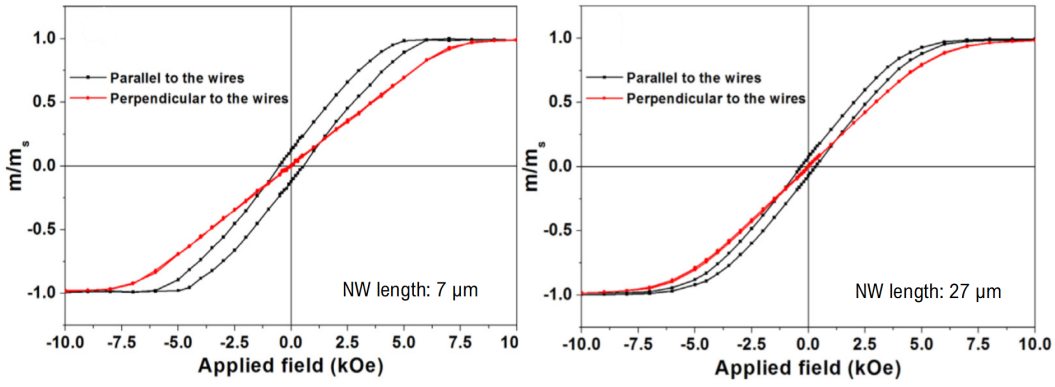


FIGURE 4.8: Magnetic hysteresis curve of equiatomic FeCo NWs with length of (a) 7 μm and (b) 27 μm, with $H_{\parallel}$ and $H_{\perp}$ [67].

Besides the demonstration that the H_A and SQ can be modified by changing the length of the NWs (figure 4.8), Mansouri et al. also demonstrated that the H_c can be altered by annealing (figure 4.9). H_c increase can be attributed to different factors such as (1) the thermal mismatch between the CTE of alumina and FeCo can improve the shape anisotropy;

(2) M_{me} increase due to the very hard wall of alumina; and (3) M_{mc} increase caused by strain induced by the expansion of the crystal lattice. [67]

Figure 4.9 represents the evolution of the magnetic hysteresis loops, with $H_{||}$, for FeCo NWs with length of 20 μm. There is an increase in the H_c for NWs annealed for 20 h at 300 ºC. The coercivity passes from 337 Oe to 627 Oe with annealing.

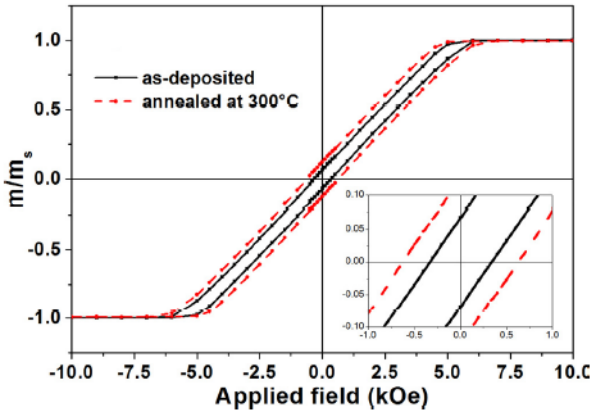


FIGURE 4.9: Magnetic hysteresis curve, with $H_{||}$, of equiatomic FeCo NWs, with length of 20 μm before and after annealing at 300 ºC for 20 h [67].

$Fe_{48}Co_{52}$ NWs with different D_{int} and diameters were annealed at temperatures between 390 and 590 ºC with an $H_{||}$ of 3 kOe for 30 min. These NWs were synthesized by AC electrodeposition into NATs using an electrolyte that consisted in 0.125 mol/L $CoSO_4 \cdot 7\,H_2O$, 0.095 mol/L $FeSO_4 \cdot 7\,H_2O$, 1 g/L $C_6H_8O_6$, and 0.6 mol/L H_3BO_3 with a pH value of 4. XDR analysis revealed a bcc phase structure with a (110) preferred orientation. The influence of annealing temperature with an $H_{||}$ in H_c and SQ in NWs with D_{int} of 50 nm and diameters between 22 and 46 nm, and lengths of 2 μm was also studied. H_c and SQ present the same behaviour (figure 4.10 a) and b)) for both annealing temperatures. $Fe_{48}Co_{52}$ NWs with diameter of 22 nm, D_{int} between 30 and 60 nm, and lengths of 2 μm were also annealed at temperatures between 390 and 590 ºC with an $H_{||}$ of 3 kOe for 30 min. H_c and SQ present the same behaviour (figure 4.10 c) and d)) for both annealing temperatures. [79]

With this study, it was concluded that applying a 3 kOe magnetic field along the NWs while annealing could not significantly enhance the magnetic properties of these NWs. The main reason for this happening is attributed to the magnetostatic interaction between the NWs, because it increases with wire diameter and decreases with D_{int}. It is also suggested to apply a higher magnetic field during annealing to improve these properties. [79]

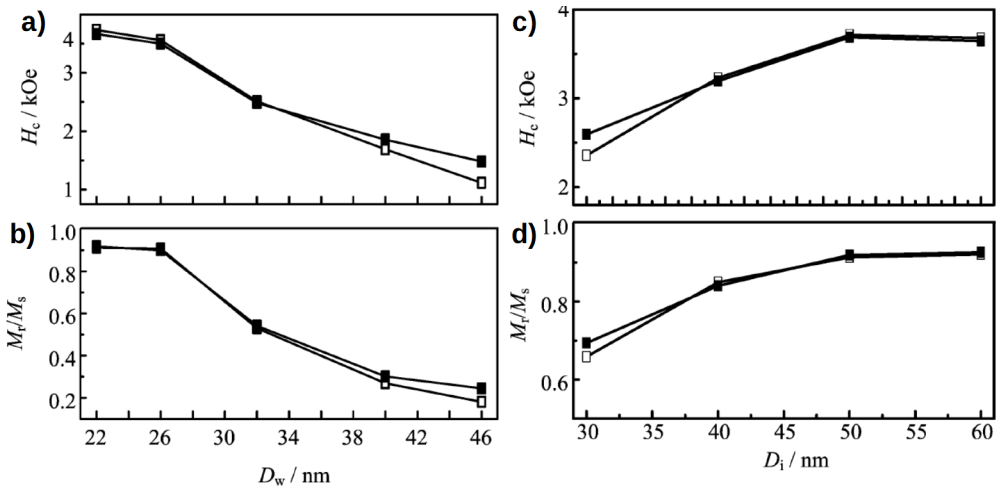


FIGURE 4.10: (a) H_c and (b) SQ for NWs with D_{int} of 50 nm in function of NW diameter; (c) H_c and (d) SQ for NWs with diameters of 22 nm in function of D_{int}; where hollow squares represent NWs as-deposited and solid squares represent NWs annealed at 550 °C [79].

$Fe_{100-x}Co_x$ ($0 \leq x \leq 100$) NWs with L = 3 and 4 μ and diameters 40 and 20 nm, respectively were fabricated through electrodeposition in NATs at room temperature. The electrolyte consisted in $CoSO_4 \cdot 7\,H_2O$ (0.02-0.16 M), $FeSO_4 \cdot 7\,H_2O$ (0.02-0.16 M), $C_6H_8O_6$ (0.06 M), and H_3BO_3 (0.16 M) with a pH value of 3. XRD revealed that NWs with 40 nm shown cubic symmetry for the whole range of studied compositions (figure 4.11). Starting with a body-centred cubic (bcc) for pure Fe and passing to a face-centred cubic (fcc) as the Co atomic content increases. For NWs diameters of 20 nm a similar compositional evolution was obtained, but pure Co NWs presented a hexagonal closed packed (hcp) structure. [66] Still, both series of NWs had a phase transition at $x \approx 80$ which is in good agreement with the phase diagram [67] of bulk alloy shown before (figure 4.1) and also with the XRD patterns obtained for bulk alloys (figure 4.4).

The magnetic properties $\mu_0 H_c$ and SQ studied (figure 4.12) for $H_{\|}$ shown similar behaviour for both NW diameters. Both these properties, $\mu_0 H_c$ (figure 4.12 a)) and SQ figure 4.12 b)), present a minimum for low Co content and continuously increase with Co content. The largest $\mu_0 H_c$ obtained is above 0.27 T and the largest SQ obtained is above 90 %. Also, the NWs with 20 nm of diameter, generally, present higher values of $\mu_0 H_c$ and SQ. [66]

Besides the variation of the $\mu_0 H_c$ with the Co content, the influence of temperature (figure 4.12 c) and d)) was also studied. Results revealed that the $\mu_0 H_c$ for both NWs diameters decreases with increasing temperature. However, for Co NWs, the opposite

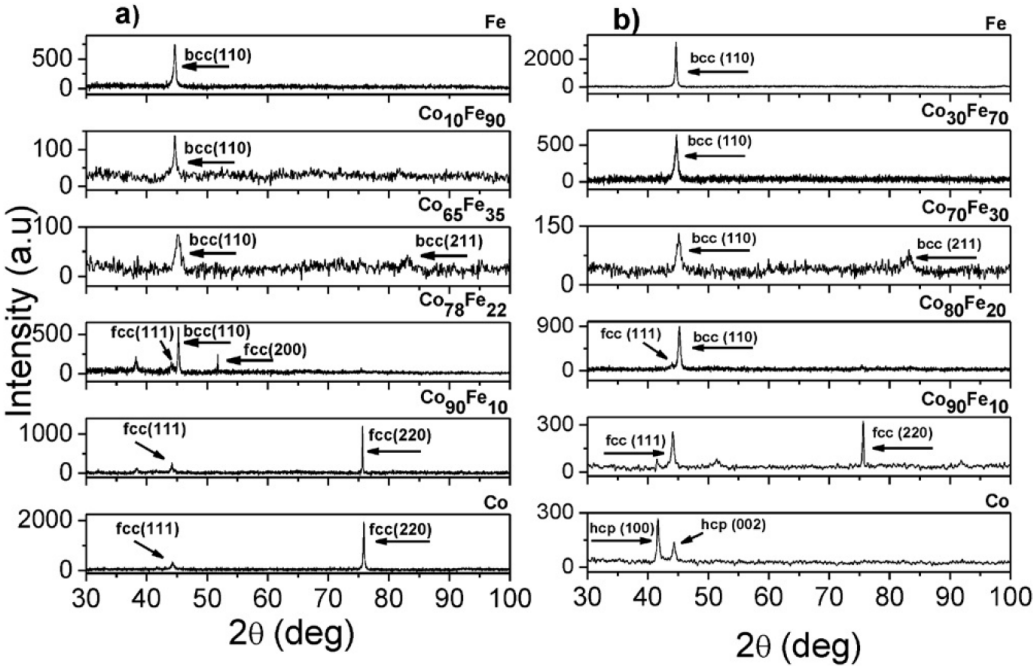


FIGURE 4.11: XDR patterns of $Fe_{100-x}Co_x$ NWs with diameters of a) 40 nm and b) 20 nm [66].

is observed. The $\mu_0 H_c$ increases with increasing temperature. For the NWs with 20 nm diameter, the $\mu_0 H_c$ varies more with temperature. [66]

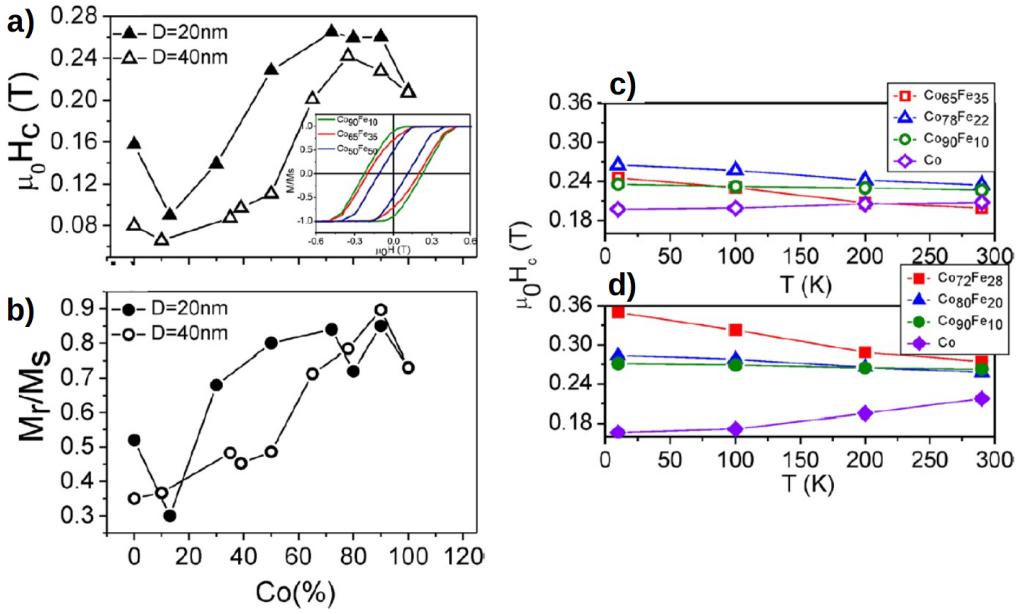


FIGURE 4.12: (a) Evolution of $\mu_0 H_c$ and (b) SQ with atomic percentage of Co at room temperature for NWs with diameters of 40 nm and 20 nm. Temperature dependence of $\mu_0 H_c$ for NWs with diameters of (c) 40 nm and (d) 20 nm. [66]

Throughout the works presented, one can observe that the method of choice to fabricate FeCo NWs is by using NAMs due to their versatility. The solutions used to synthesize this type of NWs are also variations of the same components. The molar masses of each one can be changed to obtain the desired stoichiometries of the alloy. Compared with the bulk alloys, the XRD patterns are very similar. However, NWs patterns mostly present lesser peaks corresponding to the alloy, sometimes even just one peak. As for the magnetic properties, H_c and SQ, these are highly customizable by changing the diameter length of the NWs. Despite the various results present in the literature, there is a lack of optimized parameters such as electrodeposition potential to allow constant growth of NWs. Also, as far as our knowledge goes, there are no models to predict NWs lengths through parameters such as charge transferred. Besides, in spite of all the studies in FeCo NWs, none presented results about the TE.

Chapter 5

Experimental and characterization techniques

In this chapter, a summary of all the experimental techniques used in this work is presented. We start by listing the materials, then synthesis methods, and finally a description of the characterization techniques.

5.1 Materials

In this section, a list of several materials and reagents used in this work is presented.

Cleaning:

C_2H_6O, Ethanol (70 %)

CH_3COCH_3, Acetone

Electropolishing:

$HClO_4$, Percloric acid (Sigma-Aldrich, 70.0 - 72.0 %)

C_2H_6OH, Ethanol (96 %)

Metal Foil:

High purity Aluminium foil (99.999 %), 0.25 mm thick from Goodfellow

Anodization electrolyte:

$(COOH)_2$, Oxalic acid (Acros Organic, 98 %)

Chemical etching for alumina removal:

CrO_3, Cromic acid (Acros Organic, 99.5 %)

H_3PO_4, Phosphoric acid (Fisher Chemical, 85 %)

Aluminium removal:

$CuCl_2$, Cooper(II) Chloride (Acros Organic, 99 %)

HCl, Hydrochloric acid (Chem-Lab, 37 % a.r.)

Chemical etching for alumina removal and pore widening:

H_3PO_4, Phosphoric acid (Fisher Chemical, 85 %)

Electrodeposition:

$CoSO_4 \cdot 7\,H_2O$, Cobalt (II) sulfate heptahydrate (Fisher Chemical, 99+ %)

$FeSO_4 \cdot 7\,H_2O$, Iron (II) sulfate heptahydrate (Acros Organic, 99.5 %)

BH_3O_3, Boric acid (Ficher Chemical, $\geq$ 99.5 %)

$C_6H_8O_6$, L-ascorbic acid (Sigma Aldrich, 99.7 % min)

Orosene (falta completar)

Bulk materials:

Fe, Iron pieces, irregularly shaped, 3.2-6.4mm, 99.99 %

Co, Cobalt Pieces (Alpha Aesar, 99.99 %)

5.2 Methods

Herewith is presented all the methods and steps to fabricate FeCo NWs as well as bulk FeCo alloys. All the samples were prepared in IFIMUP (Universidade do Porto), the NWs more specifically in the Bottom-up Nanofabrication Laboratory ("Alumina Lab").

5.2.1 Substrate Cleaning

The Al metal foil was cut into 1.5 x 1.5 cm^2 pieces. The pieces were cleaned with acetone and ethanol 70 % and 96 % in an ultrasonic bath for 3 min for each step before the anodization.

5.2.2 Electropolishing

Electropolishing consists of the electrolytic removal of metal in an ionic solution through an electric potential. This method is used to remove thin layers of contaminated material on the surface of the metal and for micro-polishing, where a smooth surface is obtained. The electropolishing set-up, represented in the figure 5.1, has an anode that is the metal substrate and a cathode that is a Pt mesh. The electrodes distanced from 2.5 cm are immersive in the ionic electrolyte, which is mechanically stirred and establishes an electric circuit when a DC voltage is applied. The electric field lines concentrate more on the top of irregular topographic points than the valleys regions. Consequently, the higher points of the metal surface will corrode faster.

The electrolyte used in this work consisted of 75 % ethanol, 96 % and 25 % perchloric acid and was stirred at 300 rpm. Each piece of Al foil is electropolished for 2 min at 20 V in a bath of ice to keep the temperature at 10 ºC.

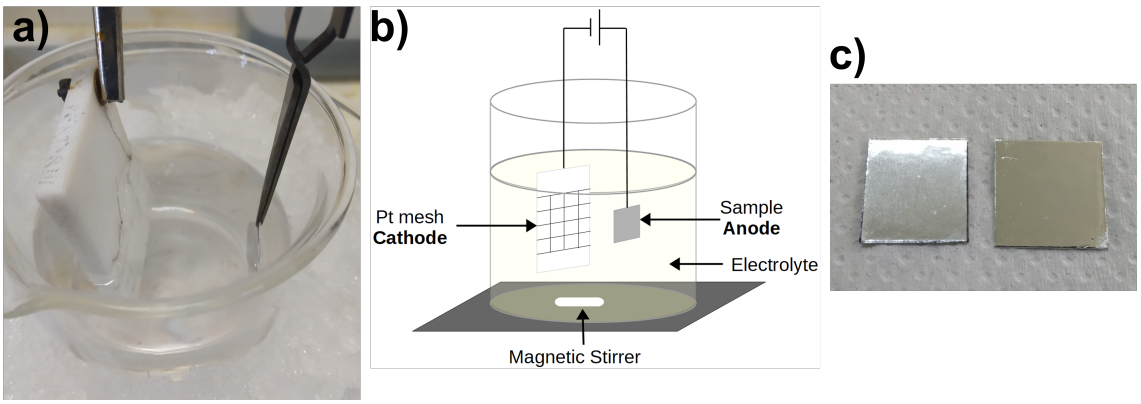


FIGURE 5.1: (a) Experimental set-up and (b) schematic of the set-up for the electropolishing. (c) Al foil before and after the electropolishing.

5.2.3 Electrochemical Anodization

The anodization was performed in a cell consisting of a Teflon container, where the Al foils (working electrode) are placed in its bottom in contact with a Cu plate, used as the anode, and a Pt mesh (counter electrode) inserted at the top that acts as the cathode (see

figure 5.2). The anodization area for each piece of Al foil is 1 cm^2. The electrolyte was agitated through the anodization using an electric fan.

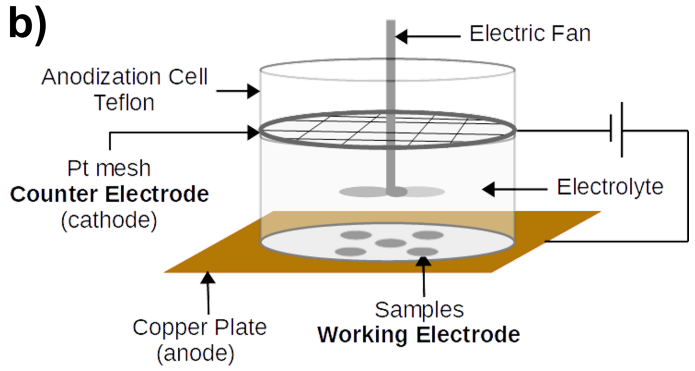


FIGURE 5.2: (a) Experimental set-up and (b) schematic of the set-up for the anodization.

The mild anodization using a two-step anodization process was performed in 0.3 M oxalic acid at 40 V and 5 ºC. The first anodization was carried out for 24 h. The alumina was removed in a aqueous solution of 0.2 M H_3PO_4 and 0.4 M H_2CrO_4 for 12 h at 40 ºC in a ultrasound bath. The second anodization was performed for 60 h, in the same conditions as the first anodization.

For the hard anodization, the electrolyte was also 0.3 M oxalic acid at 5 ºC. This type of anodization was done in three steps, first a pre-anodization of 5 min at 40 V and after a ramp of 0.6 V/s until 140 V, then hard anodization of 60 min at 140 V, and finally an after-anodization of 1 min at 40 V.

The anodization current density curves were recorded and monitored using a Keithley 2004 Sourcemeter controlled by a home-developed LabView application. The Sourcemeter operates in potentiostatic mode, with a range from 0 to 210 V, and in a galvanostatic mode, with a range from 0 to 110 mA. The application allows the automatic control of the anodization experiments within user-defined conditions such as anodization time, applied voltage, etc.

5.2.4 Electrodeposition

For the DC electrodeposition inside the PAA templates, the leftover Al foil was removed with a aqueous solution of 0.2 M $CuCl_2$ and 4.1 M HCl at room temperature, as shown in figure 5.3 a). The alumina barrier at the bottom of the pores was also chemical-etched in 0.5 H_3PO_4 at 30 ºC for membranes fabricated through mild anodization (see figure 4.5 b)), and at 50 ºC for membranes fabricated through hard anodization. When the membrane

drowns, it means that the pores are open. This process enlarges the pores slightly and can also be used to widen the pores at a rate of 2 nm/min. Then, a layer of Au was sputtered on the membrane on the side where the pores were opened to serve as the working electrode, see the final result in figure 4.5 c). Before the electrodeposition of the NWs, it was electrodeposited Orosene to obtain a layer of Au NWs. This guarantees that the bottom of the pores, where it first deposited a thin film of gold by sputtering, is a uniform layer of Au that allows the NWs to grow uniformly. For NAMs fabricated through mild anodization, the Au was electrodeposited for 6 min. For the ones fabricated through hard anodization, the Au electrodeposition was 15 min, both using a V_{dep} of -1.0 V.

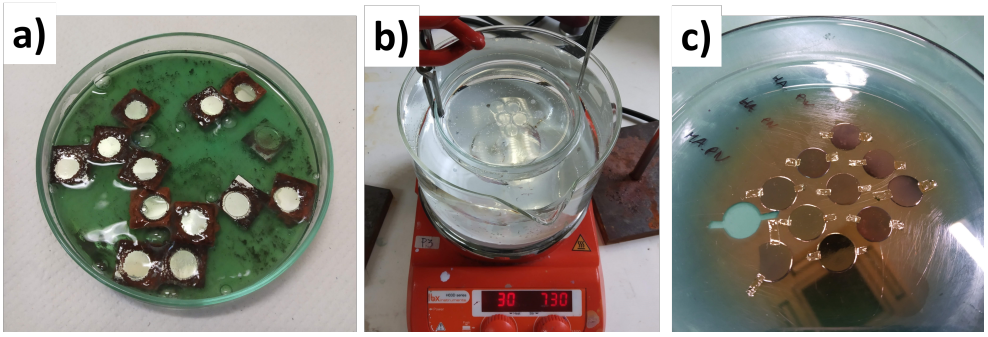


FIGURE 5.3: (a) Al foil removal, (b) alumina barrier removal, and c) NAM sputtered with Au.

The electrodeposition set-up includes the substrate used or the NAM as the working electrode, a Pt mesh as the counter electrode and an Ag/AgCl (in 4 M KCl) as the reference electrode as represented in the figure 5.4. The electrodeposition was performed at room temperature $\sim$ 19 ºC.

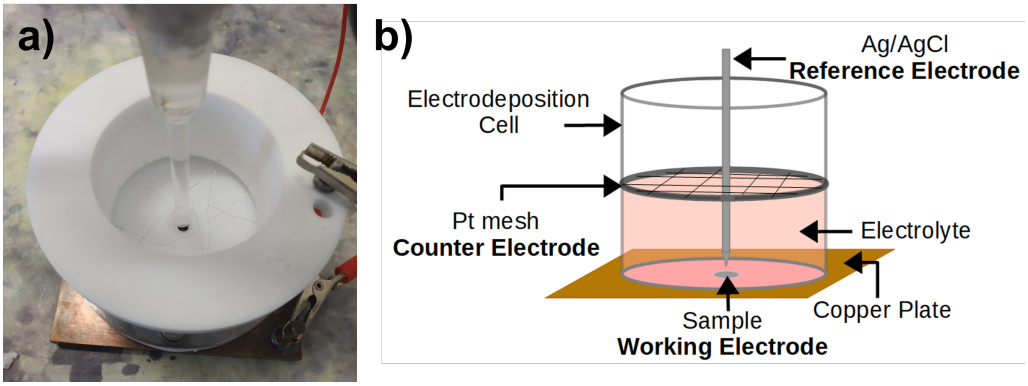


FIGURE 5.4: (a) Experimental set-up and (b) schematic of the set-up for the electrodeposition.

Initial electrodepositions current curves were recorded and monitored using a Keithley 2004 Sourcemeter, the same as for the anodization, which is controlled by a home-developed LabView application. Then the electrodepositions were controlled by Potenciostato Autolab (PGSTAT204).

5.2.5 Sputtering

Sputtering is a physical vapor deposition technique used to fabricate thin films. This method is versatile, simple and inexpensive, and produces thin films with good uniformity, density and adhesion.

This technique removes atoms from the surface of a material, called target, through the bombarding by energetic particles, normally ions, of plasma or gas. The atoms removed are accelerated and deposited onto the substrate. The process happens in a chamber in a vacuum, where gas is inserted. When a voltage is applied between the cathode, target, and the anode, substrate, the gas is ionized. In figure 5.5 one can observe the experimental set-up as well as a graphic representation. In this work, the sputtering was used to deposit a thin film of Au in NAMs. So the Au was the target, and the NAMs were the substrate. The gas used was argon, which is one of the most commons.

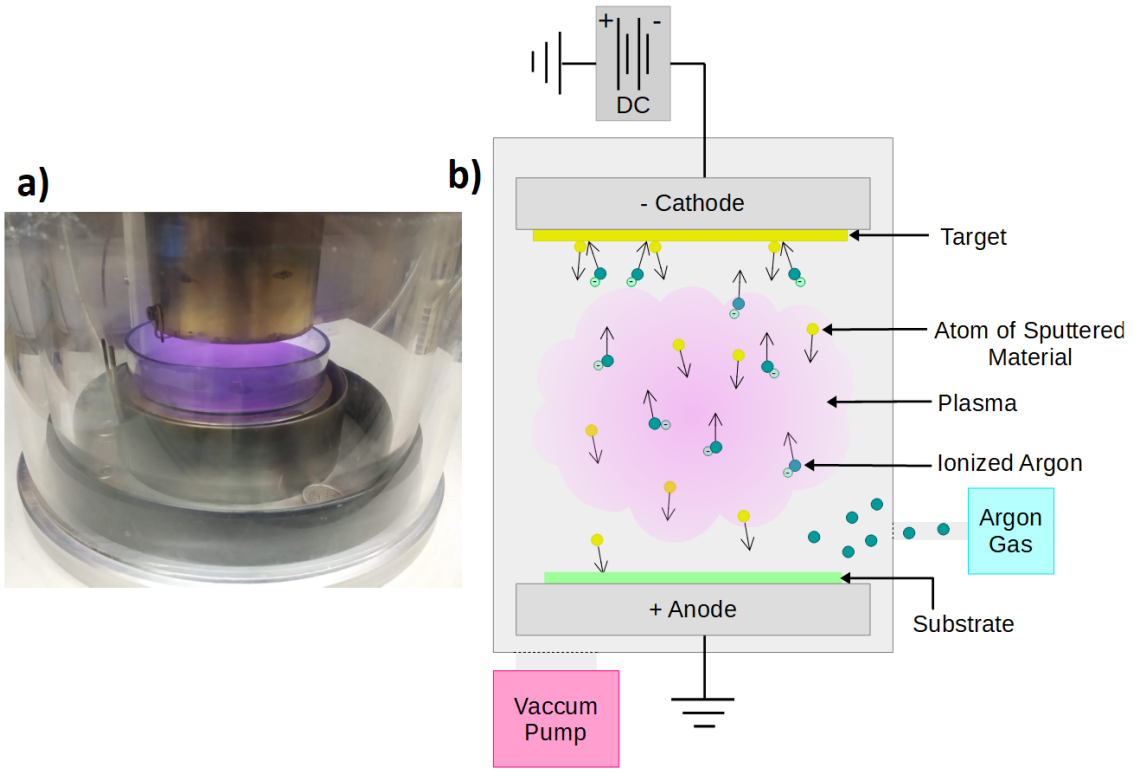


FIGURE 5.5: (a) Experimental set-up and (b) schematic of the set-up for the deposition of the thin film of gold by sputtering.

5.2.6 Arc-melting furnace

The preparation of bulk samples in this work was done by arc melting. This method applies a high power between a copper electrode with a tungsten tip and a copper electrode with crucibles in an Ar atmosphere. A schematic representation of the set-up is presented in figure 5.6. The copper electrode with the tungsten tip is controlled by the user. By approximating the tungsten tip to the crucibles, an electric discharge occurs, and a visible electric arc is formed. When placed on top of the bulk pure elements, this arc causes their melting, resulting in homogeneous alloys. In the chamber is also present a titanium getter that, when partially melted, helps to absorb any remaining oxygen and other lighter elements in the chamber. The samples were prepared in the arc-melting furnace from IFIMUP (Universidade do Porto).

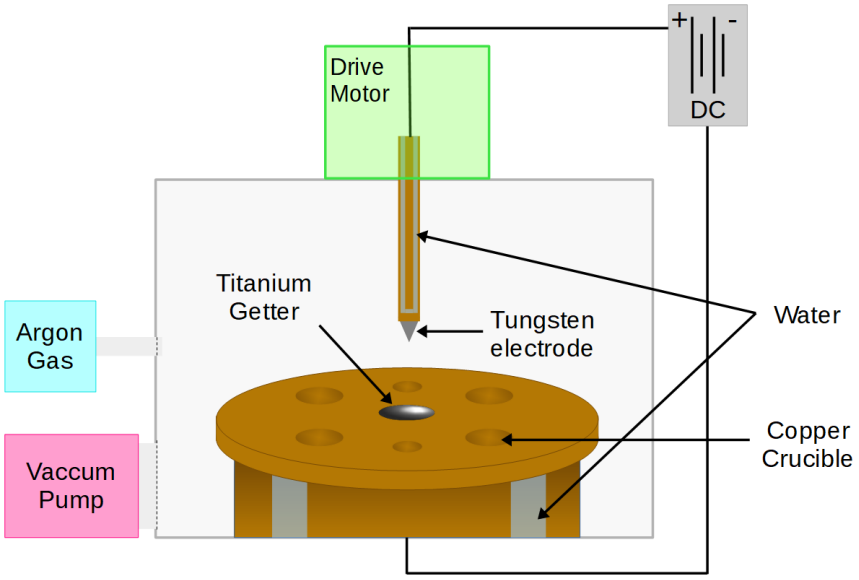


FIGURE 5.6: Graphic representation of the set-up for the preparation of alloys using the arc melting furnace.

5.3 Characterization Thecnique

5.3.1 Electron Microscopy

The electron microscopy technique allows obtaining images of materials by using an accelerated electron beam as an illumination source. The wavelength of the electrons in this type of microscopy is usually less than 0.1 nm, which is several times smaller than the wavelength of photons in optical microscopes. Thus, electron microscopes possess higher

revolving power and field depth. Its system is based on controlling the electron beam kinetic energy, its settings, and its focusing through the usage of electrostatic and magnetic lenses. There are several methods of electron microscopy such as SEM, STEM, EDS and TEM.

5.3.1.1 Scanning Electron Microscopy (SEM)

The morphology of samples was obtained by Scanning Electron Microscopy (SEM), where the image resolution ranges from a few millimeters down to 5 nm. In this method, high-energy electrons irradiate the sample. In turn, the sample surface emits both electrons and photons. A set of magnetic lenses is used to move the focused electron beam across the sample. Then the intensity of the electrons and photons emitted are convoluted to form the SEM image. Different signals can be used to form the images, being the most common secondary electrons, and the backscattered electrons and the X-rays.

The secondary electrons are electrons from the sample obtained from inelastic collisions caused by the incident electron beam. Their energy is less than 50 eV, and their signal is mostly localized at the point of impact of the primary electron beam. The backscattered electrons are electrons from the primary electron beam reflected from the sample by elastic scattering. The intensity of this electrons signal is strongly related to the atomic number of the illuminated spot in the sample. So a 2D phase analysis can be performed.

SEM images were obtained with the equipment from CEMUP (Porto) using a FEI Quanta 400FEG ESEM / EDAX Genesis X4M. SEM analysis of the bottom of NAM samples were performed by using an FEI Inspect F50 microscope (FEI Europe, Madrid, Spain).

5.3.1.2 Energy-dispersive Spectroscopy (EDS)

The Energy-Dispersive Spectroscopy (EDS) can be performed in the features observed in SEM to obtain the corresponding elemental composition through the X-rays analysis. This method uses the primary electron beam to eject an electron in an inner shell, creating a hole. Then an electron from an outer, higher-energy shell fills the hole, releasing an X-ray due to the energy difference. Since each element possesses characteristic X-ray wavelengths associated, the elemental composition of the specimen to be measured.

EDS was performed with the equipment from CEMUP (Porto) using a FEI Quanta 400FEG ESEM / EDAX Genesis X4M.

5.3.2 X-Ray Diffraction (XRD)

The X-ray Diffraction (XRD) technique is one of the most used to study the crystallography of both poly and single crystalline samples. This technique consists of shining an X-ray beam in a sample, where the X-rays interact with the atoms resulting in the scattering of the radiation. The X-ray wavelength is between 0.1 and 10 nm, which is in the same order as the lattice parameters of solids. Since the atoms in a crystal are organized in sets of planes, uniformly spaced, it causes the waves of the incident X-ray beam to interfere constructive and destructive, forming a diffraction pattern. The X-ray beam is then diffracted with specific angles related to the spaces between the atomic planes characteristic of the crystalline structure. The maximum intensities in the diffraction pattern are univocally related to the reciprocal lattice vectors of the crystal. These are the Bragg reflections, and a set of Miller indexes (hkl) can be assigned to each one of them. Bragg's law gives the relationship between the X-ray wavelength (λ) of the incident wave, distance between the planes with the miller indexes (hkl) (d_{hkl}) and diffraction angle (2θ) formed by the propagating vector of the incident wave with the scattered:

$$n\lambda = 2d_{hkl}sin\theta \tag{5.1}$$

Throughout this work, Bragg-Brentano geometry was used in the configuration θ-2θ, in the 2θ range from 10 to 90 at a speed of 7.5 deg/min and at room temperature. The radiation used was Cu-$K_{\alpha 1}$ and Cu-$K_{\alpha 2}$ with wavelengths of $\lambda_1 = 1.540598\ \mathring{A}$ and $\lambda_2 = 1.544418\ \mathring{A}$.

The XRD measurements at room temperature were performed with a Philips X-Pert diffractometer at IFIMUP (Universidade do Porto). The XRD measurements to determine the thermal expansion were performed with Anton Paar htk1200 furnace on a Bruker d8 series 2 diffractometer with a Lynxeye detector run under a slow flow of 99.998 % N_2 gas, around one to two bubbled per second, at Durham University. The analysis of the diffractograms was done recurring to FullProf Studio package software. [80]

5.3.3 High - Resolution Synchrotron X-Ray Radiation Diffraction Technique

The Synchroton X-ray radiation diffraction (HRSXRD) technique is similar to the XRD. However, the X-rays used here are produced from accelerating charged particles along with a proper curvilinear particle accelerator, where accelerated charge emits electromagnetic radiation. In comparison, the X-rays used in XRD are produced when the collision

of electrons with a Cu metallic target causes abrupt transitions in the Cu atoms that emit electromagnetic radiation. The HRSXRD technique allows faster measurements using typically transmission geometry, where the transmitted and scattered beam are detected and higher resolution.

5.3.4 Superconducting Quantum Interference Device (SQUID)

The magnetic properties of the bulk samples fabricated were studied with a Superconducting Quantum Interference Device (SQUID) magnetometer. It is an integrated device that contains a superconducting magnetic coil immersed in a helium bath and a corresponding control system. With this system, one can perform magnetization measurements in the temperature range of 5 to 380 K. One can conduct experiments of isothermal M(H) where we can obtain the saturation magnetization (M_s) and the coercive field (H_c), and M(H) to determine the critical temperature. The M(T) curves are obtained in heating. If the sample is cooled without any applied field, the M(H) curve is denominated a zero-field-cooled (ZFC) magnetization, otherwise called a field-cooled (FC) magnetization.

The magnetic properties of the bulk samples were studied with a SQUID magnetometer at IFIMUP (Universidade do Porto).

5.3.5 Vibrating Sample Magnetometer (VSM)

The magnetic properties of the nanowires fabricated were measured using the vibrating sample magnetometer (VSM). It is a scientific instrument that measures magnetic properties based on Faraday's Law of Induction. To effectuate the measurement, one applies a constant field to the sample aligning its magnetization with the external field. Then the sample vibrates, and the magnetic dipole moment creates a magnetic field that changes as a function of time. The alternating magnetic field induces an electric field in the VSM coils, and a hysteresis loop is recorded.

The magnetic properties of the NWs samples were studied with a VSM (LakeShore Controller, Model 7304) (Madrid). All measurements have been performed at room temperature, with the magnetic field applied parallel and perpendicular to the NWs' long axis

Chapter 6

Results and Discussion

Aiming to customize the thermal expansion in FeCo NWs alloys, we started by fabricate and characterizing morphological, structural and magnetic properties of FeCo bulk alloys. Then, to synthesize FeCo NWs, parameters such as stoichiometry and thickness needed to be first studied, so the solutions were first electrodeposited unto copper tape substrates and later unto NAMs. Due to several difficulties in the fabrication of NWs with different stoichiometries, an intensive electrodeposition optimization study was performed. Finally, samples of FeCo NWs alloys had their thermal expansion calculated.

Additionally, a simple study in FeCo oxide as a co-catalyst for photocatalytic water splitting for solar H_2 generation was carried out. Also, a study of the thermal expansion in microparticles of $La(Fe, Si)_{13}$ was conducted.

6.1 Bulk FeCo alloys

Three different bulk FeCo alloys were fabricated with the following stoichiometries: $Fe_{10}Co_{90}$, $Fe_{50}Co_{50}$ and $Fe_{10}Co_{90}$ by arc-melting technique. Individual Fe and Co compounds were carefully measured in weight to form alloys with the desired stoichiometries. The compounds were placed in the copper crucibles inside the arc-melting furnace. The chamber was purged with Ar gas three times, and between each purge, the chamber pressure was greatly reduced to a vacuum of approximately $P \sim 10^{-4}$ mbar by the action of the rotary (primary) and diffusion (secondary) pumps. After reaching the last vacuum, the chamber was filled with Ar gas until reaching a pressure of $P \sim 800$ mbar. Afterward, an electric arc was formed that led to the melting of the compounds. The melting was executed two times, cooling down the samples in between melts. Because the bottom of the samples

is in contact with a refrigerator base, the samples are subjected to a temperature gradient that can cause the stoichiometry not to be homogeneous through all the samples. So, the chamber was then open to turn the samples around and repeat the process, ensuring that the samples were all homogeneous.

After the three bulk FeCo alloys fabrication, the samples were characterized structurally and magnetically using XRD and SQUID, respectively. Additionally, the individual Fe and Co reagents were also analyzed.

6.1.1 Structural Characterization

To characterize the bulk samples by XDR, they were prepared by cutting them into smaller pieces and then polished to obtain a flat surface. The XRD patterns, for each sample ($Fe_{10}Co_{90}$, $Fe_{50}Co_{50}$, $Fe_{10}Co_{90}$, Fe and Co), are presented in the figure 6.1 alongside with the Miller indices correspondent to each peak.

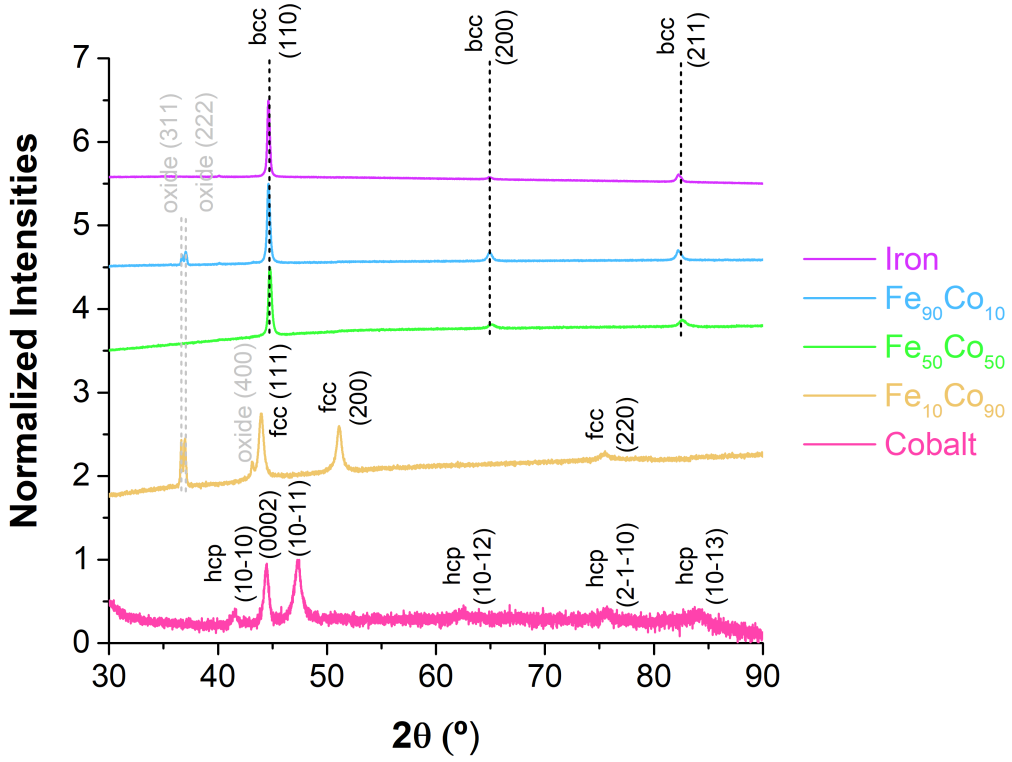


FIGURE 6.1: XRD patterns of Co, $Fe_{10}Co_{90}$, $Fe_{50}Co_{50}$ and $Fe_{10}Co_{90}$ and Fe bulk alloys with the respective miller indexes.

XRD patterns of the bulk alloys revealed that the compositions of Fe, $Fe_{90}Co_{10}$ and $Fe_{50}Co_{50}$ possess a bcc structure, $Fe_{10}Co_{90}$ has an fcc structure, and Co shows an hcp phase

structure, which is in accordance with the results presented in the literature [75]. All samples revealed their polycrystalline character. Additionally, the diffractograms of the alloys $Fe_{10}Co_{90}$ and $Fe_{90}Co_{10}$ indicate that these samples suffered oxidation. The peaks corresponding to the oxide could be attributed to magnetite, Fe_3O_4, or maghemite,γ-Fe_2O_3. However, since these two oxides have the same fcc structure is not possible to differentiate them by XRD [12, 81].

Each peak was fitted individually using the function Pseudo-Voigt in the software OriginPro to obtain peak full width at half maximum (FWHM) and peak center. These parameters were used to obtain the crystallite size and lattice parameter of the alloys. The Scherrer equation [82] was used to calculate the crystallite size, which is given by:

$$L = \frac{0.9\lambda}{\beta cos\theta} \tag{6.1}$$

where β is the FWHM in radians, and θ corresponds to the value of peak center in the 2θ axis, and λ is the X-ray wavelength in nanometer (nm).

The calculation of the lattice parameter was done using the following equation:

$$a = \frac{\lambda\sqrt{h^2 + k^2 + l^2}}{2sin\theta} \tag{6.2}$$

which is a derivative from the equation 5.1 presented in the previous chapter 5.

In figure 6.2 is represented the crystallite size (green dots) and the lattice parameter (blue dots) for each Fe_xCo_{1-x} (x = 10, 50, 90, 100) bulk alloy. The lattice parameter for the Co bulk sample is not represented on the graphic because it has an hcp structural phase, having two different lattice parameters. As one can observe, the grain size increases with the Fe content [83]. The lattice parameter however, is somewhat constant for Fe and all the alloys with bcc structural phase, $\sim$ 2.86 $\AA$, increasing for 3.56 $\AA$ for the $Fe_{10}Co_{90}$ alloy, which has a fcc structure [12, 83, 84].

6.1.2 Magnetic Characterization

SQUID magnetometer was used to characterize magnetically the bulk alloys Fe, $Fe_{90}Co_{10}$, $Fe_{50}Co_{50}$ and Co, the alloys $Fe_{10}Co_{90}$ was not measured due to equipment problems. Figure 6.3 a) and b) presents the hysteresis loops (M(H)), magnetization (M) in function of the applied field (H), obtained for Fe, $Fe_{90}Co_{10}$, $Fe_{50}Co_{50}$ and Co at 300 K, and for $Fe_{90}Co_{10}$ and $Fe_{50}Co_{50}$ at 5 K. One can observe that all the bulk alloys are soft ferromagnetic materials, presenting a SQ (M_r/M_s) very close to zero. Accurate values of M_r were not possible

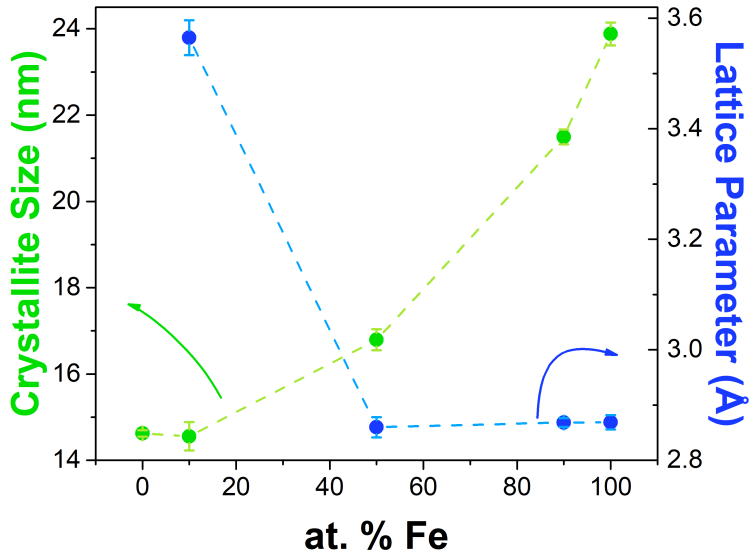


FIGURE 6.2: Crystallite size (green dots) and lattice parameter (blue dots) of the bulk alloys Fe_xCo_{1-x} (x = 0,10,50,90,100).

to calculate due to low-resolution measurements. Only the Co presents a considerable M_r in the value of 9 %..

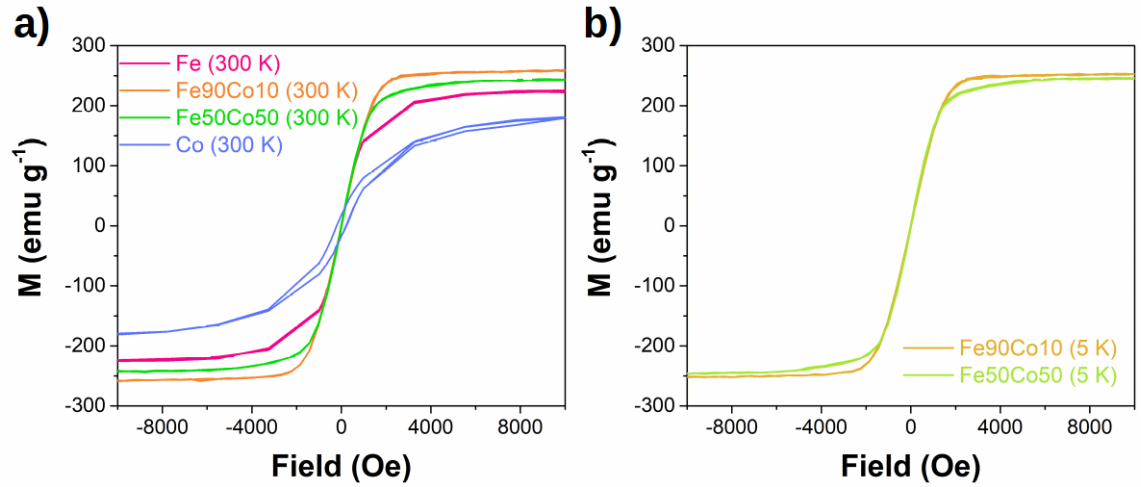


FIGURE 6.3: a) Magnetic hysteresis loops of bulk alloys Fe, $Fe_{90}Co_{10}$, $Fe_{50}Co_{50}$ and Co at 300 k, and b) the magnetic hysteresis loops of $Fe_{90}Co_{10}$, $Fe_{50}Co_{50}$ bulk alloys performed at 300 K and at 5 K.

Figure 6.4 shows the M_s in function of the content of Fe in the alloys. M_s increases with the at. % of Fe until a maximum of $\sim$ 260 emu g^{-1} for the alloy $Fe_{90}Co_{10}$ [10, 11, 83]. However, for 100 at. % of Fe a decrease of M_s is observed. This is related with the fact that the magnetic moments of Fe change with their environment, whereas the same is not observed for Co. Pure Fe atoms present a magnetic moment of 2.2 μ_B, whereas ordered

equiatomic FeCo alloys have a mangnetic moment of $3\mu_B$ [85]. These results also show that the measurements performed at 300 K and then at 5 K do not differ significantly.

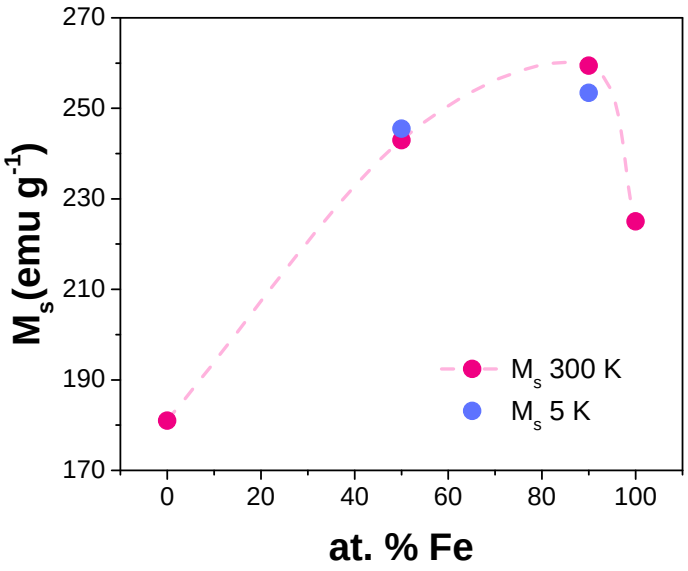


FIGURE 6.4: M_s in function of the content of Fe of the bulk alloys Co, $Fe_{90}Co_{10}$, $Fe_{50}Co_{50}$ and Fe. Pink dots correspond to the measurements at 300 K and blue dots to measurements at 5 K, whereas the dashed line is only a guide obtained through a spline.

6.2 $Fe_{20}Co_{80}$ alloys

This section presents an initial study performed on the deposition of FeCo by the electrodeposition technique. In the first stage, (2D) thin films were deposited on Cu substrate, then (1D) NWs were deposited in NAMs. The electrodeposition solution used was already used in previous experiments in Bottom-up Nanofabrication Laboratory, it will be called the test solution, and consists on 0.036 M $FeSO_4 \cdot 7\,H_2O$, 0.16 M $CoSO_4 \cdot 7\,H_2O$, 0.16 M H_3BO_3 and 0.06 M $C_6H_8O_6$, for a expected a stoichiometry of $Fe_{20}Co_{80}$.

6.2.1 $Fe_{20}Co_{80}$ Thin Films

We started by performing electrodeposition in Cu tape substrates to grow thin films and to be able to evaluate the behavior of the test solution. More specifically, to obtain parameters such as deposition rate and stoichiometry variation. Before the electrodeposition, the Cu tape substrates were cut in squares and cleaned according to the procedure described in chapter 4. The electrodeposition was controlled with the homemade LabVIEW

program, occurring for different electrodeposition potentials (V_{dep}) : -0.7, -1.0, -1.1, -1.2, and -1.8 V (vs. Ag/AgCl).

In figure 6.5 is present the electrodeposition characteristic curves, current density (j) versus time, obtained for each thin film, for the different V_{dep}.

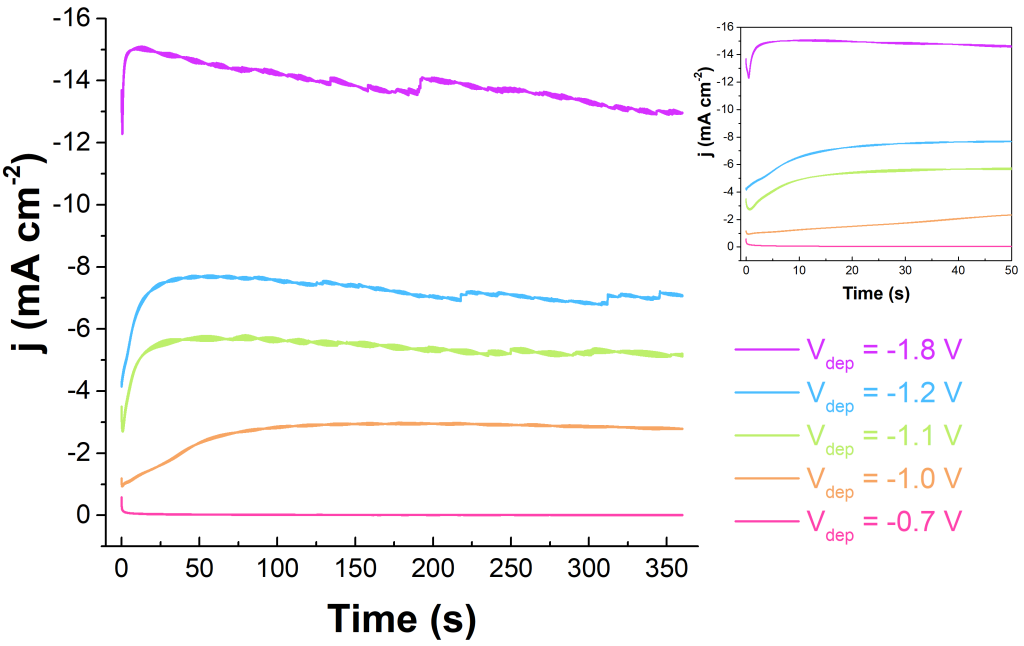


FIGURE 6.5: Electrodeposition curves of the thin films in Cu tape using the test solution obtained with V_{dep} of -0.7, -1.0, -1.1, -1.2, and -1.8 V (vs. Ag/AgCl). The inset is a zoom in the first 50 s of the electrodeposition curves.

One can observe that the overall j increases with the V_{dep} decrease. Where the charge transference is constant in time as observed in figure 6.6 a), indicating a constant growth rate. Several typical stages of thin-film growth can be observed in the electrodeposition curves. A first stage is observed in the first few seconds, where a j increase is observed, corresponding to the formation of the double-layer capacitor. The j reaches its maximum (j_{max}) right after the nucleation and initial growth of the metal film, where with the decrease of V_{dep} the time to achieve j_{max} is fastest (see figure 6.6 b)). Afterward, j decreases slowly due to the diffusion of the species from the electrolyte to the interface electrode/-solution. For example, for the V_{dep} of -1.8 V, the j is continuously decreasing, but for the applied potential of -1.1 V, the j seems to stabilize in time. Thus, for lower V_{dep} are created a bigger depletion zone where the species take a longer time to reach the working electrode. This makes the electrodeposition at lower V_{dep} more diffusion-controlled

than charge controlled. This can be verified by the nucleation time. Lower V_{dep} reach almost instantaneously the j_{max}, much faster than the higher potentials. Because lower V_{dep} implies higher electric fields that increase the nucleation sites on the working electrode, promoting the electrodeposition of the metal (reduction of the metal). This will make the interface electrode/solution depleted of species to electrodeposit. On the other hand, for V_{dep} = -1.0 V, i.e., abrupt nucleation does not occur, so the species are electrodeposited almost at a constant rate. So, the j_{max} increases by making the V_{dep} more negative (figure 6.6 b)) while the corresponding time decreases, indicating an increase in the nucleation rate. Table 6.1 shows the values of j_{max} and their corresponding times (t_{max}), for each V_{dep}.

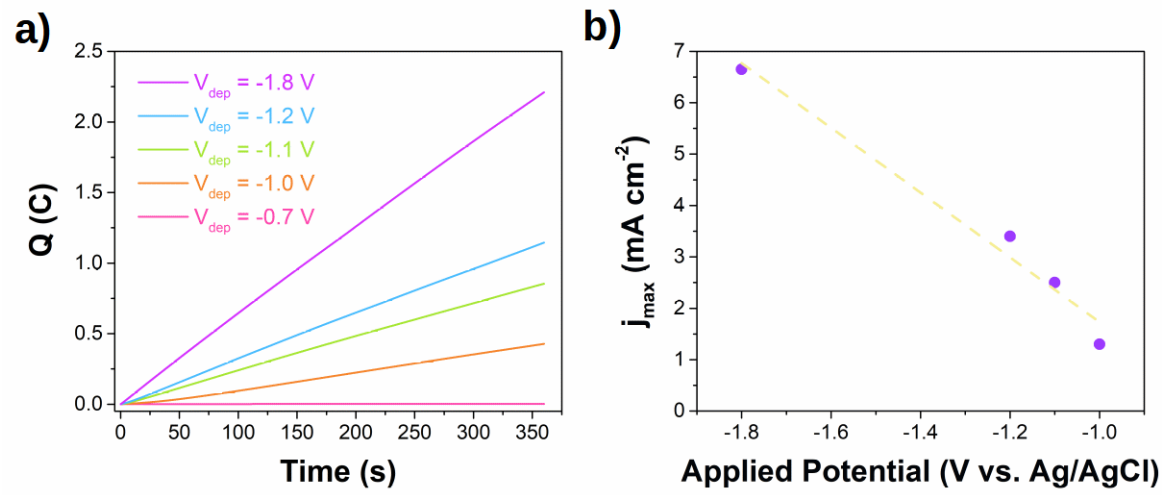


FIGURE 6.6: a) Charge transferred as a function of time and b) current density maximum dependency with V_{dep} of -0.7, -1.0, -1.1, -1.2, and -1.8 V (vs. Ag/AgCl).

Potential Applied (vs. Ag/AgCl) (V)	j_m $(A \cdot cm^{-2})$	t_m (s)
-1.0	1.3	185
-1.1	2.5	68
-1.2	3.4	54
-1.8	6.65	5

TABLE 6.1: j_m and t_m of current density curves electrodeposited at -1.0 V (vs. Ag/AgCl) to -1.8 V (vs. Ag/AgCl).

As for the electrodeposition curve at V_{dep} = -0.7 V, one can observe that it immediately goes to a j of zero. This means that this potential is not adequated to this electrodeposition solution: a lower potential is required for promoting the ionic species, [Fe^{2+}] and [Co^{2+}], separation from their hydrated states, and thus reduce them into their metallic form during electrodeposition.

The nucleation process can be characterized in terms of the type of growth, by comparison with the Scharifker and Hills model using the equations previously presented in chapter 3 [62]. To use this model, we first normalized the j curves to $j/j_m \sim t/t_m$ in order to obtain non-dimensional curves. The parameters j_m and t_m for each curve are presented in the table 6.1 above. The curve corresponding to the applied potential of -0.7 V was not considered because it does not correspond to the typical behavior of an electrodeposition curve due to reasons previously explained.

From the dimensionless curves presented in figure 6.7 one can observe that all the electrodeposition curves are closer to the 3D instantaneous model (compared to the 3D progressive). So, the V_{dep} does not influence the type of nucleation. For $t/t_m > 1$ the experimental curves deviates from the theoretical curve, as expected due to reasons stated in chapter 3.

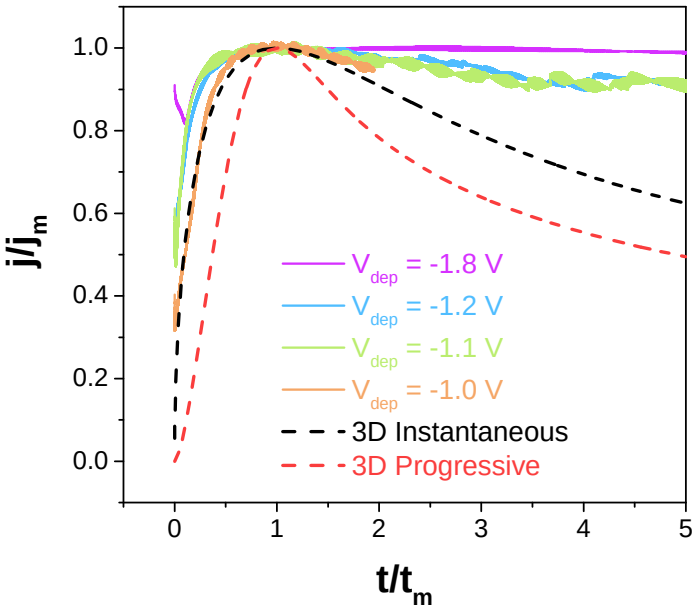


FIGURE 6.7: Electrodeposition curves comparison with the theoretical model of 3D progressive and instantaneous nucleation.

The thin film thickness (L) were estimated by Faraday's Law of Electrolysis [11] adapted with the expression of the volumetric mass density, obtaining the following expression:

$$L = \frac{M}{nF\rho A} \cdot Q \tag{6.3}$$

where M is the molar mass of iron and cobalt which equals 114.75 g mol^{-1}, n is 4 (two electrons for iron and two electrons for cobalt). ρ was calculated having in consideration the theoretical stoichiometry of the solution, $\rho_{Fe_xCo_{1-x}}$ = x· 7.874 g cm^{-3} + (1-x)· 8.9

g cm $^{-3}$, giving ρ = 8.7 g cm^{-3}. The electrodeposition area was 0.442 cm^2, and the total charge transferred (Q) was obtained by integrating current as a time for each sample with different V_{dep}:

$$Q = \int I dt \tag{6.4}$$

The thicknesses obtained were 0.2, 33.1, 66.1, 88.6 and 171.0 μm for the thin films electrodeposited using V_{dep} of -0.7, -1.0, -1.1, -1.2, and -1.8 V, respectively. Figure 6.8 shows the relation between L and V_{dep}, by the Faraday's Law of Electrolysis, revealing a linear dependence. In this case, the linear fit relation gives: $L = (-163 \pm 13) \cdot V_{dep} + (117 \pm 16)$.

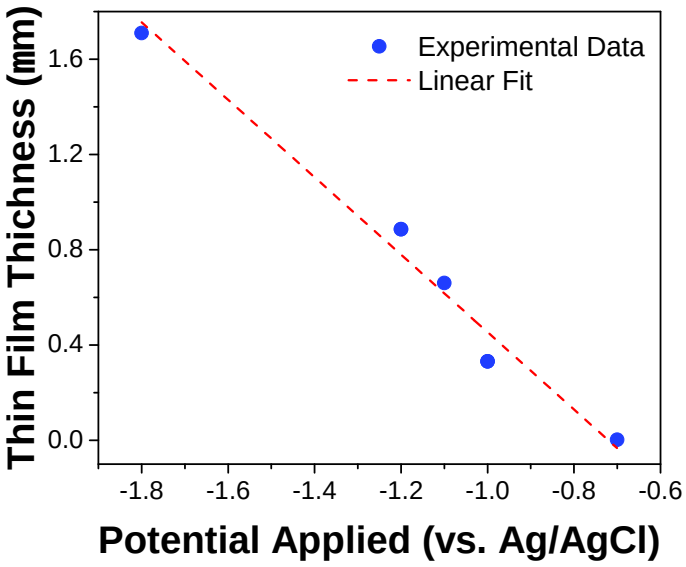


FIGURE 6.8: Blue dots correspond to the thin films thickness obtained using the test solution and applying V_{dep} of -0.7, -1.0, -1.1, -1.2, and -1.8 V (vs. Ag/AgCl), the red dash line is the linear fit.

6.2.1.1 Morphological Characterization

Figure 6.9 a) b) c) and d) shows SEM images of the $Fe_{20}Co_{80}$ thin films electrodeposited, for V_{dep} -1.0, -1.1 and –1.8 V, respectively (with different magnifications). The thin film electrodeposited with V_{dep} of -0.7 V was not observed with SEM. The thin film with V_{dep} = -0.7 V will not be considered in the further analysis since its electrodeposition curve did not correspond to what was expected, and there was no apparent deposition on the Cu substrate. Additionally, the thin film with V_{dep} = -1.2 V was revealed to be contaminated with sulfur.

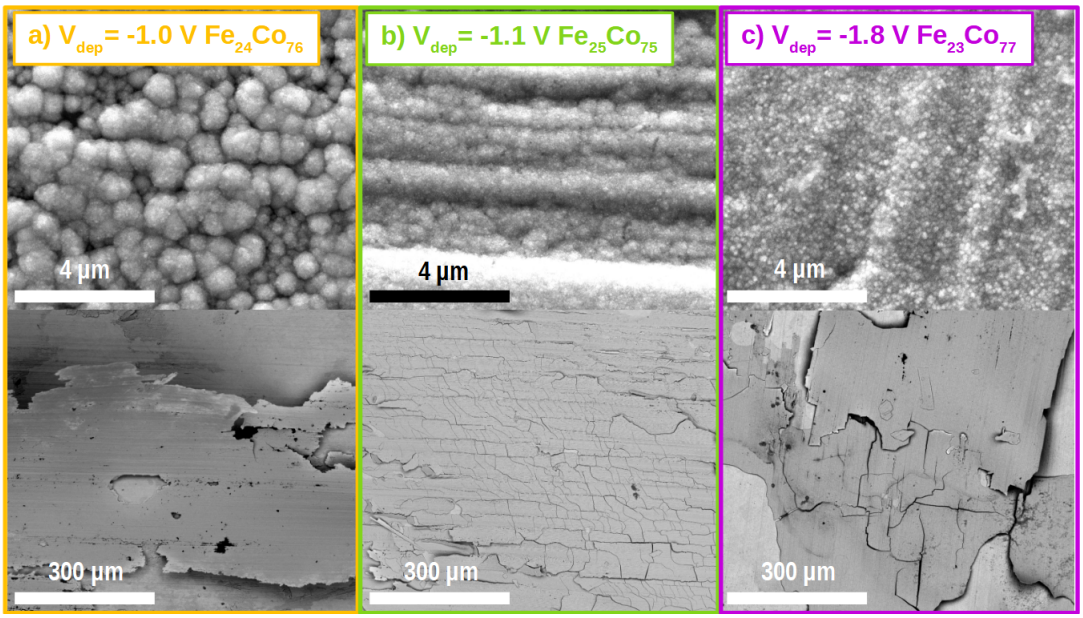


FIGURE 6.9: SEM images from the electrodeposition in copper tape with V_{dep} of a) -1.0, b) -1.1 and c) –1.8 V. Images with lower magnification were obtained with backscattered electrons, and the images with higher magnification were obtained with secondary electrons.

One can observe that for lower V_{dep} (-1.8 V), the film is less granular and more continuous. This fact is correlated with the nucleation time, as previously seen. Lower potentials lead to the fastest nucleation improving the homogeneity of the thin film. EDS analysis revealed stoichiometries of $Fe_{24}Co_{76}$, $Fe_{25}Co_{75}$, $Fe_{24}Co_{75}$ and $Fe_{23}Co_{77}$ for V_{dep} of -1.0, -1.1, -1.2 and –1.8 V, respectively. The stoichiometry presented for the film of V_{dep} of -1.2 V was only considering the content of Fe and Co in the sample, disregarding the content of sulfur. For different V_{dep}, the average stoichiometries were of $Fe_{24}Co_{76}$, leading to the conclusion that V_{dep} does not significantly affect the alloy stoichiometry.

6.2.1.2 Structural Characterization

Figure 6.10 shows the XRD patterns of the thin films electrodeposited with V_{dep} of -1.0, -1.1 and –1.8 V. Only part of the pattern is shown (range from 44.5 ° to 46 °) because the peaks intensity from the Cu substrate are much more intense and pronounced when compared to the FeCo peaks contribution (for full pattern see figure 8.1 of the appendix 8).

All the different films present a single peak $\sim 45°$, corresponding to FeCo bcc structural phase, with a preferential growth in the direction of (110), which is in accordance with the results presented in the literature. The slight deviations in the peak center are related to the centering of the samples in the XRD instrument. By applying the Scherrer

equation (eq. 6.1) to the FeCo XRD peaks, crystallite sizes of 78±4 nm, 53±3 nm and 68±2 nm were obtained for the thin films electrodeposited with V_{dep} of -1.0, -1.1 and –1.8 V, respectively.

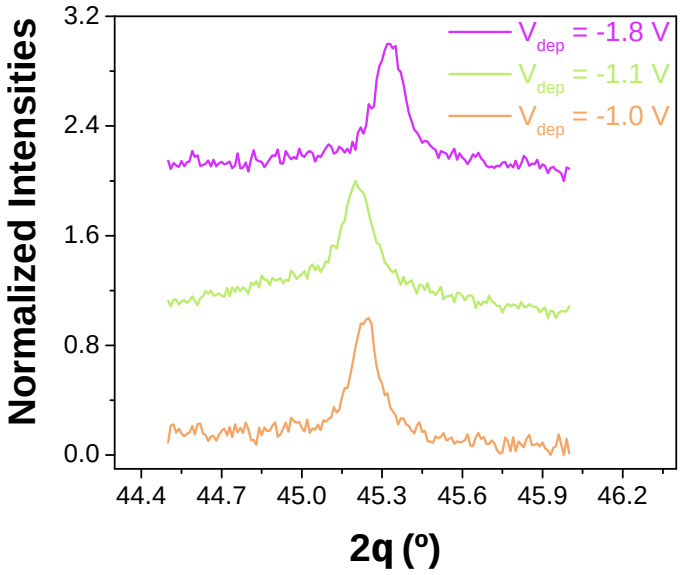


FIGURE 6.10: XDR diffraction patterns of the thin films electrodeposited with applied potentials of -1.0, -1.1 and –1.8 V. The peaks represented correspond to bcc (110).

Figure 6.11 presents the crystallite size obtained for each potential applied as well as the lattice parameter calculated with Bragg's Law (eq. 6.2). One can observe that the lattice parameter does not change despite the V_{dep}, for all films this parameter is ~ 2.83 $\AA$. This parameter is in good agreement with the phase diagram of FeCo and with the results present in the literature [12]. However, the crystallite size does not present a monotonous behavior, which is again related to the poor statistics of the XRD peaks.

With the study in Cu tape substrate using the test solution, one observed that lower applied potentials lead to higher depositions rates, that: the stoichiometry does not change with this parameter, nor does the lattice parameter. As for the crystallite size, a correlation was not observed.

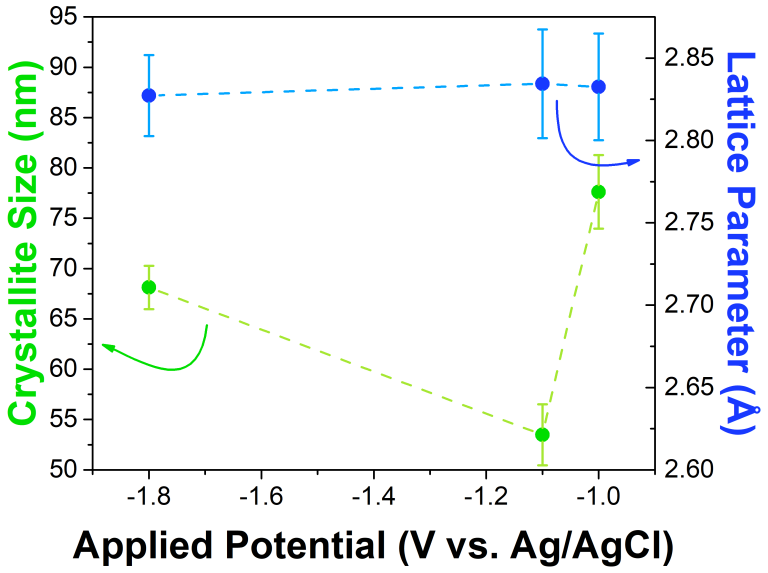


FIGURE 6.11: Crystallite size (green dots) and lattice parameter (blue dots) of the corresponding thin films electrodeposited with applied potentials of -1.0, -1.1 and –1.8 V.

6.2.2 $Fe_{20}Co_{80}$ Nanowires

After the study in Cu substrate, the same study was conducted in NAMs to observe the correlation between the FeCo 1D nanowires and 2D thin films. NAMs were fabricated through mild anodization following the procedure described in section 5.2. To conduct this experiment, two groups of samples were prepared with two different parameters, D_p and V_{dep} (see table 6.2). Group A had a fixed D_p of $\sim$ 45 (typical diameters for these MA conditions with oxalic acid) and varied the V_{dep}. Group B had a fixed D_p of $\sim$ 75 (resulting from the pore opening controlled chemical dissolution, as mentioned in chapter 5) and varied the V_{dep}. For all samples, electrodeposition was performed using the test solution ($Fe_{20}Co_{80}$), the same used to fabricate the thin films during 360 s.

Group	Sample	V_{dep} (V vs. Ag/AgCl)	D_p (nm)
A	1	-1.1	$\sim$ 45
	2	-1.2	
	3	-1.8	
B	4	-1.1	$\sim$ 75
	5	-1.8	

TABLE 6.2: Resume of the samples to be fabricated by electrodeposition in NAMs using the test solution.

Figure 6.12 shows the electrodeposition curves (j versus t) of the fabricated samples. By comparing these curves with the thin films, the nucleation stage is much faster in time than the ones for the NWs. The curves of samples 3 and 5 do not present the typical initial decrease in current, which corresponds to the charge of the double layer. Instead, they start already with j decreasing. This can be due to the Δt step between data points, where the Δt chosen was not small enough to collect data in this nucleation stage. As for the curves of samples 1 and 4, they do not show a pronounced maximum, being stable through time. In contrast, sample 2 shows a mixed behavior between the curves of samples 1 and 3, presenting a j_{max}, but not the full nucleation stage as observed for the thin films.

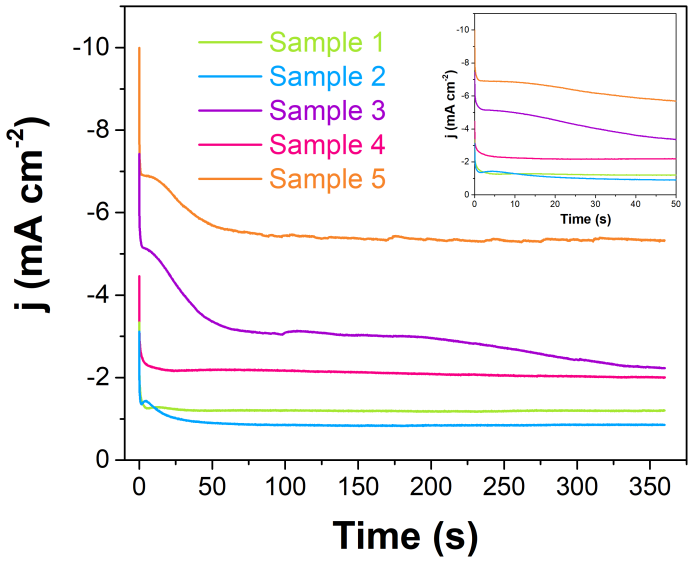


FIGURE 6.12: Electrodeposition curves of the NWs with D_p of ∼45 and ∼75 nm fabricated using the test solution with V_{dep} of -1.1, -1.2 and -1.8 V (vs. Ag/AgCl).

$j(t)$ curves under the same V_{dep} = -1.8 V (samples 3 and 5) exhibit an overall j value in comparison with the ones under V_{dep} = -1.1 V (samples 1 and 4). Furthermore, $j(t)$ curves for samples with the same V_{dep} (samples 1 and 2, and 3 and 5), the ones corresponding to a $D_p \sim 75$ nm present higher current, resulting in a higher Q value, as shown in figure 6.13. Despite having different D_p, all the NAMs were fabricated in the same MA conditions providing them all the same overall porosity. So, one must conclude that the increase in current is due to the increase in the D_p. Larger D_p leads to higher j values along the electrodeposition at the same V_{dep} because there is a larger contact area that decreases the

resistance of the system. So, larger the pores lead to higher $j(t)$ curves, higher the V_{dep} also means higher $j(t)$ curves.

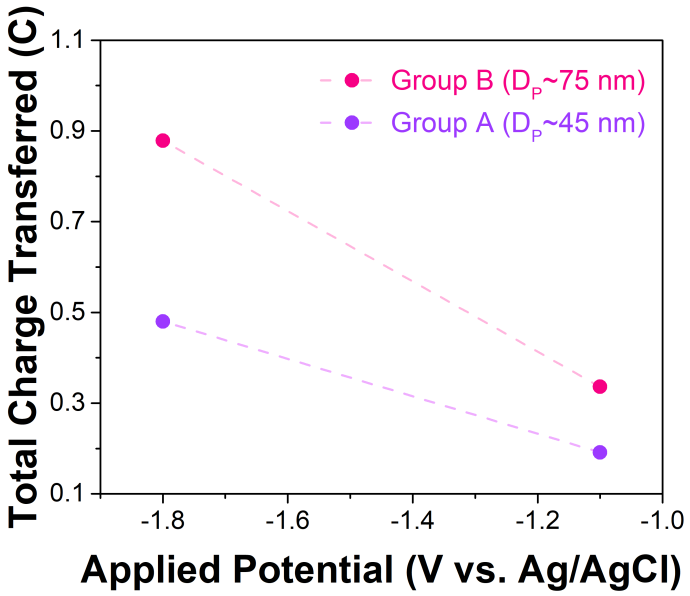


FIGURE 6.13: Total charge transferred in the electrodeposition of the NWs with D_p of ∼45 and ∼75 nm fabricated using the test solution with V_{dep} of -1.1 and -1.8 V (vs. Ag/AgCl).

6.2.2.1 Morphological Characterization

Figure 6.14 a) b) and c) shows SEM images, with different magnifications, of the NWs with D_p = ∼45 nm electrodeposited at V_{dep} of -1.1, -1.2 and –1.8 V, respectively. All the images were obtained with backscattered electrons, so different chemical elements are shown with different contrasts. In the images presented, it is possible to observe the thin film of Au that was sputtered in the NAMs and the NWs of Au firstly electrodeposited (as described in synthesis section 4). These Au features are represented with white pixels, while the FeCo NWs are less brightened (grey). This occurs due to atomic number (Z) dependence with the brightness of the image (Z(Au) = 79, Z(Fe) = 26 and Z(Co) = 27). Thus, from now on, all SEM images of the NWs will be in this SEM electronic mode of operation since it allows better visualization of the NWs and their study.

One can observe that the lower the V_{dep}, the longer NWs are obtained since higher depositions rates are achieved. The NWs length acquired from the SEM images correspond to 1.3±0.8, 1.6±0.3 and 3.6±0.3 μm for the V_{dep} of -1.1, -1.2 and –1.8 V, respectively.

In this work, we introduced a new variable in the original Faraday's Law of Electrolysis (already defined in the chapter 3, equation 6.3), the porosity (P), which through simple

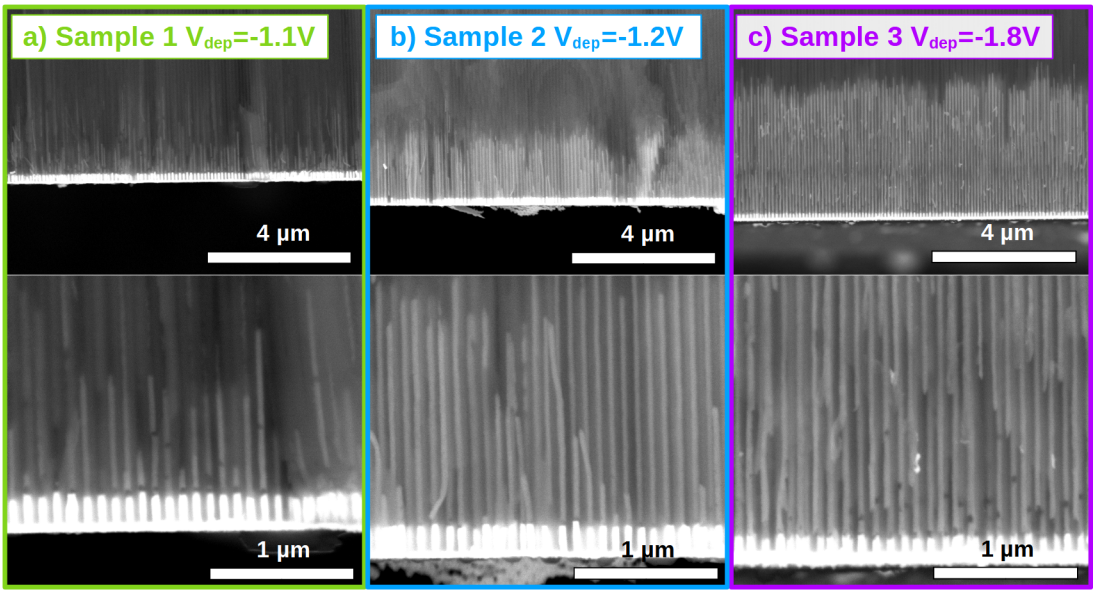


FIGURE 6.14: SEM images of the NWs electrodeposited at V_{dep} of a) -1.1, b) -1.2, and c) –1.8 (V vs. Ag/AgCl) in membranes with $D_p \sim 45$ nm (group A).

manipulation of the equations 3.8 and 6.3 allowed us to obtain a new Faraday's Law of Electrolysis adapted for the NWs geometry features, given by:

$$L = \frac{M}{nF\rho A} \cdot \frac{Q}{P} \tag{6.5}$$

where This simple and straightforward result, so far, not found in the literature as far as our knowledge, allowed us to estimate the NWs length without resorting to SEM techniques.

Figure 6.15 presents the comparison between the NWs lengths obtained by SEM images and by the ones obtained through estimation with the adapted Faraday's Law of Electrolysis. The calculation of the estimated lengths by the expression 6.5 took into account the experimental features extracted from the SEM images, like NWs diameters, to calculate the porosity (eq. 3.8) of each sample.

One can observe that theoretical estimation does not correspond to the experimental results, being lower than the latter. This is because, at the time of these electrodeposition experiments, it was clearly seen that the deposition did not occur in all the NAM area. This means that the NAMs were electrodeposited only in certain sites of the all sample area. In this sense, the deposition was not uniformly distributed in the total area of the electrodeposition sample. Instead, it was concentrated on those spots, leading to longer NWs in localized regions of the sample. An explanation for the non-uniform NWs growth may be attributed to non-optimized experimental procedures such as some regions where

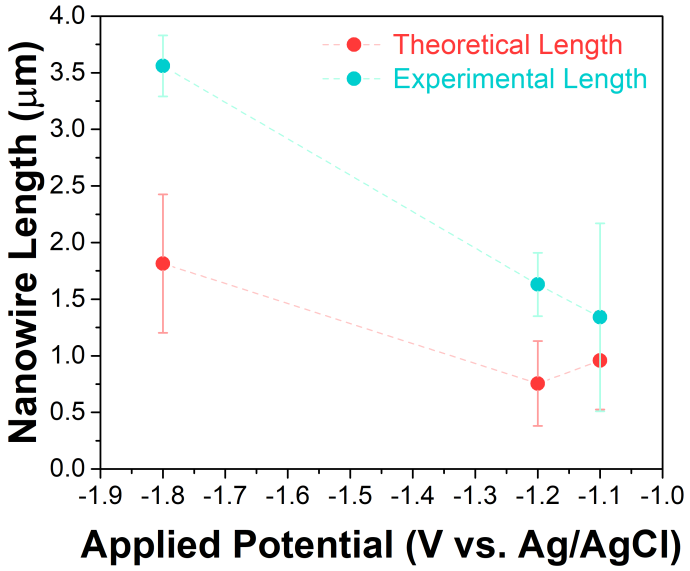


FIGURE 6.15: Comparison between theoretical and experimental NWs lengths of the NWs electrodeposited at V_{dep} of -1.1, -1.2 and –1.8 (V vs. Ag/AgCl) in membranes with $D_p \sim 45$ nm.

not all pores bottoms were open or a poor Au sputtering coating that did not allow the electrical contact with the copper base in all regions of the NAM.

Figure 6.16 a) and b) shows SEM images, with different magnifications, of the NWs with D_p of ∼75 nm electrodeposited at V_{dep} of -1.1 and –1.8 V, respectively. Once again, the lower V_{dep} (-1.8 V) corresponds to the longer NWs. The NWs lengths acquired from the SEM images correspond to 0.64±0.09 and 1.1±0.8 for the V_{dep} of -1.1 and –1.8 V, respectively.

In figure 6.17 is presented the NWs lengths obtained by SEM images and by estimating them with equation 6.5, as done previously. The results obtained are much more consistent because the electrodeposition in these NAMs was uniform in all the sample area.

Table 6.3 summarizes the results obtained for both groups of samples, A and B. It is presented the NWs geometrical values extracted from SEM images like, D_p and L_{exp}, the P calculated by equation 3.8, stoichiometry obtained by EDS analyse, Q obtained by the equation 6.4, and finally L_{teo} estimated with the equation 6.5. In general, the stoichiometries acquired correspond to what was expected by the test solution in thin films. When compared with the thin films, the average stoichiometry is more closer to what was expected, $Fe_{20}Co_{80}$. However, the EDS error is considerable, so one can not rely completely

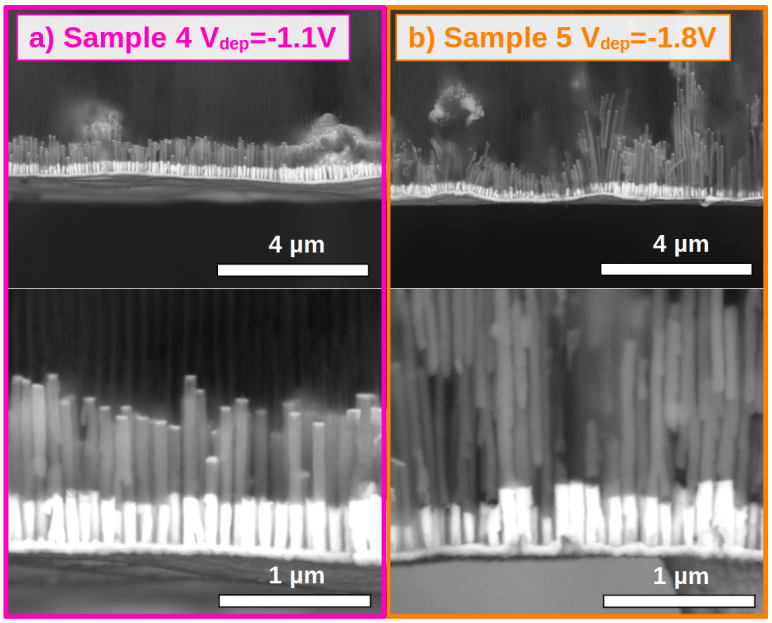


FIGURE 6.16: SEM images of the NWs electrodeposited at V_{dep} of a) -1.1 and b) –1.8 (V vs. Ag/AgCl) in membranes with $D_p \sim 75$ nm (group B).

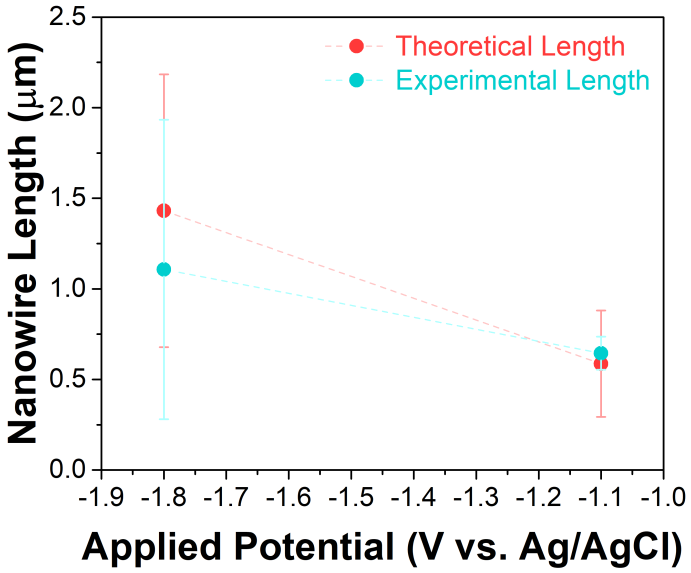


FIGURE 6.17: Comparison between theoretical and experimental NWs lengths of the NWs electrodeposited at V_{dep} of -1.1 and –1.8 (V vs. Ag/AgCl) in membranes with $D_p \sim$ 75 nm.

on it. Accordingly, because the NWs growth was not uniform in the electrodeposition area for the samples with $D_p \sim 45$ nm, it was not possible to calculate an accurate deposition rate. As for the samples with $D_p \sim 75$ nm, a deposition rate of $\sim 1.8 \pm 3\ nm\ s^{-1}$ was obtained for the NWs electrodeposited with V_{dep} = -1.1 V. For the case of the sample with V_{dep} = -1.8 V the deposition rate was also not calculated, since the NWs height

presents a great dispersion resulting in a not uniform deposition. Porosities obtained for group A were on average P = 17 %, while for the group B of samples with larger pores was obtained on average P = 4.5 %.

Sample	Stoichiometry	D_p (nm)	P	Q (C)	L_{teo} (μ m)	L_{exp} (μ m)
1	$Fe_{21}Co_{79}$	45±5	0.16±0.07	0.1917	1.0±0.4	1.3±0.8
2	$Fe_{20}Co_{80}$	42±5	0.14±0.07	0.1408	0.8±0.4	1.6±0.3
3	$Fe_{20}Co_{80}$	50±4	0.21±0.07	0.4803	1.8±0.6	3.6±0.3
4	$Fe_{22}Co_{78}$	73±9	0.4±0.2	0.3361	0.6±0.3	0.7±0.1
5	$Fe_{20}Co_{80}$	76±10	0.5±0.3	0.8785	1.4±0.8	1.1±0.8

TABLE 6.3: Resume of the results obtained with the samples fabricated by electrodeposition in NAMs using the test solution. The stoichiometries represented were obtained through EDS analysis.

6.2.2.2 Structural Characterization

Figure 6.18 shows the XRD patterns of both groups of the NWs samples considered in this study. Full patterns can be found in the figure 8.2 of the appendix 8; a diffractogram of only Au NWs in a NAM is also present in figure 8.3 of the appendix 8. Figure 6.18 displays the diffractogram patterns from 40 to 50 in the 2θ range to emphasize the FeCo peaks. Additionally, the peaks indexed to the Au NWs contributions are highlighted in grey and the ones indexed to the FeCo are displayed in black. Samples 1, 2, 3 and 4 present a single peak around 45° (see figure 6.18 a)), corresponding of FeCo alloy with a preferential growth in (110) direction and a bcc structural phase, which is in accordance with the results previously seen for the $Fe_{20}Co_{80}$ thin films. In addition, in figure 6.18 a) and b), is represented a pattern corresponding to a NAM with a thin film of Au deposited by sputtering and Au NWs (electrodeposited at V_{dep} = -1.0 V for 360 s) to better be compared with the XRD patterns obtained for the $Fe_{20}Co_{80}$ samples. However, an expected result was obtained, the XRD pattern of sample 5 (D_p = 76±10 nm and V_{dep} = -1.8 V) shows the existence of two structural phases, bcc and fcc. The bcc phase reveals two peaks that correspond to (110) and (211) directions, and the fcc phase also presents two peaks that correspond to (111) and (220) directions. Actually, Bran et al. [66] reported that FeCo NWs alloys with Co content higher than 78 %, showed a mixture of bcc and fcc structural phases, and it is consistent with the phase diagram of FeCo bulk alloy present in figure 4.1. This may be indicative that samples 1, 2, 3 and 4 have content of Co lesser than 78 %, contrary to what was acquired with EDS.

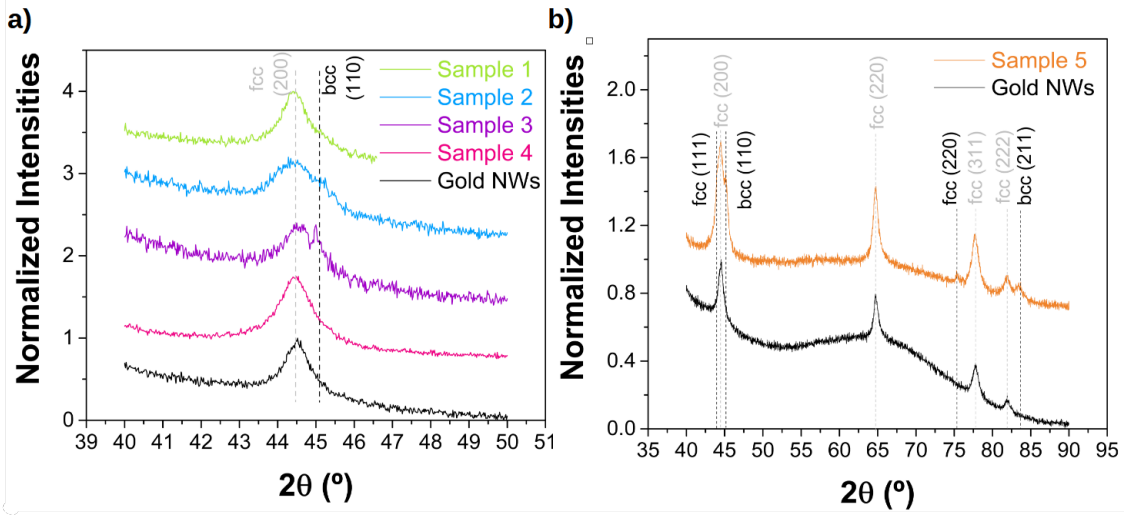


FIGURE 6.18: XDR diffraction patterns of the samples a) 1, 2, 3, 4, and b) 5, comparing with the XDR diffraction pattern of a sample with a thin film of Au and Au NWs.

Overall, in this study in NAMs with different D_p using the test solution, one was able to conclude that lower V_{dep} leads to longer and uniform $Fe_{20}Co_{80}$ NWs. Structural phase results are consistent with the literature, wherefrom a certain at. % of Co, there is a coexistence of two structural phases (bcc and fcc). In addition, by changing the V_{dep} (-1.1 V to -1.8 V) or D_p features, it does not influence much the alloy stoichiometry.

6.3 Fe_xCo_{1-x} (x = 10, 50, 90) alloys

This section presents an electrodeposition study for different solutions, first in thin films deposited in Cu tape substrate and then in NAMs, similarly as befero.

Aiming different FeCo stoichiometries ($Fe_{10}Co_{90}$, $Fe_{50}Co_{50}$ and $Fe_{90}Co_{10}$), three solutions with different concentrations of Fe and Co were prepared. Their compositions and concentrations are shown in the table 6.4 below.

	$Fe_{10}Co_{90}$	$Fe_{50}Co_{50}$	$Fe_{90}Co_{10}$
$FeSO_4 \cdot 7H_2O$	0.02 M	0.09 M	0.16 M
$CoSO_4 \cdot 7H_2O$	0.16 M	0.09 M	0.02 M
H_3BO_3		0.16 M	
$C_6H_8O_6$		0.06 M	

TABLE 6.4: Compositions of the solutions prepared to obtain alloys with stoichiometries of FeCo ($Fe_{10}Co_{90}$, $Fe_{50}Co_{50}$ and $Fe_{10}Co_{10}$), following the suggested by Bran et al. [66].

6.3.1 Fe_xCo_{1-x} (x = 10, 50, 90) Thin Films

Firstly, the solutions were electrodeposited in copper tape substrates to obtain thin films. Since the test solution showed higher deposition rates and good homogeneity in both thin films and NWs depositions for the potential -1.8 V (vs. Ag/AgCl), the new solutions were studied using this potential.

Figure 6.19 presents the electrodeposition characteristic curves (j versus t) obtained for each solution using V_{dep} = -1.8 V (vs. Ag/AgCl).

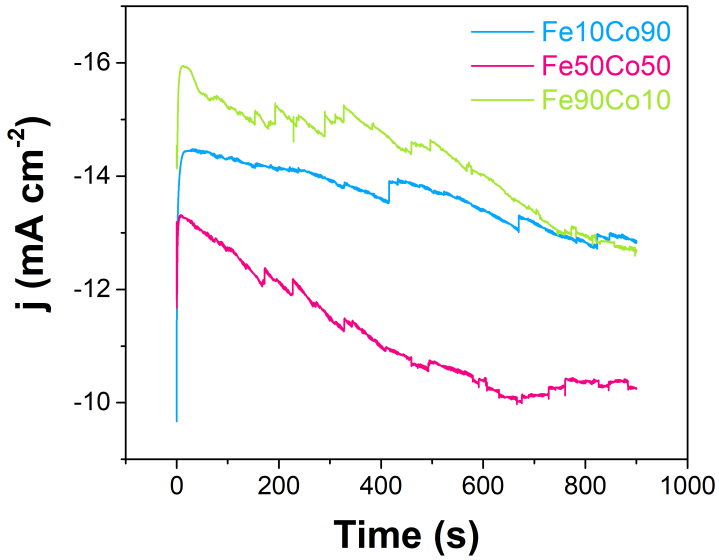


FIGURE 6.19: Electrodeposition curves of the thin films fabricated in Cu tape using the ($Fe_{10}Co_{90}$, $Fe_{50}Co_{50}$ and $Fe_{90}Co_{10}$) solutions at a potential of -1.8 V (vs. Ag/AgCl).

The thin film thickness was calculated using the classical Faraday's Law of Electrolysis 3.10. ρ was calculated having into consideration the theoretical stoichiometry of each solution. The thickness obtained were 4.15, 3.58 and 4.81 μm for the thin films electrodeposited using the solutions $Fe_{10}Co_{90}$, $Fe_{50}Co_{50}$ and $Fe_{90}Co_{10}$, respectively, and a V_{dep} of -1.8 V (vs. Ag/AgCl). Figure 6.20 is represented the relationship between the film thickness and at. % of Fe.

Through the behavior of the electrodeposition curves and the thicknesses obtained for each solution, one can see that there is no clear relation between the overall j_{max} values and the Fe and Co content in the solutions. However, it is clear that the solution for $Fe_{90}Co_{10}$ leads to thicker films with V_{dep} = -1.8 V.

The nucleation process was characterized by comparison with the Scharifker and Hills model [62]. The electrodeposition curves present in figure 6.21 were normalized to $j/j_m \sim$

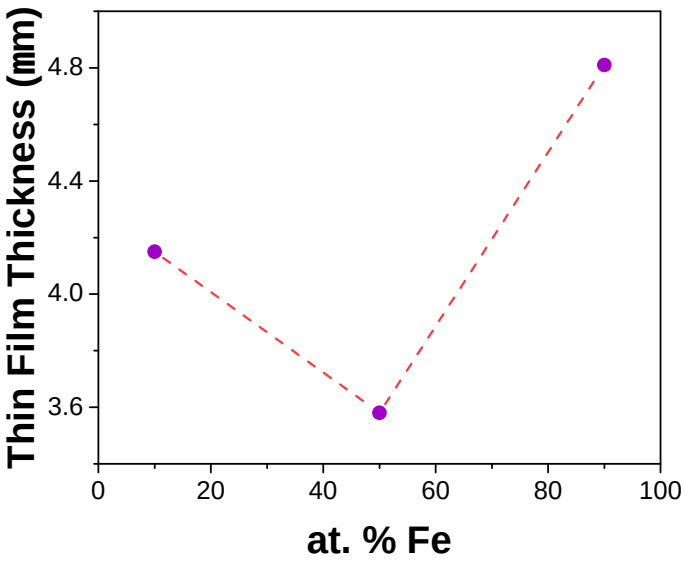


FIGURE 6.20: The dots correspond to the thin films thickness obtained using the solutions with different concentrations of Fe and Co, by applying a V_{dep} of -1.8 V (vs. Ag/AgCl).

t/t_m in order to obtain non-dimensional curves. The parameters j_m and t_m for each curve are presented in the table 6.5.

	j_m $(A \cdot cm^{-2})$	t_m (s)
$Fe_{10}Co_{90}$	6.39	20.9
$Fe_{50}Co_{50}$	5.9	7.3
$Fe_{90}Co_{10}$	7.05	11.2

TABLE 6.5: j_m and t_m of current density curves obtained with different concentrations of Fe and Co electrodeposited at -1.8 V (vs. Ag/AgCl).

From the dimensionless curves presented in figure 6.21 one can observe that all the electrodeposition curves normalized do not follow the 3D instantaneous nucleation model exactly. One can observe that the nucleation is much faster than the theoretical instantaneous nucleation. However, the potential applied does not influence the nucleation type for the three solutions, as the experimental curves overlap. Also, once again, for $t/t_m > 1$ the experimental data starts to deviate from the theoretical curve, as previously observed in the case of $Fe_{20}Co_{80}$ thin films.

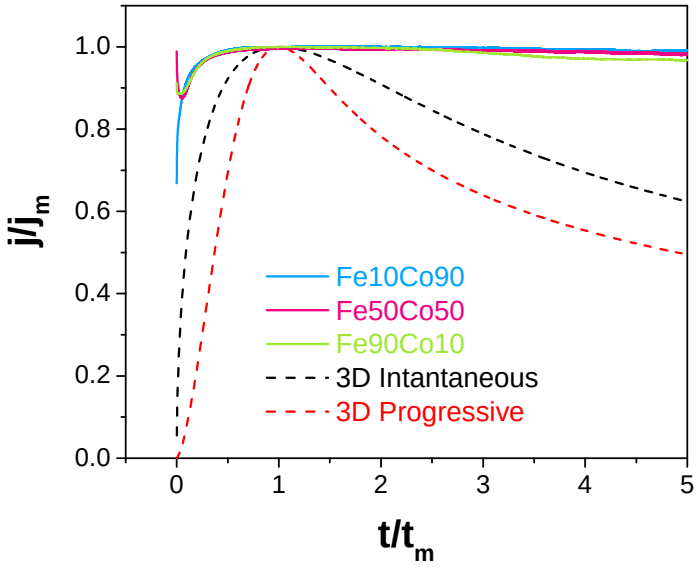


FIGURE 6.21: Electrodeposition curves comparison with the theoretical model of 3D progressive and instantaneous nucleation.

6.3.1.1 Morphological Characterization

Figure 6.22 a) b) and c) shows SEM images of the three thin films electrodeposited at -1.8 V (vs. Ag/AgCl), with theoretical stoichiometries of $Fe_{10}Co_{90}$, $Fe_{50}Co_{50}$ and $Fe_{90}Co_{10}$, respectively, with different magnifications. As one can observe from the SEM images, the change in stoichiometry affects the morphological structure of the thin films. The film with stoichiometry of $Fe_{90}Co_{10}$ presents a morphology similar to the $Fe_{20}Co_{80}$ thin films. However, the other two thin films, $Fe_{10}Co_{90}$ and $Fe_{50}Co_{50}$, show a different morphology, where instead of granular morphology, there is some kind of fibers. We believe that the main reason for this fiber-like morphology is due to electrolyte contaminations. These films had a bad/insufficient electrolyte removal with deionized water after the electrodeposition. In this specific case, the thin films produced were rinsed very softly because they were very fragile. Despite the morphology observed at a lower magnitude, the morphology observed at higher magnitude show an underline granular morphology, similar to $Fe_{90}Co_{10}$ thin films, but with smaller grains, where $Fe_{50}Co_{50}$ shows the smallest grain sizes.

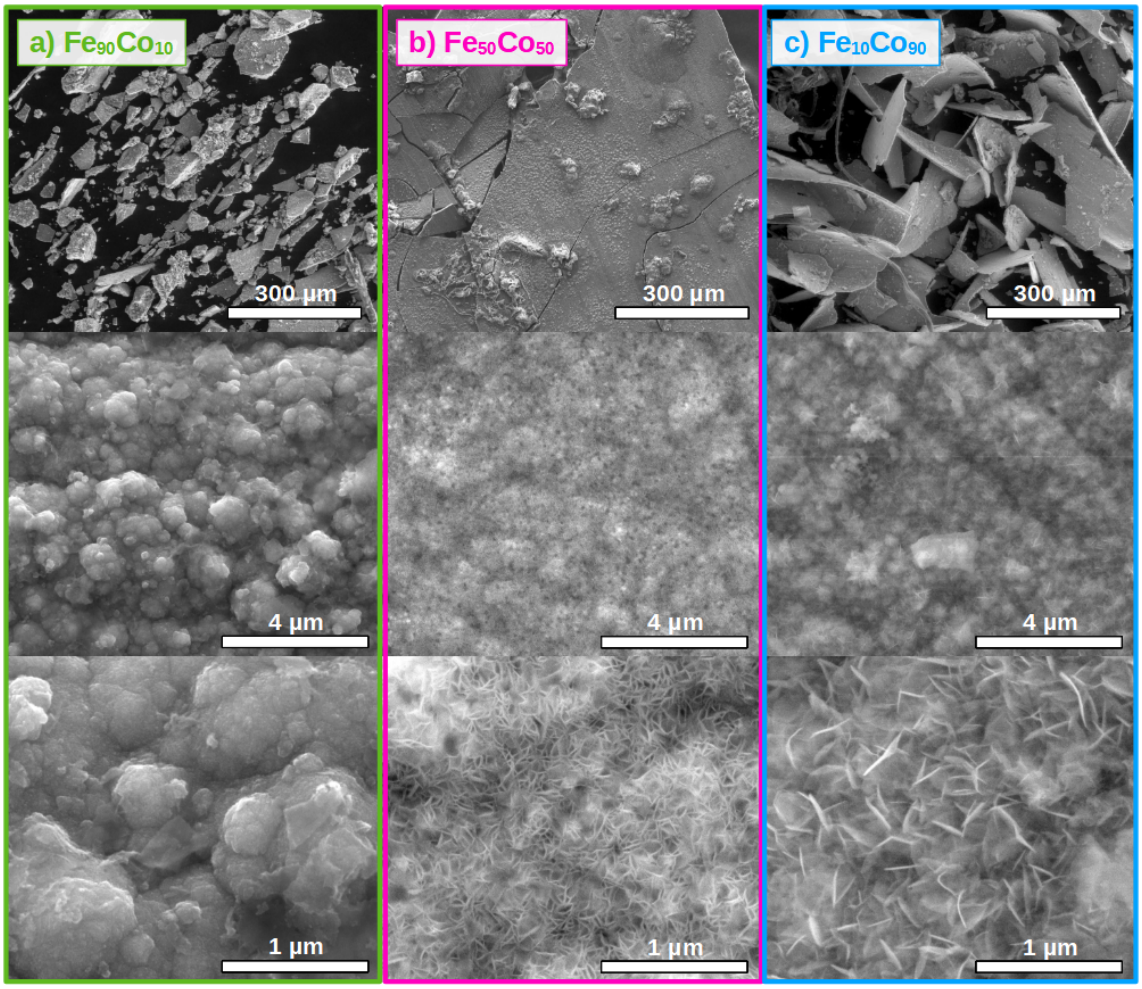


FIGURE 6.22: SEM images from the thin films electrodeposited in Cu tape using solutions $Fe_{10}Co_{90}$, $Fe_{50}Co_{50}$ and $Fe_{90}Co_{10}$ at -1.8 V (vs. Ag/AgCl).

6.3.1.2 Structural Characterization

Figure 6.23 shows the XRD patterns of the thin films with theoretical stoichiometries of $Fe_{10}Co_{90}$, $Fe_{50}Co_{50}$ and $Fe_{90}Co_{10}$ electrodeposited with V_{dep} of –1.8 V. The patterns were obtained using the Bragg-Brentano geometry in the configuration theta-2theta, in the 2θ range from 30 to 90 at a speed of 7.5 deg/min and at room temperature.

Figure 6.23, only the FeCo peaks are identified, as the thin films were peeled off the copper tape substrate. The XRD diffraction patterns of the thin films with stoichiometries $Fe_{50}Co_{50}$ and $Fe_{90}Co_{90}$ present two pronounced peaks (110) and (211) corresponding to the bcc FeCo phase. Whereas the thin film with stoichiometry $Fe_{10}Co_{90}$ shows peaks at (111) and (220) corresponding to the fcc FeCo phase. All patterns reveal a polycrystallinity degree as they were slightly grinded for XRD measurements.

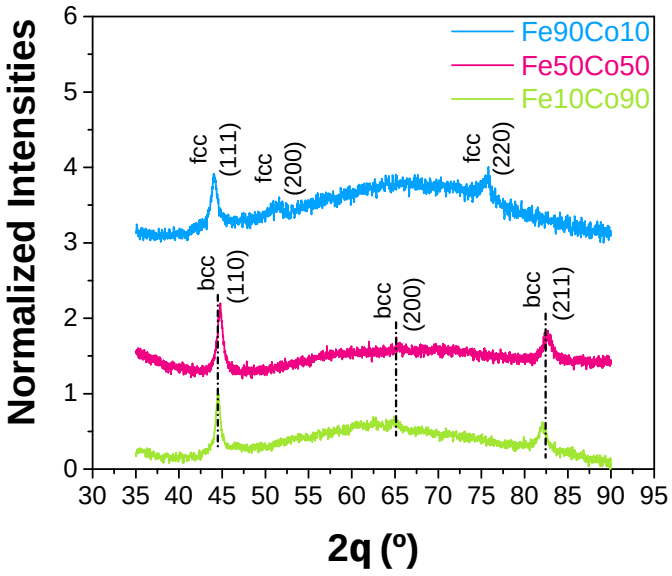


FIGURE 6.23: XDR diffraction patterns for peeled off thin films with stoichiometries of $Fe_{10}Co_{90}$, $Fe_{50}Co_{50}$ and $Fe_{90}Co_{90}$ (the stoichiometries of the thin films are theoretical).

The crystalline grain sizes obtained (using Scherrer equation) for the thin films with theoretical stoichiometries of $Fe_{90}Co_{90}$, $Fe_{50}Co_{50}$ and $Fe_{10}Co_{90}$ were, as an average of the two peaks more pronounced, 12.3±0.5 nm, 9.4±0.3 nm, and 9.7±0.9 nm, respectively. Figure 6.24 presents the grain size and the lattice parameter as a function of at. % of Fe. The grain size increases with Fe content, as demonstrated by the literature. As observed in figure 6.24, the thin film with stoichiometry of $Fe_{10}Co_{90}$ has the largest lattice parameter, 3.0±0.1 $\AA$. This is because this thin film has an fcc structural phase, which is characteristic of this stoichiometry. Also, all the other thin films have similar lattice parameters, about 2.6 $\AA$, because they share a bcc structural phase.

Comparing the graphic present in figure 6.24 with the one present in figure 6.2 one can observe that the tendencies are similar. However, all the quantities in figure 6.2 are slightly higher, which means that the crystalline size increases with the at. % of Fe, and the lattice parameter is constant during the bcc phase and increases when the structural phases change to an fcc.

With the study in Cu tape using solutions with different concentrations of Fe and Co while maintaining the V_{dep} of –1.8 V, one was able to observe that the film thickness is strongly correlated to the at. % of Fe and Co in the solution. Also, the passage from a bcc structural phase to an fcc one was observed, similar to the bulk.

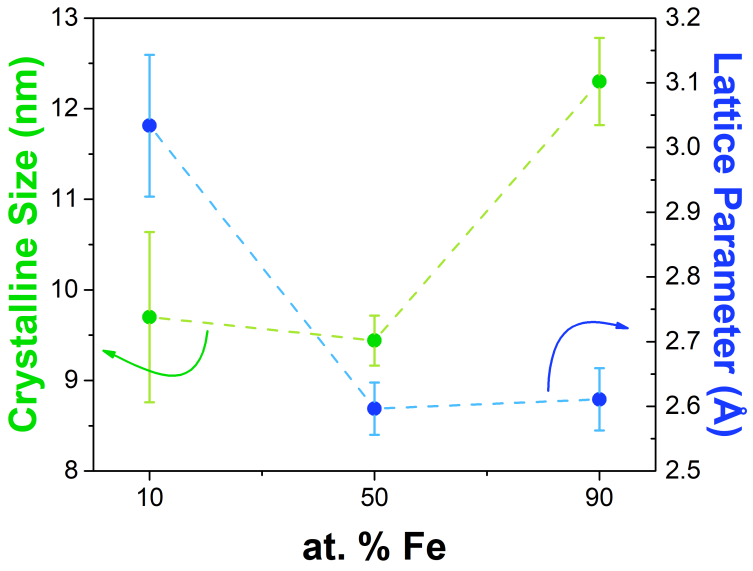


FIGURE 6.24: Crystalline size (green dots) and lattice parameter (blue dots) of the corresponding thin films electrodeposited using solutions $Fe_{10}Co_{90}$, $Fe_{50}Co_{50}$ and $Fe_{90}Co_{90}$ at -1.8 V (vs. Ag/AgCl).

6.3.2 Fe_xCo_{1-x} (x = 10, 50, 90) Nanowires

After the study of thin films deposited in Cu tape substrate, the same approach was conducted in NAMs to obtain NWs to obtain the correlation between 1D nanostructures with 2D thin films. NAMs were produced through MA following the procedure described in section 5.2. To conduct this experiment the parameters D_p (∼45 nm), V_{dep} (-1.8 V (vs. Ag/AgCl)) and deposition time were maintained constant, varying only the solutions, to obtain once again the three different stoichiometries (see table 6.6).

Sample	Solution	V_{dep} (V vs. Ag/AgCl)	D_p (nm)
6	$Fe_{10}Co_{90}$	-1.8	
7	$Fe_{50}Co_{50}$	-1.8	∼ 45
8	$Fe_{90}Co_{10}$	-1.8	

TABLE 6.6: Resume of the samples to be fabricated by electrodeposition in NAMs using the solutions prepared with different concentrations of Fe and Co.

The electrodeposition curves of the fabricated samples are shown in figure 6.25. By comparing these curves with the ones of the $Fe_{20}Co_{80}$ NWs (figure 6.12), only the curve of sample 1 presents a similar trend, stable j along the electrodeposition time. The curves of samples 7 and 8 show an initial increase in current and then decay to ∼ 0. Sample 7 shows a initial stage with a constant j (until ∼ 50 s) but rapidly decreases to ∼ 0. However,

sample 8 does not stabilize, from the first seconds of the electrodeposition instantaneously goes to ~ 0. The fact that the current drops so rapidly to zero can imply the evolution of H_2 inside the nanopores that prevent the electrodeposition. Nevertheless, it can also be related to the reduction potential of the different solutions.

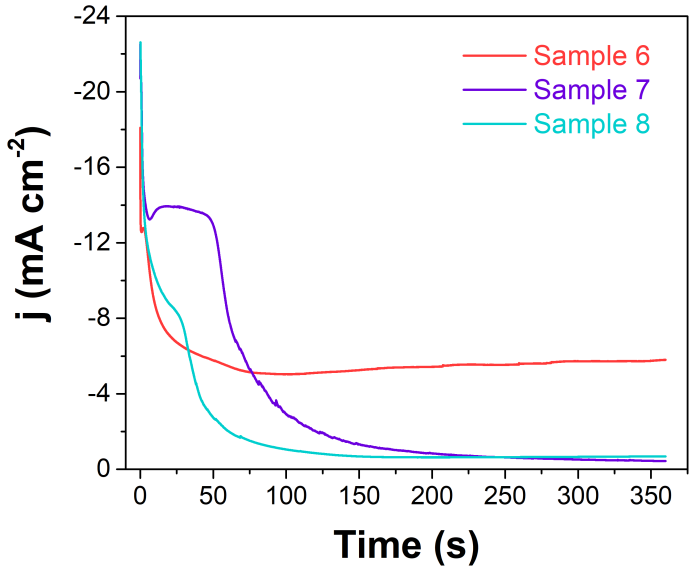


FIGURE 6.25: Electrodeposition curves of the NWs with D_p of ~45 nm fabricated using solutions with different concentrations of Fe and Co, at a V_{dep} of -1.8 V (vs. Ag/AgCl).

6.3.2.1 Morphological Characterization

Figure 6.26 a) b) and c) shows SEM images, with different magnifications, for the samples 6 ($Fe_{10}Co_{90}$), 7 ($Fe_{50}Co_{50}$) and 8 ($Fe_{90}Co_{10}$). All the images where obtained with backscattered electrons, so different elements are showed with different contrasts.

The NWs lengths acquired from the SEM images correspond to 5.3±0.3, 0.13±0.02 and 0 μm for the solutions $Fe_{10}Co_{90}$, $Fe_{50}Co_{50}$ and $Fe_{90}Co_{10}$, respectively, thus higher concentrations of Co in the electrodeposition solution leads to longer are the NWs at the same V_{dep} of –1.8 V.

The SEM images result present in figure 6.26 corroborate with the electrodeposition curves behavior: stable j leads to NWs homogeneous growth and constant growth rate (sample 6); the non-stable j (decay to ~ 0) or only stable for few seconds (sample 7) leads to smaller NWs since only for a short time the deposition occurred; the rapid decrease to 0 of sample 8 means that the deposition of the NWs did not occur, or only in some random

nanopores. This sample exhibits some very small darker regions in the periphery that can correspond to the presence FeCo NWs.

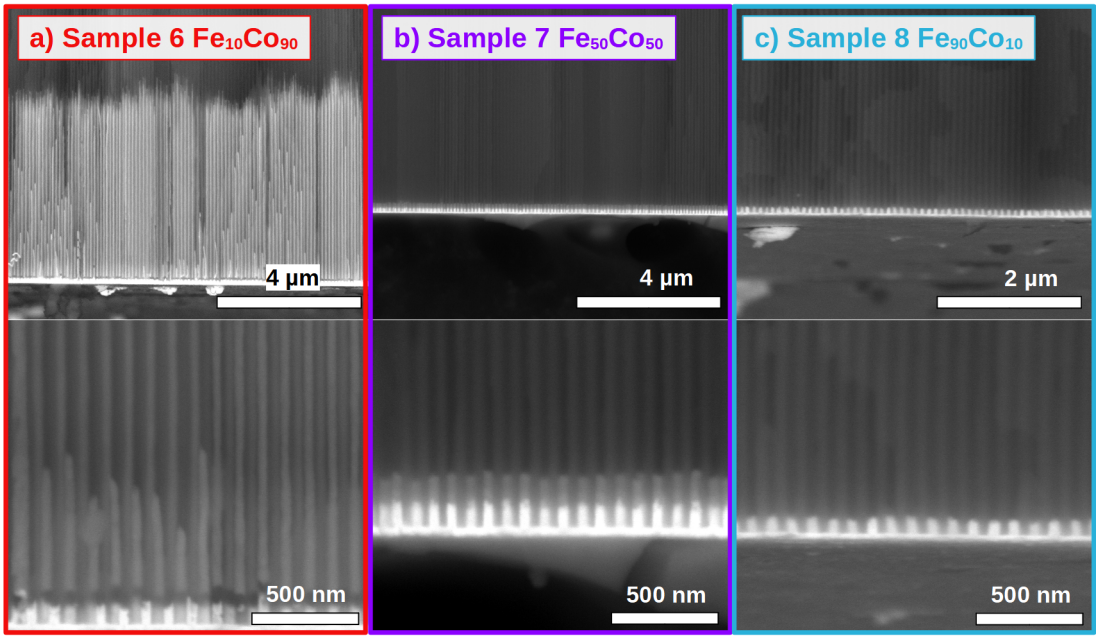


FIGURE 6.26: SEM images of the NWs electrodeposited at V_{dep} –1.8 (V vs. Ag/AgCl) in membranes with $D_p \sim 45$ nm using solutions with different concentrations of Fe and Co.

The results obtained lead to the conclusion that the three solutions prepared have different optimum electrodeposition potentials. The solution $Fe_{10}Co_{90}$ showed a good electrodeposition for the potential of -1.8 V, while for the solutions $Fe_{50}Co_{50}$ and $Fe_{90}Co_{10}$ this potential is not suitable for a uniform and constant NWs electrodeposition.

By applying the adapted Faraday's Law of Electrolysis (equation 6.5) the theoretical length of the NWs was estimated, using the D_p obtained from SEM images. Figure 6.27 presents the comparison between the NWs lengths obtained by SEM images and by estimation.

Table 6.3 presents the results obtained for samples 6, 7 and 8, where the stoichiometries presented for samples 6 and 7 were obtained by performing EDS.

The deposition rate of the solution $Fe_{10}Co_{90}$ into a NAM with $D_p \sim 44$ nm at a potential of -1.8 V is estimated to be $\sim 15 \pm 7\ nm\ s^{-1}$, by the results from sample 6. The deposition rate was not calculated for the other solutions due to the not optimum electrodeposition conditions described previously for these samples.

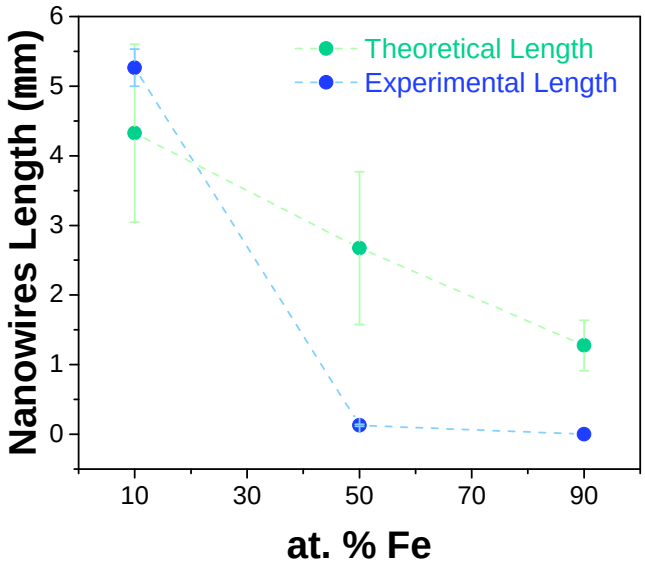


FIGURE 6.27: Comparison between theoretical and experimental NWs lengths of the NWs electrodeposited at V_{dep} –1.8 (V vs. Ag/AgCl) in membranes with $D_p \sim 45$ nm using solutions with different concentrations of Fe and Co.

Sample	Stoichiometry	D_p	P	Q (C)	L_{teo} (μ m)	L_{exp} (μ m)
6	$Fe_{14}Co_{86}$	44±3	0.16±0.05	0.9143	4.3±3.3	5.3±0.3
7	$Fe_{49}Co_{51}$	45±5	0.17±0.07	0.5504	2.7±1.1	0.1±0.2
8	$Fe_{90}Co_{10}$	48±3	0.19±0.05	0.2904	1.3±0.4	0

TABLE 6.7: Resume of the results obtained with the samples fabricated by electrodeposition in NAMs using solutions with different concentrations of Co and Fe. The stoichiometries represented for the samples 6 and 7 where obtained with EDS whereas the one of the sample 8 is theoretical.

6.3.2.2 Structural Characterization

Figure 6.28 shows the XRD patterns of the NWs samples 6 ($Fe_{10}Co_{90}$) and 7($Fe_{50}Co_{50}$). Full patterns can be encountered in the figure 8.4 of the appendix 8. The peaks indexed to the Au NWs are highlighted in grey, and those indexed to the FeCo are displayed in black.

Samples 7 presents a single peak around 45° corresponding to FeCo alloy indicating bcc structural phase with preferential growth in (110) direction, whereas the thin films revealed to be polycrystalline. The XDR pattern of sample 6 shows a single phase of fcc FeCo with the peaks corresponding to the direction of (111) and (220) and (200). This result is consistent with what was observed in the thin film electrodeposited with the same solution.

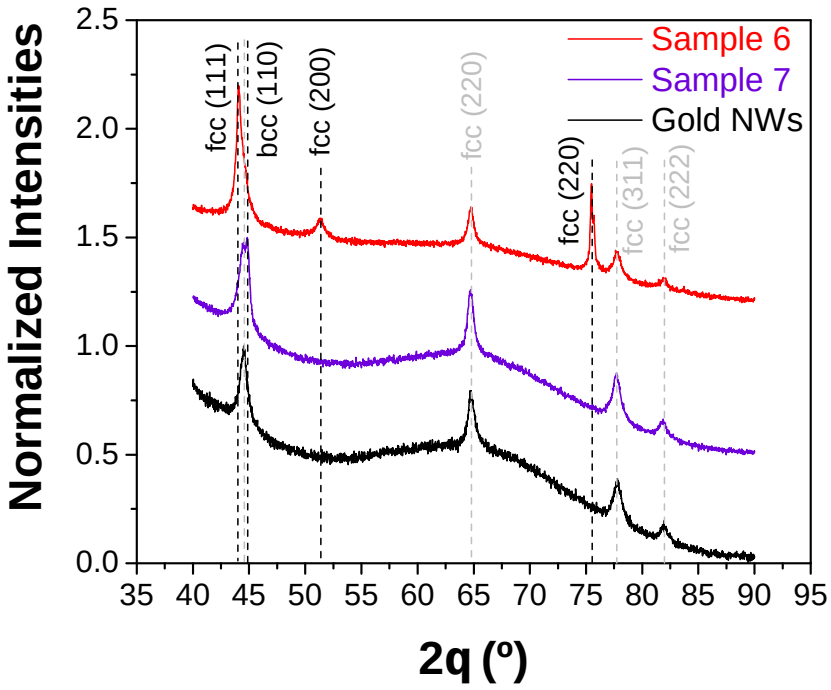


FIGURE 6.28: XDR diffraction patterns of the samples 6 and 7, comparing with the XDR diffraction pattern of a sample with a thin film of Au and Au NWs.

Through the study of electrodeposition at -1.8 V in NAMs with the same D_p using different solutions, one was able to confirm that deposition is highly dependent on the at. % of Fe and Co in the solution, as seen in the thin films. Also, the change in structural phase is consistent with the literature, wherefrom a certain at. % of Co, there is a passage from the bcc structural phase to an fcc one.

6.4 Optimization of electrodeposition potential for Fe_xCo_{1-x} (x = 10, 50, 90) Nanowires

Due to the difficulties faced to electrodeposit the solutions $Fe_{50}Co_{50}$ and $Fe_{90}Co_{10}$, an intensive study of deposition rates as a function of V_{dep} was implemented. For each solution, linear sweep voltammetry (LSV) in NAT and Au thin film was performed to find the optimal electrodeposition potential. Then a study in multisegmented Au/FeCo NWs was conducted to evaluate the NWs length with the applied potential.

6.4.1 Linear Sweep Voltammetry

LSV is a technique where the current of the working electrode is measured while the V_{dep} between the working electrode and a reference electrode is swept linearly in time. In order to compare the charge-controlled and diffusion-limited processes, LSV was performed on Au thin-film, which was electrodeposited onto a copper tape substrate, and in NATs using the three different solutions (figure 6.29). The LSV performed in the Au thin films occurred in the range from 0 to -10 V at a scan rate of 100 mV s^{-1}. The curve shows a clear charge-controlled process, where the relation between current and potential is linear. However, the LSV performed in NAMs, from 0 to -5 V range, with scan rates of 100, 200 and 400 mV s^{-1}, illustrates a combination of charge and diffusion-controlled processes. As observed, initially, the LSV curves in the NAMs follow the same linear trend as the curve obtained for the Au film, indicating that there is a similar charge-controlled process until a certain potential. The presence of a cathodic peak in the NAM evidences the existence of a mixed of charge and diffusion-controlled process for the FeCo solutions electrodeposited inside the nanopores. At high cathodic peaks (negative $j(t)$ peak for lower potentials), there is H_2 evolution resulting in gas bubbles evolution inside the nanopores, which results in a current drop. With this being, there is a limiting applied potential of the FeCo NWs deposition of inside NAM since the same does not occur for the thin films. There is also evidence of an anodic peak (positive $j(t)$ peak for higher potentials), in the range from -0.5 to 0 V, corresponding to the dissolution of FeCo, which is not completely shown in the results. Also, it is worth noticing that the reason because the LSV performed on Au thin film for the solution $Fe_{90}Co_{10}$ does not star in zero, as the others, is due to the existence of previous FeCo material deposited on the Au film.

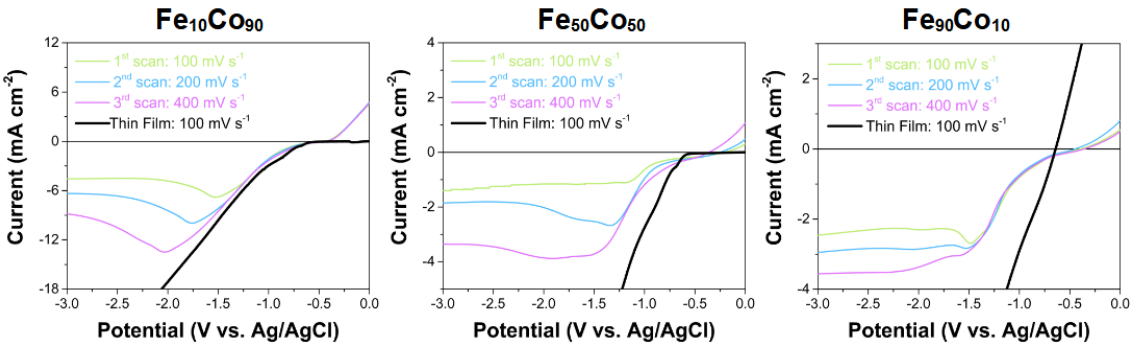


FIGURE 6.29: Linear sweep voltammetry curves obtain for each solution in NAMs (1^{st}, 2^{nd}, and 3^{rd} scans) and on Au thin film.

Overall, one can observe two different behaviors for the electrodeposition solutions in a flat substrate and NAMs, a charge controlled and a mixture of charge and diffusion controlled, respectively. Additionally, for both substrate types, the electrodeposition only occurs for V_{dep} lower than $\sim$ - 0.75 V, which is when the current turns negative.

6.4.2 Sequential FeCo Electrodeposition in a Nanoporous Alumina Template

A systematic study was performed in NAMs using the three solutions to find electrodeposition potentials that allow the uniform/homogeneous growth of FeCo NWs at constant and higher growth rates. To perform this study, the three NAMs, one for each solution, then FeCo NWs, were electrodeposited in the NAMs at constant potentials between -1.0 and -1.8 V for 6 min each. Between each layer, 6 min of Au NWs were electrodeposited at a constant potential of -1.0 V. Figure 6.30 shows the current transients during the deposition processes for each solution.

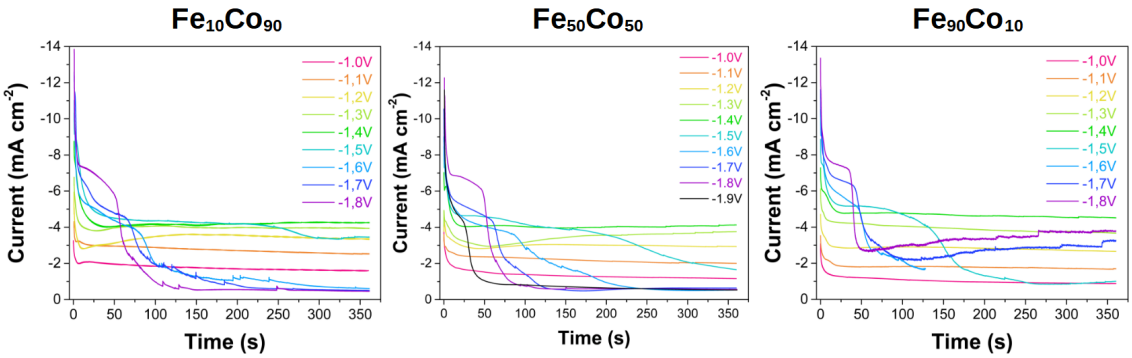


FIGURE 6.30: Current density transients, for each solution, during FeCo electrodeposition in NAMs performed at different constant potentials, between -1.0 and -1.8 V, for 6 min.

For all solutions, one can observe that for $V_{dep} \leq 1.4$ V the curves show a constant behavior, whereas for the curves corresponding to $V_{dep} \geq 1.5$ V, they tend to drop faster to low values of current as of the V_{dep} increases. So, by comparing these electrodeposition curves behavior with the ones of (fig outras) it is possible to establish that 1.4 V is more likely to be the limit V_{dep} to obtain a sample with homogeneous NWs, independently of the solution used.

Figure 6.31 shows the LSV curves, as seen previously, where the scattered points correspond to the current density values after 6 min of FeCo potentiostatic deposition for each solution. One can observe that the curves formed with the scattered points also follow the same linear trend as the film thins LSV curves for low cathodic potentials. For

higher V_{dep} than -1.4 V, the $j(t)$ curve tends to deviate from the linear behavior, being also an indicator that this potential is the limit potential for these solutions electrodeposition. Also, it is possible to observe that only for V_{dep} lower than -0.75 V the deposition starts to evolve.

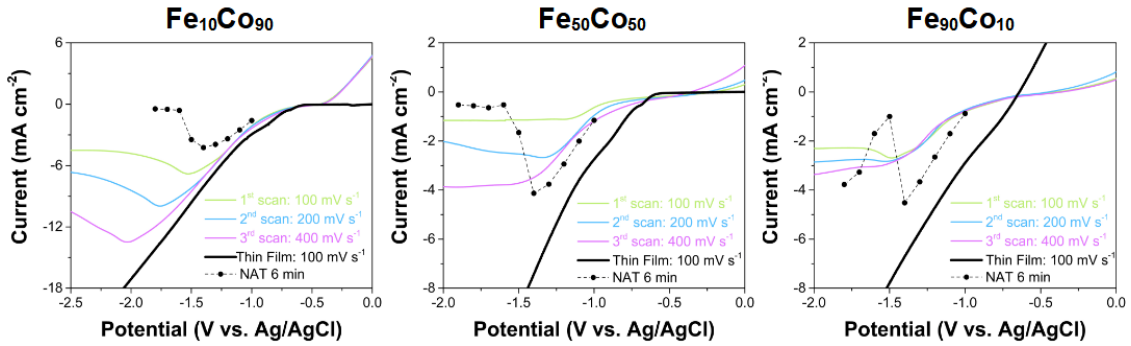


FIGURE 6.31: Linear sweep voltammetry curves obtain for each solution in NAMs (1^{st}, 2^{nd}, and 3^{rd} scans) and thin film of Au. Scattered points correspond to the current density values after 6 min of FeCo potentiostatic deposition, for each solution.

Figure 6.32 represents the total charge transferred in function of time obtained by integration of the j represented in figure 6.30. The analysis of these $Q(t)$ curves allows the control of the deposition rate. This means that by controlling the slope of the curve, one can observe if the deposition rate is constant, which is the case for $V_{dep} \leq 1.4$ V, whereas for $V_{dep} \geq 1.5$ V the slope of the curve changes in time. One can also observe that the lower the V_{dep}, the earlier the slope of the curve changes.

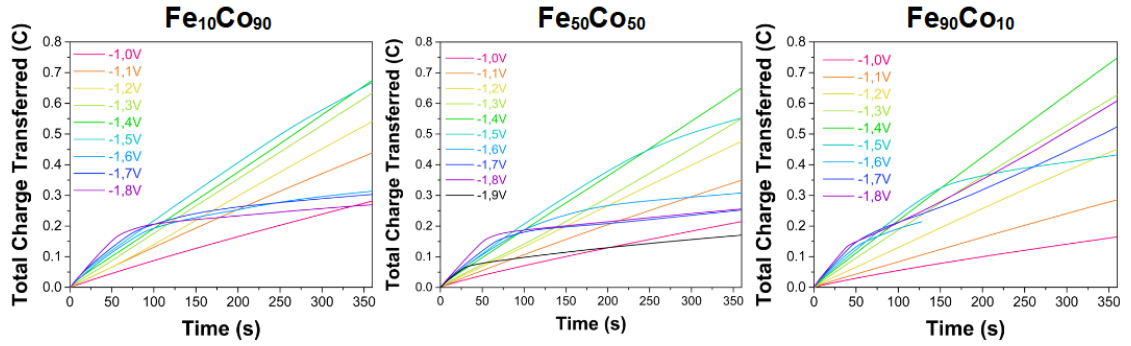


FIGURE 6.32: Total charge transferred during the process of electrodeposition at the different V_{dep} for each solution.

Figure 6.33 shows the total charge transferred after the 6 min as a function of the potential applied for each solution. Herewith is clear that it is for $V_{dep} \leq 1.4$ V that a semilinear relation is obtained, where for V_{dep} higher than -1.4 V, there is a sharp decrease in Q.

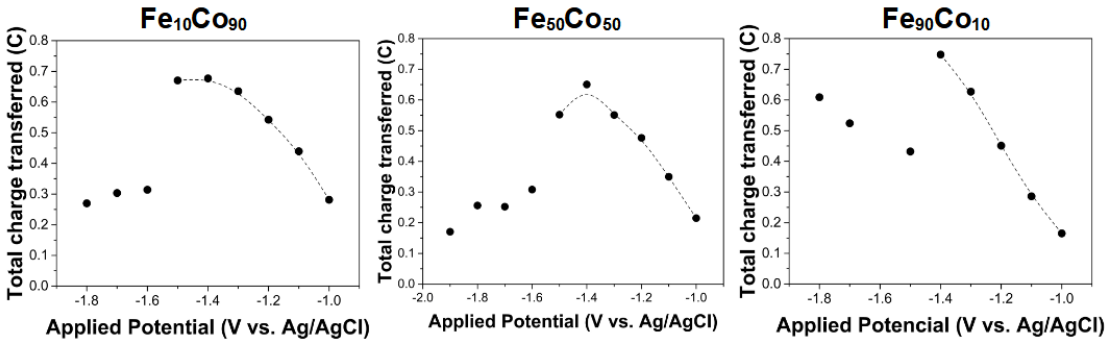


FIGURE 6.33: Total charge transferred during the process of electrodeposition at the different potentials for each solution in function of the applied potential.

Figure 6.34 displays SEM images of the multisegmented Au/FeCo NWs fabricated using the three solutions, from where it is possible to estimate the FeCo NWs length obtained with each electrodeposition potential.

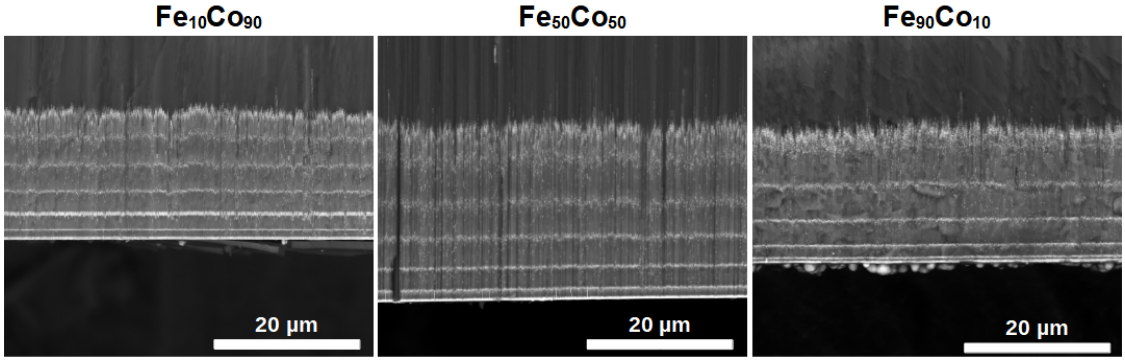


FIGURE 6.34: SEM images, obtained using backscattered electrons, of the multisegmented Au/FeCo NWs fabricated by electrodeposition of the three solutions at different potentials.

Figure 6.35 shows the relation between the estimated FeCo NWs length versus the applied potential. As one can observe, as the potential decreases, a linear relation between the NWs length and V_{dep} is observed, then a maximum is reached at -1.4 V.

Figure 6.36 shows the NWs length obtained by SEM images as a function of Q during 6 min of electrodeposition. This type of representation allows the confirmation that only for $V_{dep} \leq 1.4$ V a linear relation between NWs length and total charge transferred is obtained, meaning that it is only at these range of applied potentials that one can consider the Faraday's Law of Electrolysis to control the deposition rate. It also represented the theoretical values of the NWs length obtained by using the adapted Faraday's Law of Electrolysis, as used previously. However, one can notice a deviation between the theoretical and experimental values of NWs length. This is because the actual growth of the

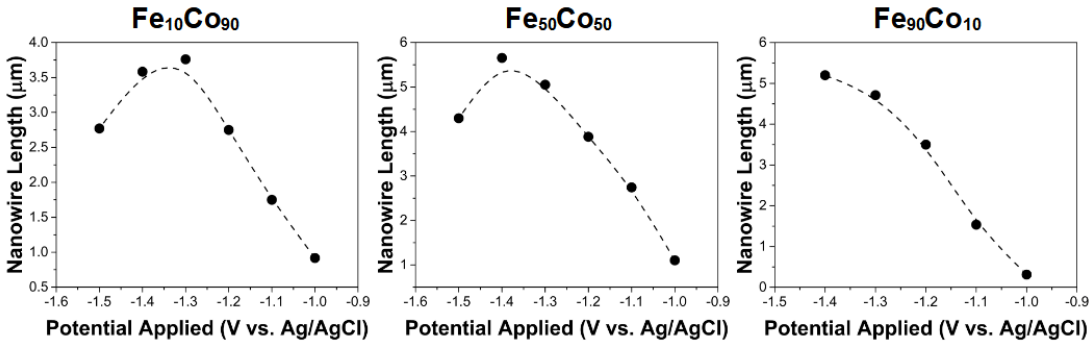


FIGURE 6.35: NWs length versus the applied potential for the three solutions, estimated by measuring the NWs in the SEM images.

NWs in the NAMs is not homogeneous. Instead, longer NWs are obtained in the center of the NAMs while smaller NWs can be encountered in the sample periphery (see figure 6.38 in the appendix 8). Therefore, experimental length values vary in the sample zone analyzed while hopefully maintaining an overall length corresponding to the theoretical value.

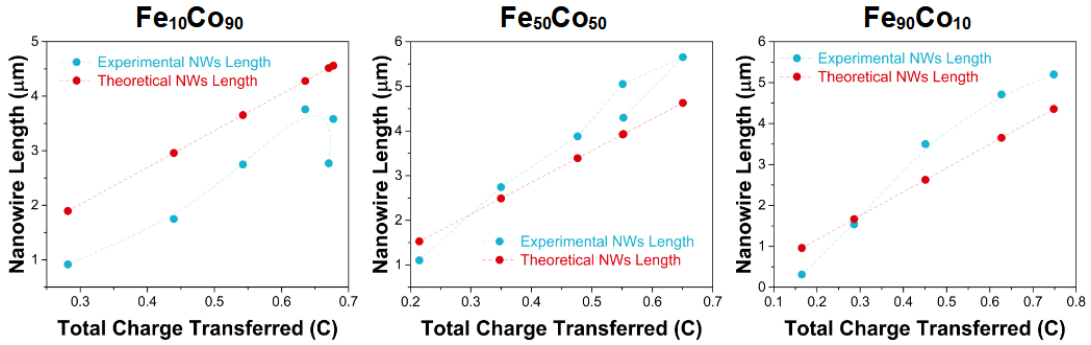


FIGURE 6.36: NWs length obtained experimentally and theoretically in function of the total charge transferred.

Figure 6.37 represents the linear relation between the NWs length and the total charge transferred for each solution. NWs with stoichiometries of $Fe_{10}Co_{90}$ and $Fe_{90}Co_{10}$ present a linear relation between -1.0 and -1.3 V, whereas the NWs with stoichiometry of $Fe_{50}Co_{50}$ present a linear relation between -1.0 and -1.4 V.

This intensive study enabled the determination of an optimal value for the electrodeposition of the different solutions, being this value -1.3 V. This optimal potential allows faster electrodeposition and a higher deposition rate without compromising the NWs homogeneity. Additionally, any V_{dep} in the range from -0.75 to -1.3 V can be used to electrodeposit any of these solutions. The only variable is the electrodeposition time, where higher potentials lead to lower deposition rates. It also verified the correlation between

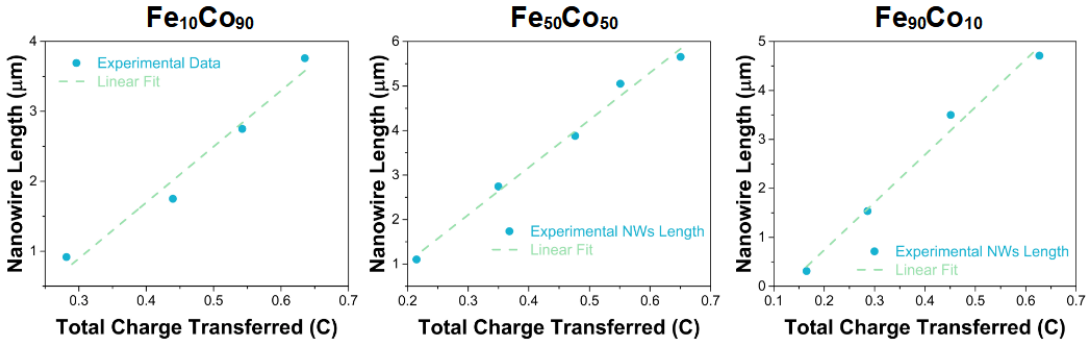


FIGURE 6.37: NWs length in function of the total charge transferred in the linear behaviour.

the experimental and theoretical values for the NWs length following the adapted Faraday's Law of Electrolysis, which showed great results. With this being said, it is now possible to tune the NWs length by controlling the total charge transferred and interpolate these results to NAMs with other values of P. Therefore, this approach allowed us to skip the SEM analysis to confirm the NWs length as we can now control NWs features.

6.5 Customization and Characterization of Fe_xCo_{1-x} (x = 10, 50, 90) Nanowires

Aiming to customize FeCo NWs alloy thermal expansion we focus on tunning two parameters, the FeCo stoichiometry, Fe_xCo_{1-x} (x = 10, 50, 90), and the NWs diameter. In this sense, six FeCo NWs samples were fabricated, categorized into two groups, C and D, differing in D_p. For group C, the NAMs were produced by HA, whereas the NAMs in group D were produced by MA, as described in chapter 5. Each group consists in three samples where each one correspond to NWs with $Fe_{10}Co_{90}$, $Fe_{50}Co_{50}$ and $Fe_{90}Co_{10}$ stoichiometries. The electrodeposition of the NWs into the NAMs was performed by using a V_{dep} of -1.3 V because this potential revealed to be the optimum V_{dep} to achieve homogeneous NWs at a high deposition rate, as seen previously. Also, by using the adapted Faraday's Law of Electrolysis (equation 6.4), one was able to estimate beforehand the total charge to transfer to obtain NWs with a length of 4 μm (a dimension that we established to obtain for all the NWs since different stoichiometries and diameters lead to different time intervals of pore filling). It is important to stress that the fabrication of this group of samples for the NTE study was only possible after the accurate and extensive optimization of the

electrodeposition conditions done in the previous sections. Where it was possible to establish controlled electrodeposition with an optimized deposition potential for different stoichiometries allowing the uniform NWs growth at a constant growth rate, a resume of the samples synthesized can be encountered in table 6.8.

Group	Sample	Stoichiometry	D_p (nm)	P_{teo}	L_{teo} (μm)	Q_{teo} (C)
C	9	$Fe_{10}Co_{90}$	~ 40	~ 0.132	~ 4	0.68
	10	$Fe_{50}Co_{50}$				0.65
	11	$Fe_{90}Co_{10}$				0.62
D	12	$Fe_{10}Co_{90}$	$\sim$130	~ 0.232	~ 4	1.09
	13	$Fe_{50}Co_{50}$				1.15
	14	$Fe_{90}Co_{10}$				1.20

TABLE 6.8: Resume of the samples to be synthesized with different D_p and stoichiometries of $Fe_{10}Co_{90}$, $Fe_{50}Co_{50}$ and $Fe_{90}Co_{10}$.

The electrodeposition time was controlled by observing the curve of the Q versus t until the desired Q was obtained, and thus controlling the NWs length for different diameters. Electrodeposition curves for all samples are represented in the figure 6.38, where one can observe that all of them are stable in time, as expected, and that the j of the samples with larger D_p possess a higher current. Sample 12 had an additional 81 s of electrodeposition that is not included in the $j(t)$ curve of this sample.

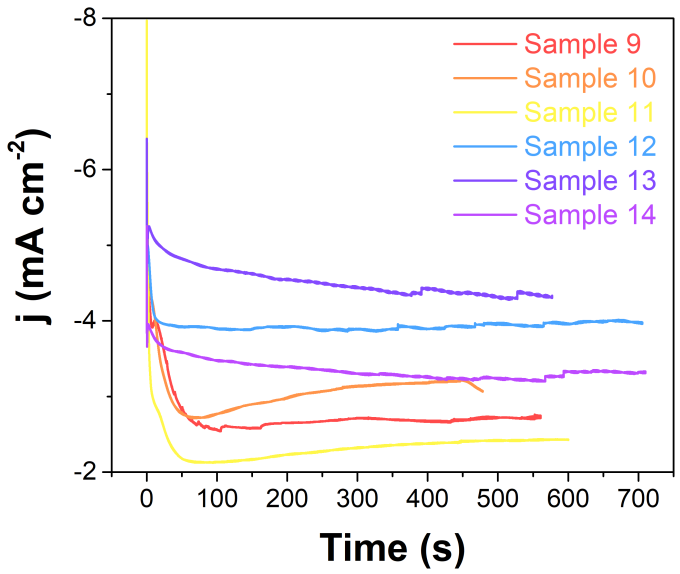


FIGURE 6.38: Electrodeposition curves of the samples 9, 10 and 11 with $\sim$ 40 nm, and samples 12, 13 and 14 with $\sim$ 130 nm.

After the electrodeposition, the Au thin film and the Au NWs were selectively removed by an Au-selective chemical etching using a solution consisting of potassium iodide, KI, for a few seconds to avoid FeCo NWs removal.

6.5.1 Morphological Characterization

Figure 6.39 presents the SEM images of the samples 9 to 14, where the NWs present homogeneous lengths.

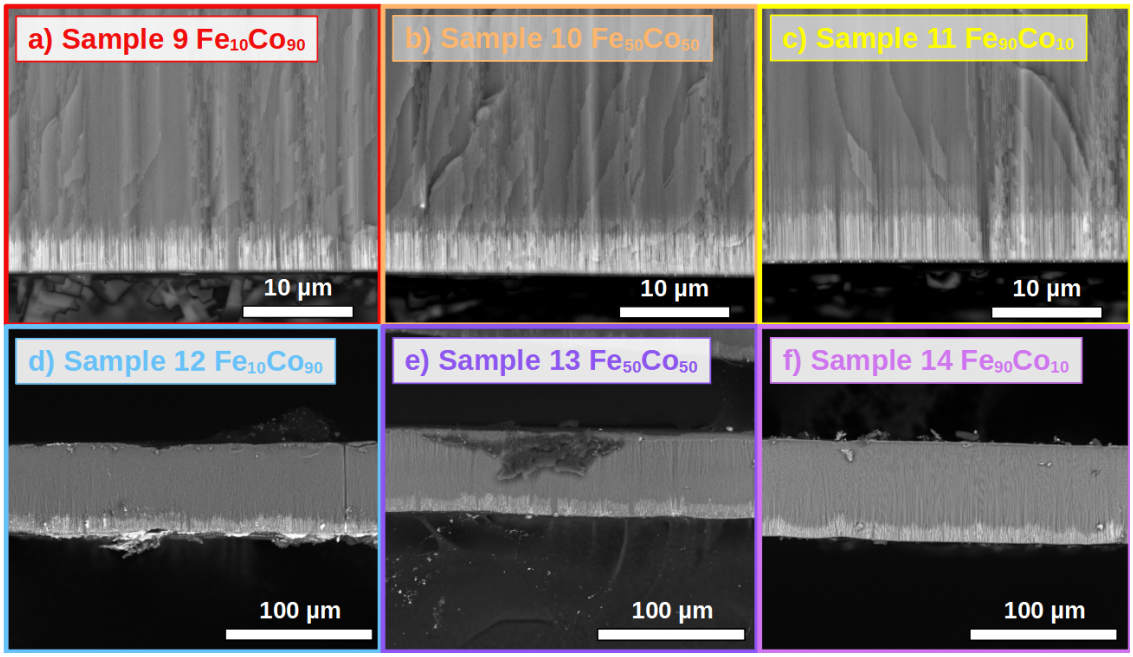


FIGURE 6.39: SEM images of the samples 9, 10 and 11 with ∼ 40 nm, and samples 12, 13 and 14 with ∼ 130 nm, obtained with backscattered electrons.

Figure 6.40 shows the SEM images of the bottom of the samples 12, 13 and 14. In these images, one can observe the bottom of the NAMs, where the pores form a hexagonal pattern.

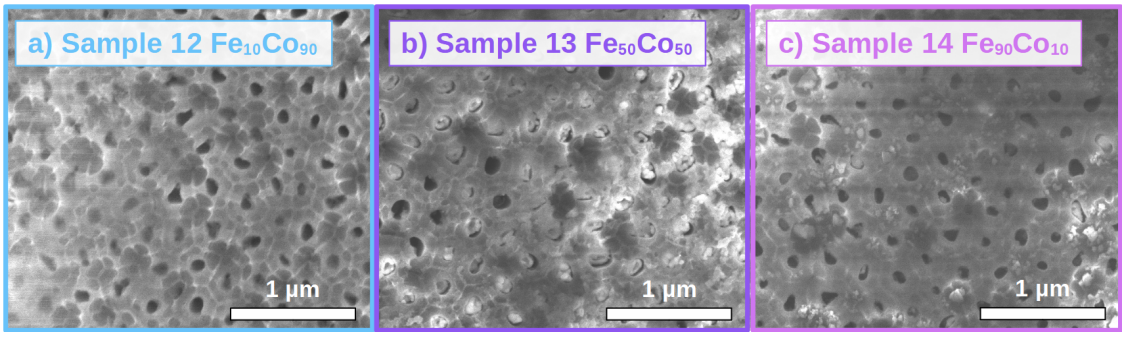


FIGURE 6.40: SEM images of the bottom of the samples 12, 13 and 14 with ∼ 130 nm, obtained with secondary electrons.

In figure 6.41 is presented the comparison between the NWs lengths obtained by SEM images and by estimation with the adapted Faraday's Law of electrolysis (equation 6.4). For the samples 12, 13 and 14 the value used as D_{int}, in the P expression (equation 3.8), was the one obtained by SEM images presented in figure 6.40. It is possible to observe that while for samples 9, 10 and 11 ($D_p \sim 45$ nm), the theoretical and experimental values are very close, for samples 12, 13 and 14 ($D_p \sim 130$ nm), the experimental values exceed the theoretical ones. The variation in length values can be associated with various reasons, as previously discussed. Since these three samples have an appearance of a good homogeneous deposition, we believe that the geometrical D_{int} and D_p have a large dispersion range of values since HA NAMs present more defects and smaller self-ordered hexagonal pores areas. This can be improved by performing longer time of HA which enables more organized nanopores.

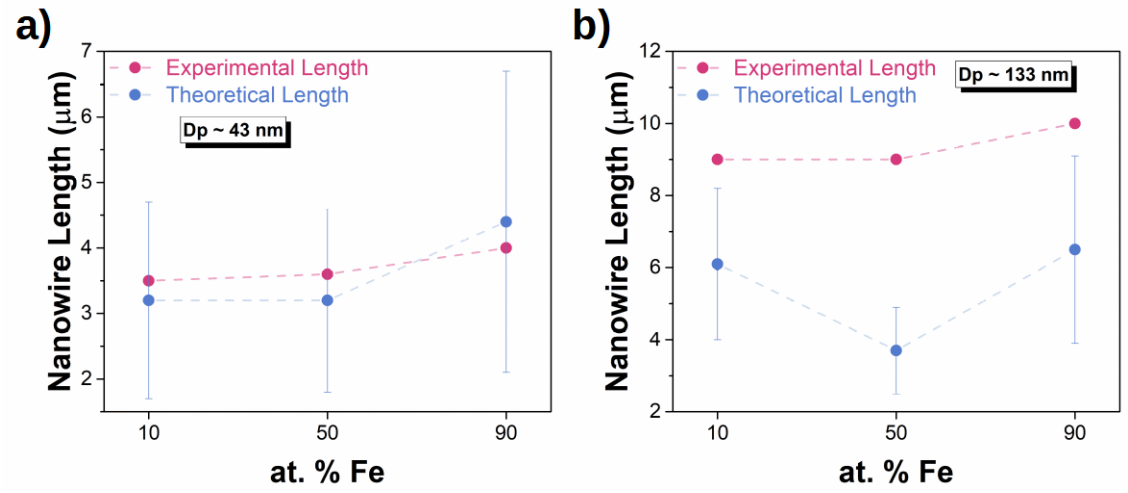


FIGURE 6.41: Nanowires length obtained experimentally in comparison with the theoretical values, for samples 9 to 14.

Table 6.9 shows the overall results obtained with these samples.

Group	Sample	Stoichiometry	D_p (nm)	D_{int} (nm)	P_{exp}	L_{exp} (μm)	Q_{exp} (C)
C	9	$Fe_{10}Co_{90}$	45±5	-	0.17±0.08	~3.5	0.6821
	10	$Fe_{50}Co_{50}$	45±5	-	0.16±0.07	~3.6	0.6494
	11	$Fe_{90}Co_{10}$	38±5	-	0.12±0.06	~4	0.6220
D	12	$Fe_{10}Co_{90}$	136±20	310±29	0.25±0.15	~9	1.3783
	13	$Fe_{50}Co_{50}$	155±21	295±25	0.33±0.18	~9	1.1526
	14	$Fe_{90}Co_{10}$	108±19	279±29	0.16±0.11	~10	1.0520

TABLE 6.9: Resume of the samples fabricated with different D_p and stoichiometries of $Fe_{10}Co_{90}$, $Fe_{50}Co_{50}$ and $Fe_{90}Co_{10}$.

6.5.2 Structural Characterization

Figure 6.42 shows the XRD patterns of the NWs samples 9 to 14. Despite the attempt to remove all Au NWs, there are always some left, and it is shown in the XRD patterns, so the peaks indexed to the Au NWs are highlighted in grey, and the ones indexed to the FeCo are displayed in black.

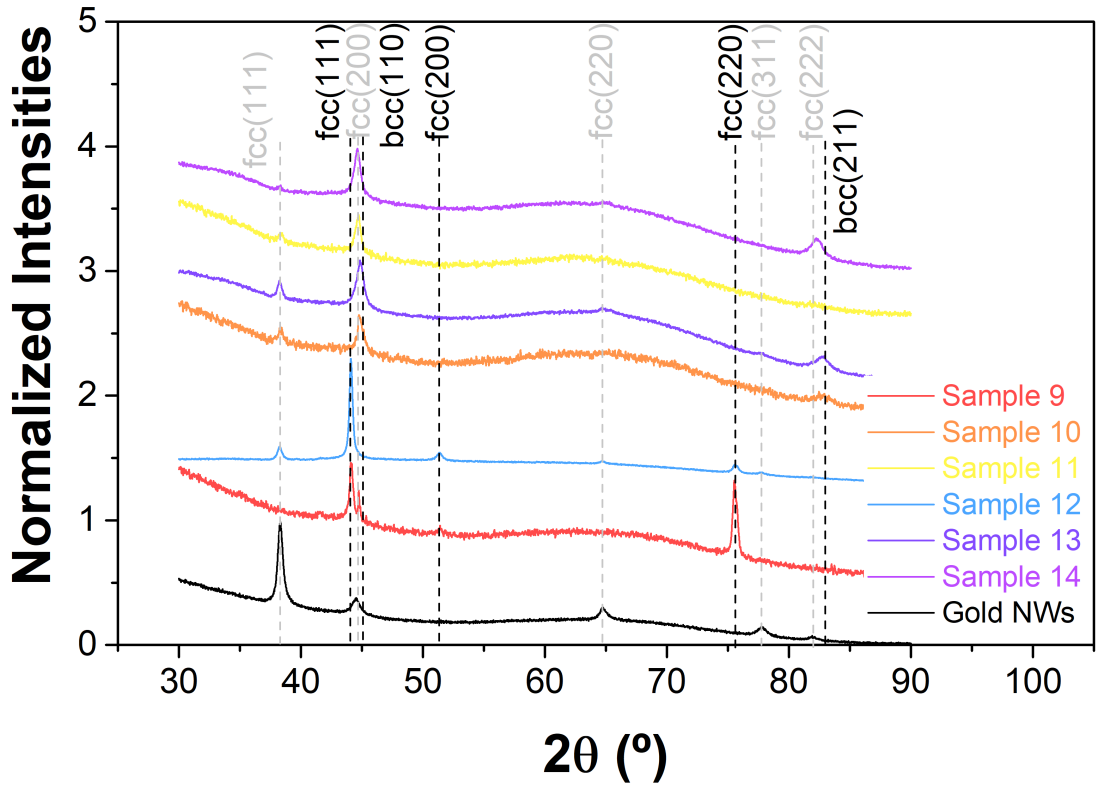


FIGURE 6.42: XRD patterns of the samples 9 to 14 with the corresponding indexes and a pattern of Au NWs to compare with pure Au diffracted peaks (indexed in grey color).

Sample 9 and 12, with a stoichiometry of $Fe_{10}Co_{90}$ and $D_p \sim 45$ and ~ 130 nm, respectively, present three peaks of FeCo, (111), (200) and (220) that correspond to a fcc single phase. The other samples, 10, 11, 13 and 14, with stoichiometries of $Fe_{50}Co_{50}$ and $Fe_{90}Co_{10}$ and $D_p \sim 45$ (sample 10 and 11) and ~ 130 nm (sample 13 and 14), have a bcc single-phase accordingly with previous results. However, because of the Au peaks, it is difficult to separate the FeCo peaks from the Au peaks in the case of a single bcc structural phase.

6.5.3 Magnetic Characterization

The magnetic properties of the samples were characterized with VSM at room temperature with $H_{\parallel}$ and $H_{\perp}$. The normalized M(H) (M/M_s) of the FeCo NWs samples 9 to 14 can be observed in the figure 6.43. Figures 6.43 a) and b) correspond to the measurements of the samples 9, 10 and 11, with $H_{\parallel}$ and $H_{\perp}$, respectively. Figures 6.43 c) and d) correspond to the measurements of the samples 12, 13 and 14, with $H_{\parallel}$ and $H_{\perp}$, respectively. Herewith, one can clearly see the effect that the shape anisotropy has on M(H). This characteristic is highly dependent on the aspect ratio of the NWs, favoring the easy axis along the NWs, where larger H_c are obtained for $H_{\parallel}$. On the other side, there are also the dipolar interactions resulting from the magnetostatic coupling of the NWs that favors the alignment of the magnetization perpendicular to the NW. There may be a small contribution of the magnetocrystalline anisotropy, which favors the alignment of the magnetization along a preferential direction, and the magnetoelastic anisotropy that depends on the stress-induced on the NWs arrays by the NAM.

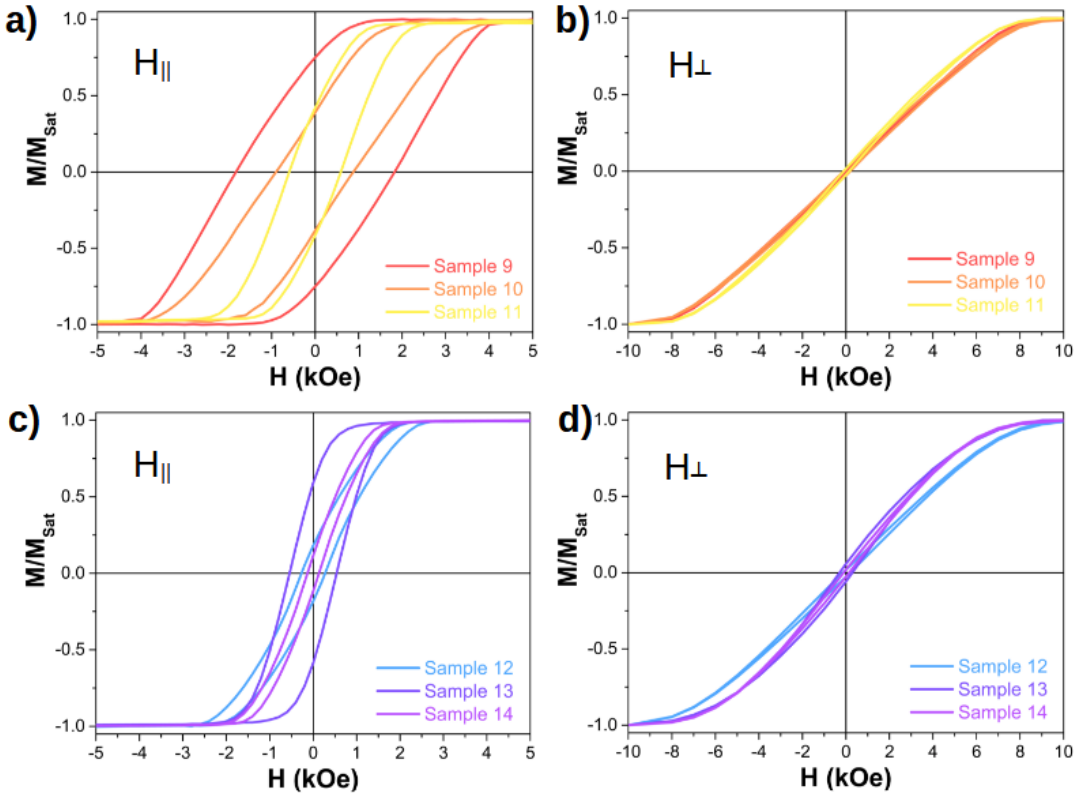


FIGURE 6.43: Normalized magnetic hysteresis curves of the FeCo NWs samples 9, 10 and 11 a) with $H_{\parallel}$ and b) $H_{\perp}$; and the FeCo NWs samples 12, 13 and 14 c) with $H_{\parallel}$ and d) $H_{\perp}$.

Figure 6.44 shows the dependence of H_c with the at. % of Fe of FeCo NWs samples.

One can observe that for $H_{\parallel}$, the NWs with D_p of $\sim$ 43 nm, samples 9, 10 and 11, present a larger H_c, proving to be harder ferromagnets than the FeCo NWs with larger D_p. Also, the FeCo NWs with D_p of $\sim$ 133 nm do not seem to present a big difference between the H_c of $H_{\parallel}$ and $H_{\perp}$.

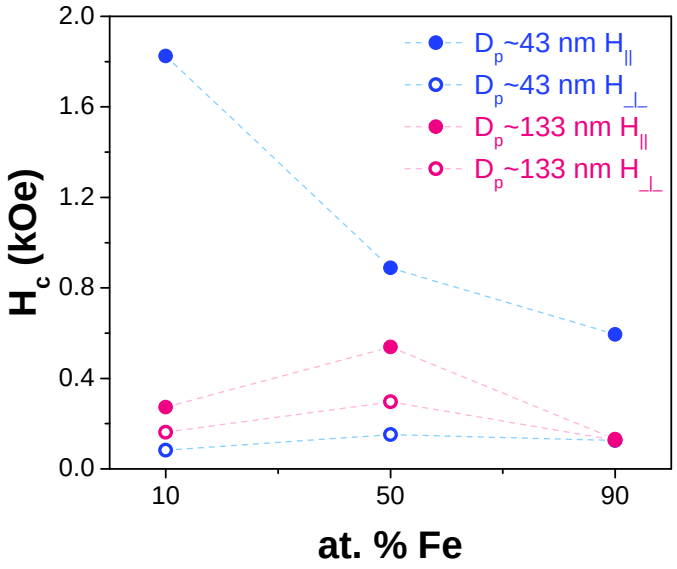


FIGURE 6.44: H_c dependence on the Fe content at room temperature for FeCo NWs with D_p of $\sim$ 43 and $\sim$ 133 nm, and lengths of $\sim$ 4 and $\sim$ 9 μm, respectively.

As for the SQ (M_r/M_s) variation with the at. % of Fe in the FeCo NWs samples, figure 6.45, the NWs with D_p of $\sim$ 43 nm show higher SQ, for $H_{\parallel}$, than the NWs with larger D_p. This can be due to a higher shape anisotropy than dipolar interaction for the NWs with lower D_p, and the opposite for NWs with higher D_p.

Despite the results discussed here, the magnetic properties of the FeCo NWs fabricated are still ongoing work. We intend to unveil the mechanism behind the behavior observed to better understand the interaction between the different magnetic contributions.

6.5.4 Thermal Expansion Characterization

Thermal expansion measurements were performed in NWs samples similar to samples 12, 13 and 14. Unfortunately, the sample corresponding to $Fe_{90}Co_{10}$ suffered complete oxidation, as the XRD measurements as a function of temperature were performed from room temperature to 640 ºC in 20 ºC steps, and each scan lasted for 30 min. The problem of oxidizing the samples led to choosing a more conservative maximum temperature for future measurements.

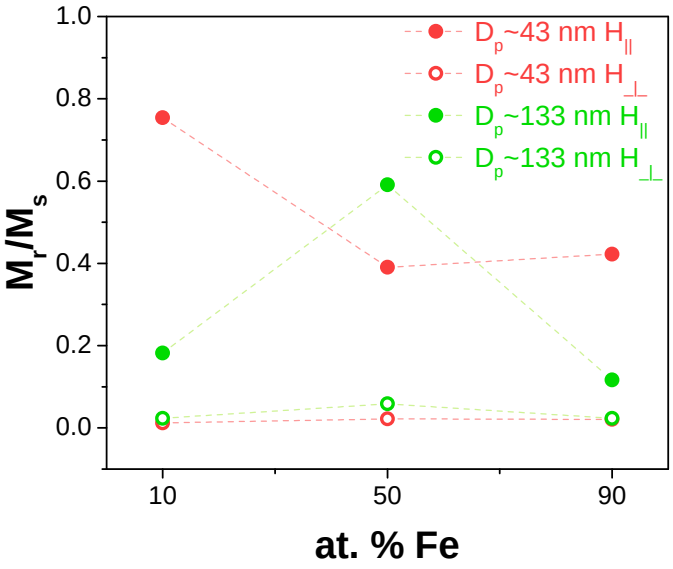


FIGURE 6.45: Variation of SQ (M_r/M_s) with Fe content at room temperature for FeCo NWs with D_p of $\sim$ 43 and $\sim$ 133 nm, and lengths of $\sim$ 4 and $\sim$ 9 μm, respectively.

Samples corresponding to the stoichiometries of $Fe_{50}Co_{50}$ and $Fe_{10}Co_{90}$ were heated from room temperature to a temperature of 651 K, and data was collected during 1 h in 20 ºC steps. Examples of the XRD patterns obtained for both samples can be encountered in figure 8.9 in the appendix 8.

Figure 6.46 a) and b) shows the unit cell volumes of the samples corresponding to the stoichiometries $Fe_{50}Co_{50}$ and $Fe_{10}Co_{90}$, respectively. These values were obtained by sequential Rietveld fits in the Full Prof program [80]. For the sample $Fe_{50}Co_{50}$, the data had to be divided into five segments because the background changed with temperature (figure 8.10 in the appendix 8). In each segment, the data was analyzed using the sequential method. For the sample $Fe_{10}Co_{90}$ the fits were all performed at once. The unit cell volumes of this sample present a linear behavior, where the values obtained during heating and cooling superimpose. The deviations can be attributed to small differences in the background of the sample, which result in not-so-good fits for some peaks of the XRD pattern as shown in figure 8.11 in the appendix 8.

From the unit cell volume as a function of the temperature for sample with stoichiometry $Fe_{50}Co_{50}$ (figure 6.46 a)), one can observe that there are several quasi-linear regimes, corresponding to the temperatures ranges: [323,532], [532,592] and [592,651] K for heating; and [651,491] and [491,301] K for cooling. This different regimes will be take into account for thermal expansion evaluation.

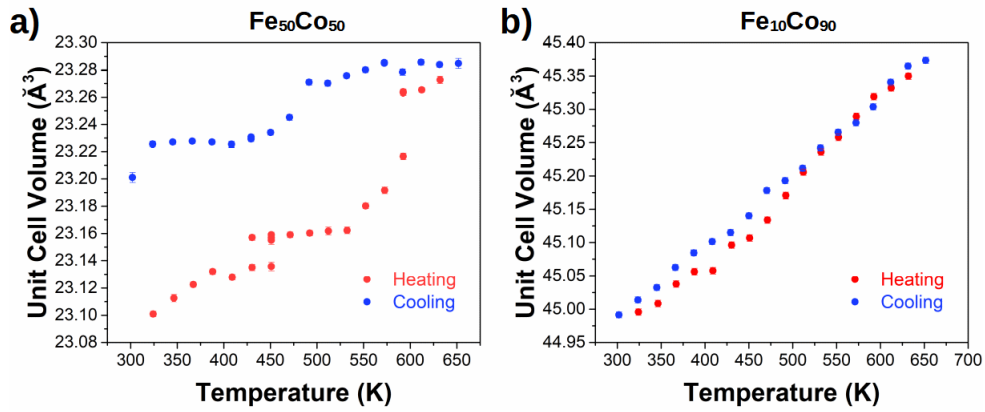


FIGURE 6.46: Unit cell volume as a function of temperature, in heating and cooling, obtained through Rietveld sequential fits for the samples with stoichiometries of a) $Fe_{50}Co_{50}$ and b) $Fe_{10}Co_{90}$.

The sample referent to $Fe_{50}Co_{50}$ shows a hysteretic behavior that is unlikely to be attributed to the thermal expansion of the NWs. Figure 8.12 in the appendix 8 shows preliminary results obtained through Rietveld fits. One can observe that the lattice parameter of the FeCo and Au show the same behavior in terms of variation, which is highly dependent on the height of the sample that also shows this same behavior. The height of the sample is fundamental for the correct alignment of the sample in the XRD equipment, so an offset of height generates an offset in the peak positions (equivalent of an offset in the lattice parameter and volume pairs obtained through the refinements). These variations indicate that the hysteresis observed is not intrinsic from the NWs behavior but a result of the centering to the sample. Another way to corroborate this fact is by analyzing the unit cell volume of the Au obtained by the sequential Rietveld fit present in figure 8.13 in the appendix 8.

To calculate the thermal expansion of the samples, the $\Delta V/V$ was plotted as a function of the temperature (figure 6.47), where several linear interpolations were performed.

Figure 6.48 presents the coefficient of thermal expansion, α_V, as a function of temperature for both samples. Some values encountered in the literature for bulk Fe and Co [86, 87], $Fe_{21}Co_{79}$ and $Fe_{31}Co_{69}$ [14] can be encountered in figure 8.14 in the appendix 8. The results obtained show little variation in α_V despite the linear interpolations. When compared with the bulk alloys, where the α_V is always higher than 35×10^{-6}, there is a clear decrease in the CTE. For the NWs, despite the not so optimal Rietveld fits, the α_V stays below the values of the bulk. For the NWs samples with stoichiometry of $Fe_{50}Co_{50}$, the overall α_V is around 10×10^{-6}, whereas for NWs samples with stoichiometry of $Fe_{10}Co_{90}$,

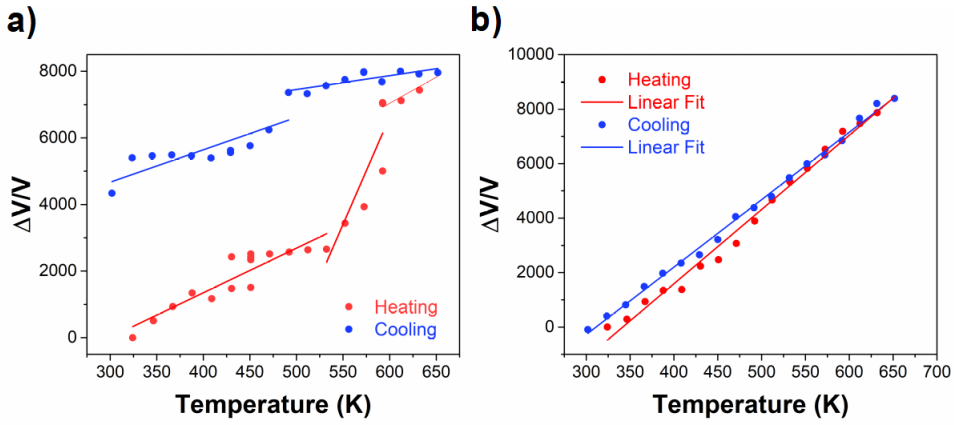


FIGURE 6.47: $\Delta V/V$ as a function of the temperature for the samples a) $Fe_{50}Co_{50}$ and b) $Fe_{10}Co_{90}$, with various linear interpolations.

the overall α_V is between 24.5×10^{-6} and 27.5×10^{-6}.

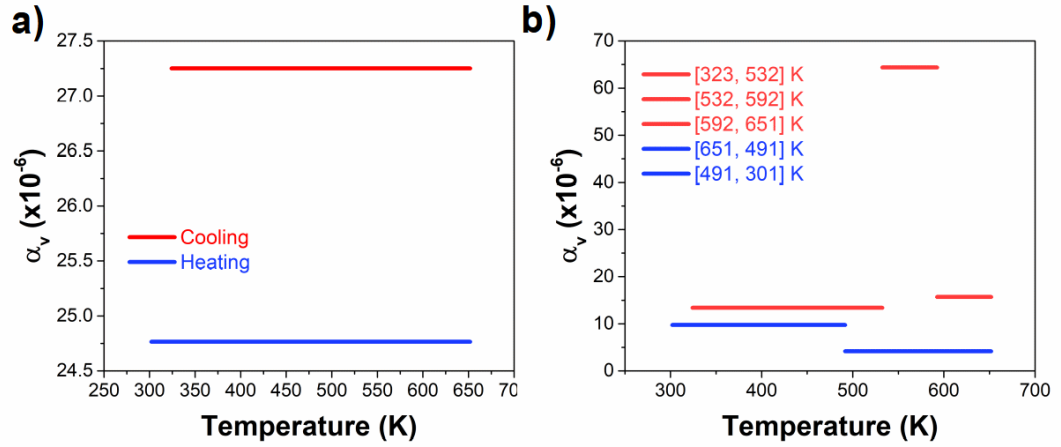


FIGURE 6.48: Thermal expansion coefficient as a function of the temperature obtained by differentiation of the various linear interpolations of $\Delta V/V$ for the samples a) $Fe_{50}Co_{50}$ and b) $Fe_{10}Co_{90}$.

With these results, one can conclude that the diminishing of the size of FeCo alloys can lower its CTE. Therefore, the customization of such parameter can be manipulated by the size of the material.

6.6 FeCo Based Co-catalyst for H_2 Green Generation

This section intends to expand the FeCo application on other technological topics, such as photocatalytic water splitting for solar H_2 generation. Photocatalytic water splitting and CO2 reduction are environmental methods that allow the storage and conversion of solar energy into chemical energy. It is very important to develop water oxidation catalysts

that are highly efficient under photochemical and electrochemical systems, stable, low-cost and eco-friendly. [69]

Metals like Fe, Co, Ni and their derivatives possess high catalytic activities in the energy conversion reactions, being considered promising substitutes of metals such as Pt [88]. Most of the FeCo catalysts used for hydrogen evolution reaction (HER) and oxygen evolution reaction (OER) are based on the combination of FeCo nanoparticles with other materials to improve photo performance. [88]. Nonetheless, Fe-Co bimetal oxide ($Fe_{1.1}Co_{1.9}O_4$) nanorods synthesized via coprecipitation have proven to be an efficient catalyst for water-splitting [69].

Herewith $Fe_{10}Co_{90}$ thin film was used as a co-catalyst for the photoelectrochemical process of water splitting. $Fe_{10}Co_{90}$ thin films were electrodeposited unto two hematite (α^- Fe_2O_3) thin films, the typical photoanode material of a photoelectrochemical cell. Two photoanodes samples were produced by depositing 150 and 300 nm of Fe on transparent conduction oxide (TCO) substrates by Ion Beam Deposition (IBD) and then annealed at 550 ºC during 2 h in air atmosphere. For the electrodeposition, it was used the FeCo solution for $Fe_{10}Co_{90}$ stoichiometry, at a V_{dep} = -1.8 V. The electrodeposition time was monitored based on the live time-analyses during the electrodeposition. Afterward, the samples were annealed at 550 ºC for 2 h in an air atmosphere.

To study the photoelectrochemical response of the prepared photoanodes (TCO/ hematite/ FeCo-oxide system), solar measurements were performed using a "cappuccino cell" and a three-electrode system. The typical measurements that evaluate the photoresponse are current-density (j) as a function of applied potential (V vs. RHE) curves (J-V). The measurements were performed under dark and simulated sunlight, AM 1.5 G and an electrolyte solution of 1.0 M NaOH (25 ºC, pH ¼ 13.3). [89]

Figure 6.49 a) shows the electrodeposition curves obtained for each sample. The FeCo film thicknesses were calculated with Faraday's Laws of Electrolysis (equation 3.10). Thicknesses of 22 and 37 nm were obtained for the samples with 150 and 300 nm, respectively. Figure 6.49 b) presents the solar measurements, where one can see that for the sample with 150 nm of Fe, the photocurrent increases from 0.17 to 0.28 mA cm_2 at 1.45V vs. RHE, which implies photoresponse an improvement of more than 60

This remarkable result proves that oxidized $Fe_{10}Co_{90}$ alloy is a great candidate to be used as a catalyst for the photoelectrochemical process of water splitting.

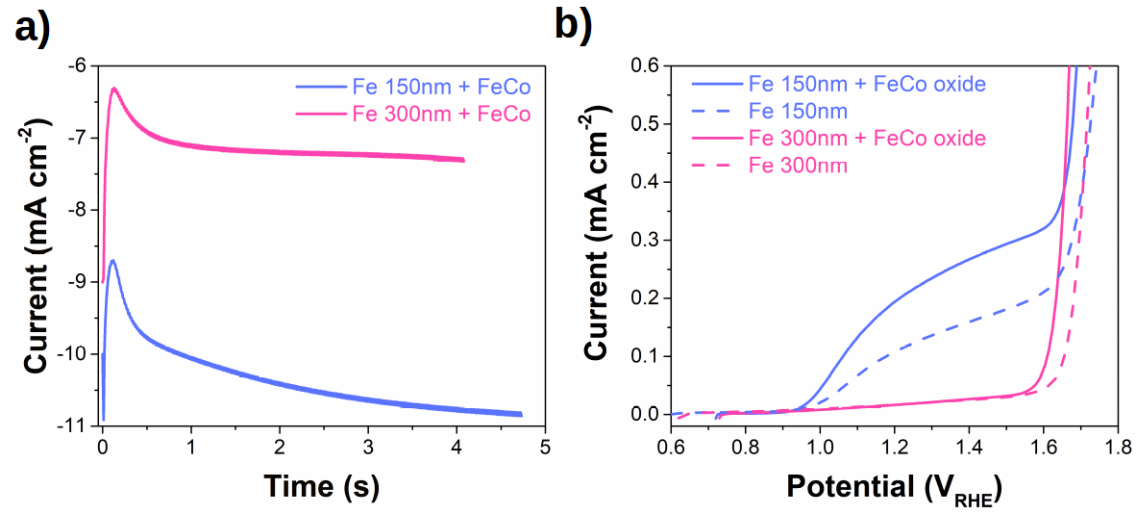


FIGURE 6.49: a) Electrodeposition curves of the $Fe_{10}Co_{90}$ thin films deposited in Fe thin films with thicknesses of 150 and 300 nm; b) solar measurements of current in function of the applied potential (vs. RHE) for both samples.

6.7 Customization of the Negative Thermal Expansion in $LaFe_{11.9}Mn_{0.27}Si_{1.29}H_x$

A seen previously in chapter 2, the $La(Fe,Si)_{13}$ family is known for their magnetocaloric applications as well as for their NTE. The magnetic transition causes their large volume contraction (at T_c) from a low-temperature ferromagnetic (FM) phase to a high temperature paramagnetic (PM) phase, meaning that the origin of the NTE in this material derives from the magnetovolume coupling. In addiction, the crystal structure, more specifically the Fe-Fe interatomic distance, is correlated with the material's magnetic properties. [29] The hydrogenation of the $La(Fe,Si)_{13}$ compounds has been proven to increase the T_c. [90]. In addition, the Mn element showed to be an effective way to also change T_c [91]. This way, the integration of Mn and H into the equation allows the shifting of the T_c to temperatures closer to room temperature. With the tuning of T_c there is also a tuning on the temperature window where the NTE exits. Since there is also the fact that several materials have shown changes in TE when their size is modified. Herewith, it is intended to tune the NTE of in the $La(FeSi)_{13}$ material by introducing a chemical modification, such as the Mn element, and by altering its particle size.

Samples of $LaFe_{11.9}Mn_{0.27}Si_{1.29}H_x$, fabricated in TU Darmstadt (Germany), by arc-melting were ball milled (BM) during different times, 14, 30, 45, 90, and 180 minutes. The particle sizes obtained were, on average, 134±89, 7±4, 3±3, 3±3, 0.6±0.5 and 0.5±0.4

μm, for the original sample and the respective BM times. Figure 6.50 shows the SEM images of all the samples, including the original one. Various particle sizes were obtained by measuring the SEM images of each sample. Then the histograms of the particle size distribution (figure 8.6 appendix 8) were fitted with a normal distribution to obtain the average size and its variation.

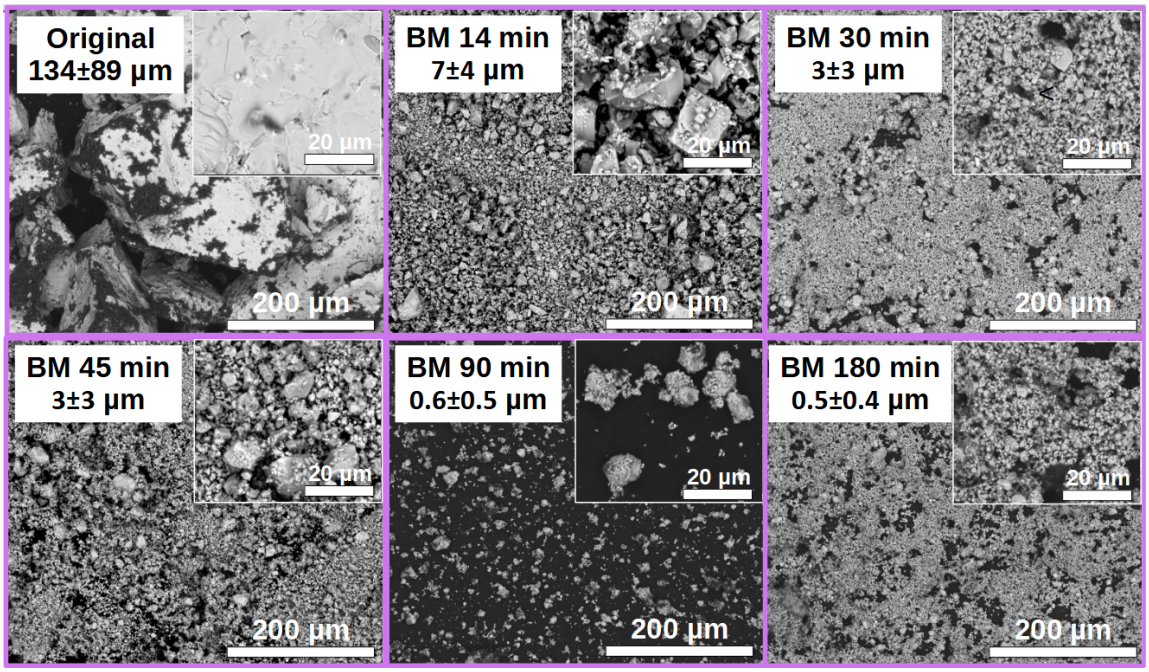


FIGURE 6.50: SEM images of the $LaFe_{11.9}Mn_{0.27}Si_{1.29}H_x$ samples, the original and the ball milled for different times.

Since the NTE behavior of the $LaFe_{11.9}Mn_{0.27}Si_{1.29}H_x$ family is strongly correlated with its magnetic transition, magnetic measurements were also performed. Figure 6.51 shows the temperature dependence of the normalized magnetization (M(T)) with an applied magnetic field of 1000 Oe in cooling under FC process for the samples original and BM for 14, 45, 90 and 180 minutes. One can observe that for all measured samples, their magnetization exhibits an increase with decreasing temperature. This occurs most drastically around the T_c and corresponds to the transition PM-FM in cooling. The M(T) of the original sample presents a sharp transition at $\sim$ 305 K, remaining constant with a further decrease of temperature. In comparison, the M(T) curves of the samples that suffered BM present increasingly smoothened transition with increasing BM time. It is impossible for samples with higher BM to observe the full transition due to equipment limitations. This indicates that the FM-PM transition becomes more gradual with the decrease in particle size, giving rise to a broader temperature transition window. It is also worth noticing

that despite the difference in mean particle size being small, the M(T) curves for sample BM180 exhibit a broader profile (than for BM90) (figure 6.50). This occurs because the BM not only decreases the particle size but also induces strain in the particles. The inset of the figure 6.51 presents the T_c variation with the BM time, due to incomplete M(T) curves and the lack of high resolution, one can consider the trend to be somewhat linear.

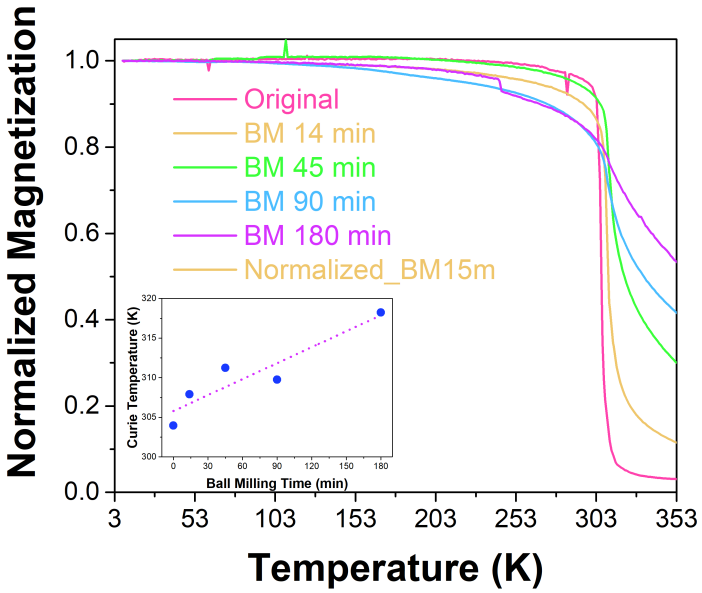


FIGURE 6.51: Normalized M(T) curves for the samples $LaFe_{11.9}Mn_{0.27}Si_{1.29}H_x$, original and ball milled for 14, 45, 90 and 180 minutes, obtained under field-cooled. The inset represents the T_c as a function of the ball milling time.

The samples were structurally characterized using a HRSXRD, where it is possible to obtain high precision XRD patterns, enabling the estimation of several crystallographic parameters with high accuracy. By refining the XRD patterns obtained with a Rietveld method [80], one can determine the unit cell parameters and volume and nearly all desired interatomic distances as a function of temperature. One example of the XRD patterns analyzed is presented in figure 6.52, where the XRD patterns obtained during the cooling of the sample (BM180) are present. Figure 8.7 in the appendix 8 contains one example of the Rietveld refinements performed, corresponding to the fit of the pattern acquired for this sample at temperature 300 K.

By performing sequential Rietveld refinements in the XRD patterns obtained, one was able to present the unit cell volumes as a function of the temperature for all samples (figure 8.8 in the appendix 8). The values obtained for this quantity are as expected, corroborating results from the literature [30]. This method of data analysis was possible because,

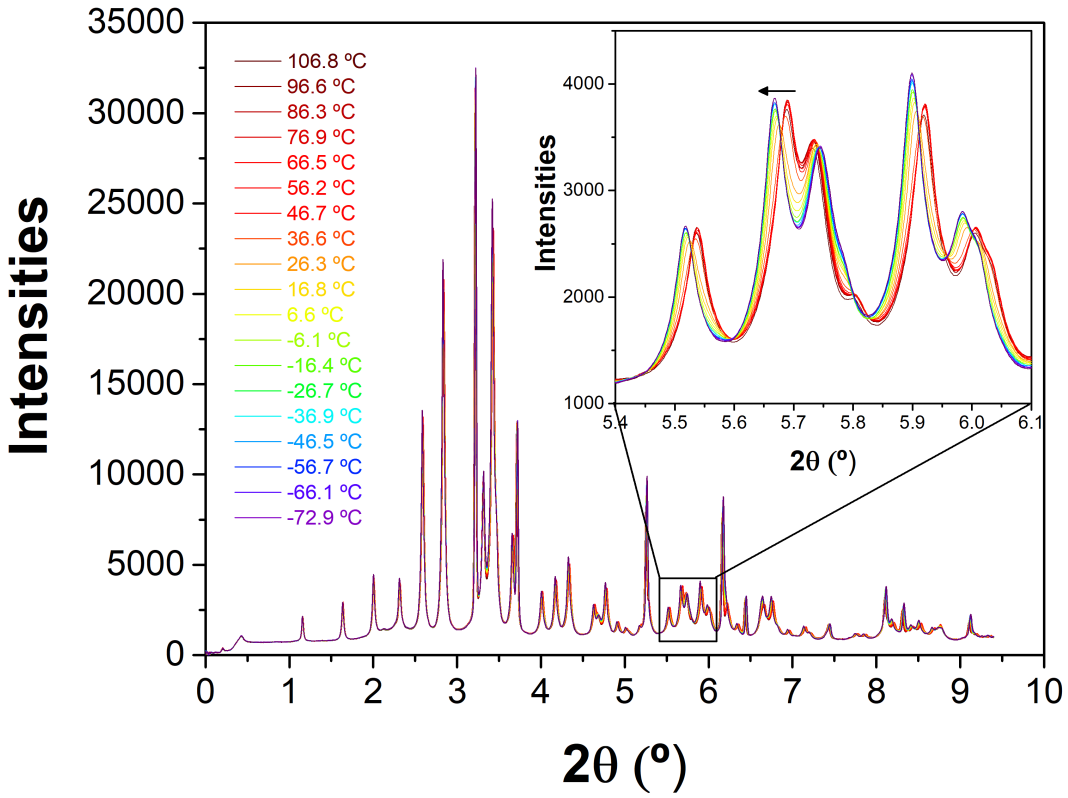


FIGURE 6.52: XRD pattern acquired for the sample of $LaFe_{11.9}Mn_{0.27}Si_{1.29}H_x$ ball milled for 180 minutes in cooling.

despite the magnet volume effect, the crystal structure undergoes a volume contraction without altering its space group, which is a cubic structure with space group *Fm3c* 6.5.

The normalized unit cell volumes can be found in figure 6.53 a) and b). From this image, one can observe that the unit cell volume of all samples presents a decrease in the temperature range from $\sim$ 233 to $\sim$ 333 K, where the unit cell volume of the original sample shows a more abrupt contraction. As the BM time increases, there is also a decrease in the sharpness of the transition, as the sample BM180 has a smoother transition. This profile transition is identical to the one observed for the magnetic transitions. Herewith, two distinct measurements present a similar behavior evolution which comes to confirm the high magnetovolume coupling. Additionally, for all samples, the volume contraction starts around the same temperature, $\sim$ 233 K. However, the transition tends to extend with increasing BM time, which means that the BM time enlarges the temperature window where the contraction occurs. The original samples present contraction until $\sim$ 323 K, whereas the sample BM180 shows contraction until $\sim$ 343 K. This can be seen in the plots present in figure 6.53 c) and d), where the derivatives of the unit cell volumes are

shown. The enlargement of the derivative (dV/dt) peak confirms that the BM broadens the temperature window of the volume contraction. Besides, the fact that the peak value of the derivatives decreases with the BM time implies a less abrupt contraction, i.e., a smaller CTE value (in magnitude). One can also observe that after the volume contraction of all samples, the unit cell starts to increase with temperature, i.e., positive/conventional thermal expansion, where a tendency of lower BM time higher volume expansion is seen (higher positive CTE). In addition, as mentioned before, because the BM time induces strain in the particles, the unit cell volumes as a function of the temperature for the samples BM30 and BM45 present different behaviors despite possessing very similar particle sizes (figure 6.50).

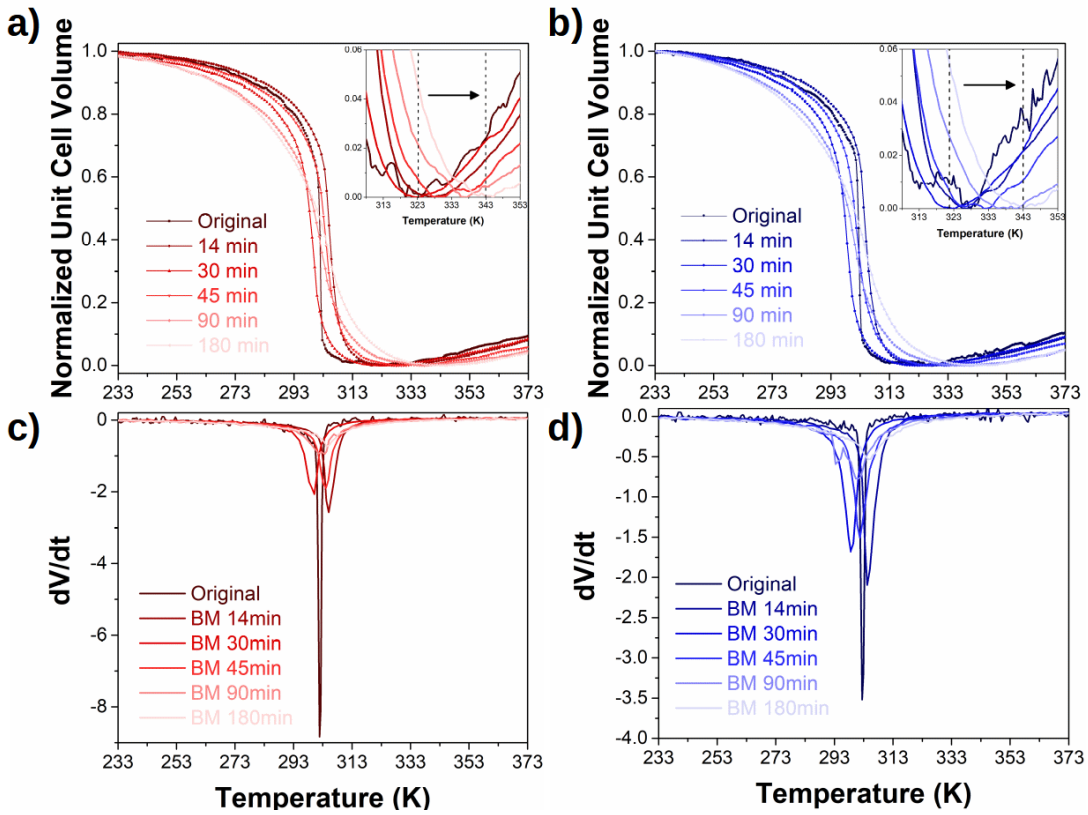


FIGURE 6.53: Normalized unit cell volumes in the temperature range from -40 to 100 ºC, obtained through sequential Rietveld refinements for all $LaFe_{11.9}Mn_{0.27}Si_{1.29}H_x$ samples, in a) heating and in b) cooling and the c) d) derivatives in order of temperature, respectively.

Figure 6.54 shows the full width at half maximum (FWHM) of the derivatives of the unit cell volumes and magnetization as a function of the BM time as well as the particle size. With this graphic representation, one can observe a linear tendency between the widening of the derivative peak both for the unit cell volume and magnetization data with increasing BM time where higher BM times lead to larger temperature ranges of

FWHM. On the contrary, the particle size was revealed to decrease with the BM time as expected and seen before. When comparing the original sample with the BM14, a great difference in size is noticeable. However, despite the impact that other BM times had on the samples size being not so extensive, BM also induces strain which turns to be decisive on the extension of the FWHM.

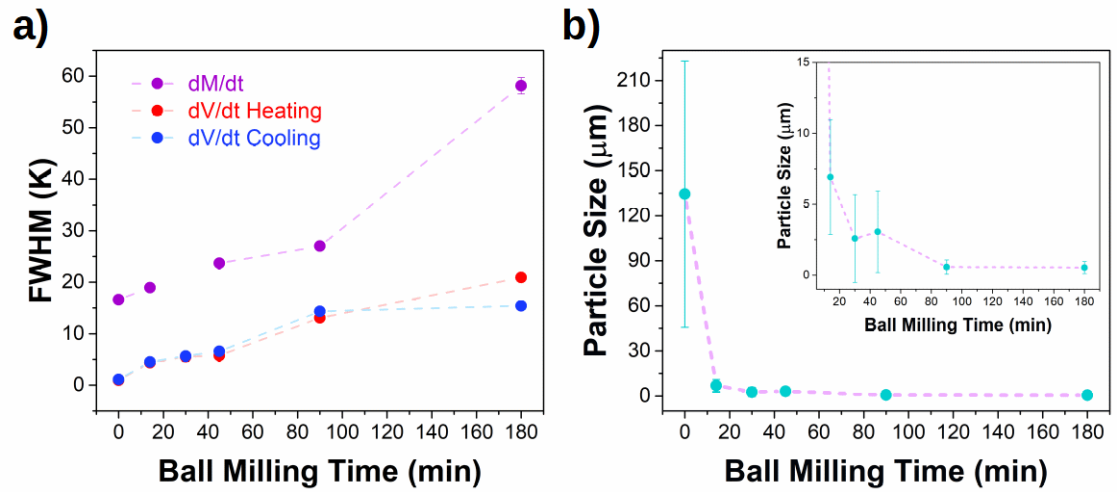


FIGURE 6.54: a) Full width at half maximum (FWHM) of the derivatives of the unit cell volume in heating (red dots) and in cooling (blue dots), and the magnetization (purple dots) as a function of the ball milling time, comparing with b) the particle size, for all samples of $LaFe_{11.9}Mn_{0.27}Si_{1.29}H_x$.

In order to obtain the CTE of the diverse samples, the expression 2.2 was used. The results obtained on heating and cooling are presented in the figure 6.55. The color windows represent the range where the volume contraction was observed previously in the unit cell volume as a function of the temperature (figure 6.53 a) and b)). The lines sidewards represent the original NTE window of the $LaFe_{11.9}Mn_{0.27}Si_{1.29}H_x$ without BM. In comparison, the crossed lines represent the additional temperature window where one could extend the NTE in this material by size tuning and inclusion of the chemical element Mn. With this, the tuning of the NTE by size-reduction was proven.

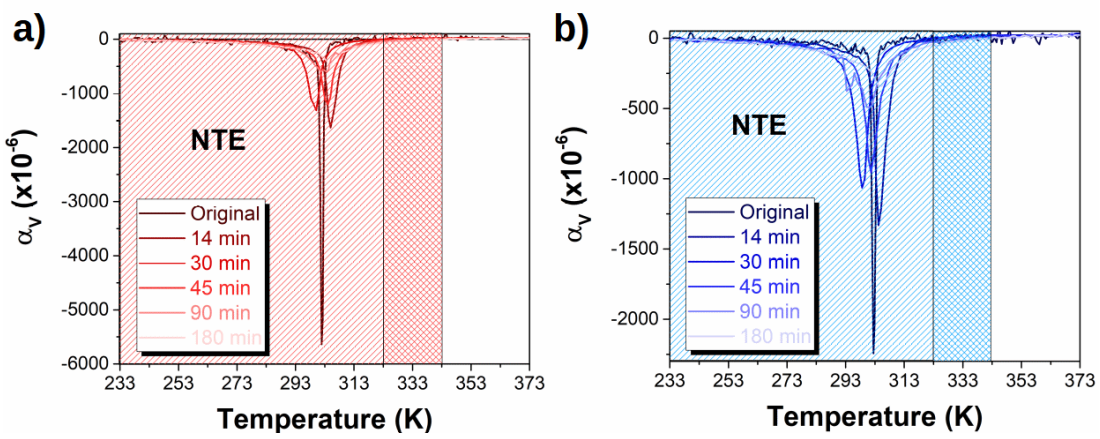


FIGURE 6.55: Thermal expansion coefficient (CTE) in function of the temperature for all samples of $LaFe_{11.9}Mn_{0.27}Si_{1.29}H_x$, obtained on a) heating and on b) cooling.

Chapter 7

Conclusions and future work

In this final chapter is divided in two parts. First, some general conclusions of this work are summarized, as the throughout each part of this dissertation the main conclusions are already synthesized. And secondly, the part that will have more emphasized, the future work.

7.1 Conclusion

One of the main goals of this dissertation was to synthesized FeCo NWs with different stoichiometries in order to characterize their TE. Due to a lack of literature in the fabrication of these NWs with different stoichiometries, we were obligated to start from the beginning by studying electrodeposition parameters to obtain the desired NWs. This approach revealed to be challenging, culminating in an intensive study to achieve optimal electrodeposition parameters for the fabrication of the NWs with vary stoichiometries. This also resulted in the adaptation of the Faraday's Law of Electrolysis for nanoporous substrates, a result that we could not found in the literature. Both the study and the adapted law were a huge step in our work, enabling the fabrication of NWs samples that have the exact expected length.

As for the thermal expansion in the FeCo NWs, the results obtained are not the more accurate but give a rough idea of the CTE for these structures. Where, one can indeed state that by reducing the size from bulk to 1D nanostructures the CTE of the FeCo alloys decreases. Therefore, proving that this nanostructures are strong candidates to have their thermal expansion customized

The thermal expansion of $LaFe_{11.9}Mn_{0.27}Si_{1.29}H_x$ was a methodic work. Where by combining several different literature results we were able to tune the already existent NTE of this material. It was showed that by decreasing the particles size and inducing strain, the magnetic transition is elongated. Which also results in the broading of the temperature window where the NTE appears while also bringing the CTE closer to zero. Despite diminishing the NTE, the fact that the NTE occurs in a larger temperature window where no extreme changes happen, is a good thing. Because lower particle sizes are easier mixed with other compounds allowing a more varied range of applications.

7.2 Future Work

Throughout this work there were a lot of things than could have been improved.

Starting with the bulk samples, we still intend to measure the magnetic properties of the sample $Fe_{10}Co_{90}$ at 300 K and also to complete the measurements at 5 K.

As for the first thin films fabricated, with stoichiometries of $Fe_{20}Co_{80}$, their pealing from the Cu substrate could enhance the XRD diffractogram enabling a more accurate structure analysis. Also the analysis of the electrodeposition curves with the Palomar-Pardavé et al. equations presented in chapter 3, should allow a better understanding of the nucleation and growth processes for the solution used, providing information such as the constant of hydrogen evolution reaction, the nucleation rate and the surface active site number [65]. This can also be extented to the results obtained with the thin films fabricated using the solution with different concentrations of Fe and Co.

For the NWs fabricated and characterized in the section (6.5), there is still a lack of understanding in the magnetic behaviors obtained. Being this a still ongoing work, we intent to be able to eventually explain the results obtained. About the thermal expansion characterization, better data needs to be collected, for example using a HRSXRD as used for the $LaFe_{11.9}Mn_{0.27}Si_{1.29}H_x$, as this would allow fantastic results. Still on the topic of the thermal expansion of FeCo alloys, we intend to characterize this property for the bulk alloys. And future work includes the fabrication of FeCo alloys with other features to determine their CTE. For example, fabricate microparticles these alloys by laser ablation and also reduce the size of the bulks by ball milling.

On other topic, the oxidized FeCo thin used as a photocatalytic water splitting for solar H_2 generation, revealed to be a fantastic candidate for this application, as we expect to extend this work to that technology.

Chapter 8

Appendix A

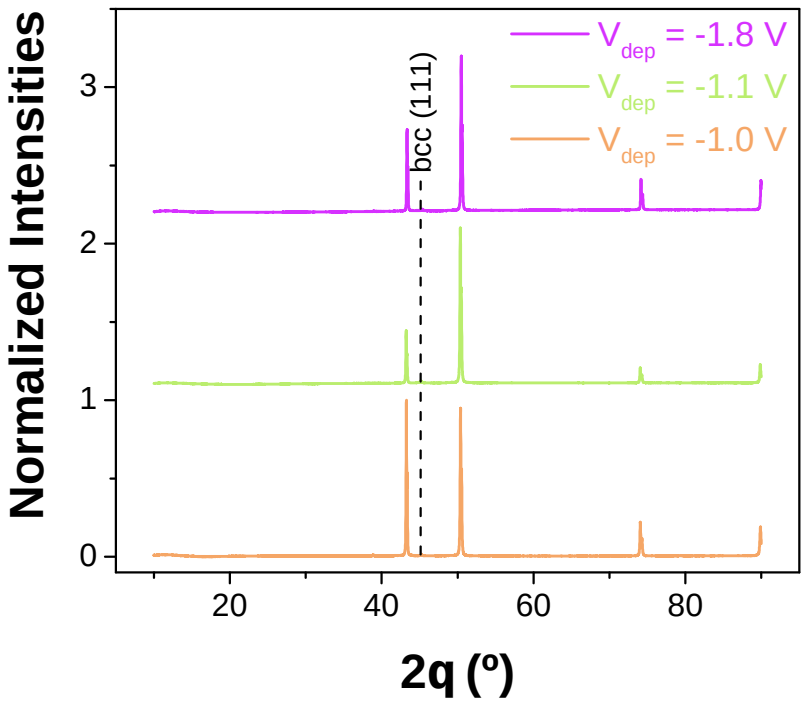


FIGURE 8.1: Full XDR diffraction patterns of the thin films electrodeposited with applied potentials of -1.0, -1.1 and –1.8 (V vs. Ag/AgCl).

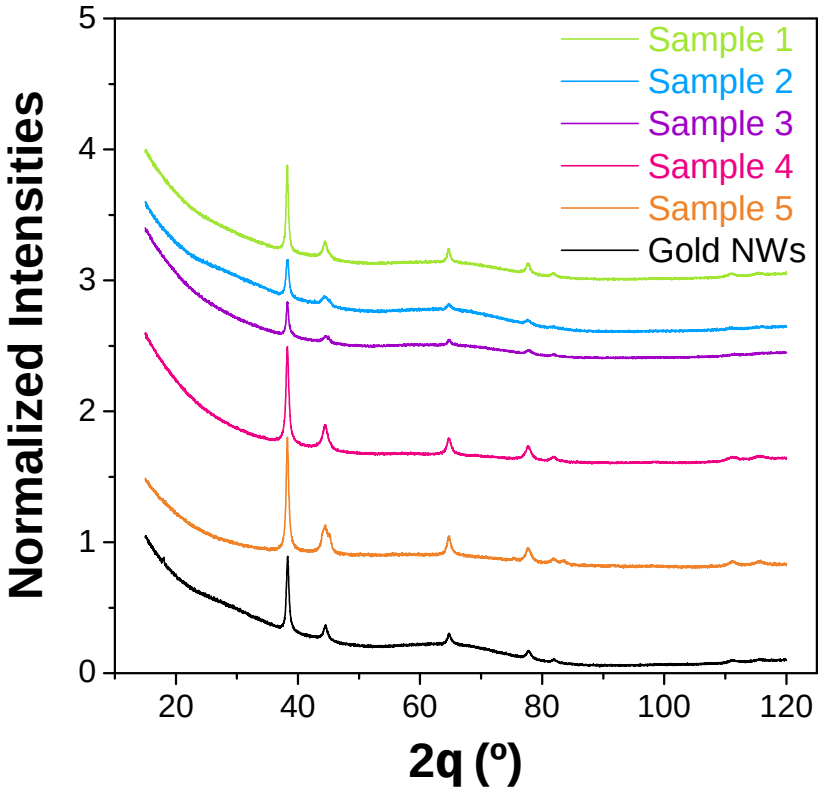


FIGURE 8.2: XDR diffraction patterns of the NWs samples 1, 2, 3, 4 and 5 fabricated using the test solution and a sample of only sputtered Au and Au NWs for comparison.

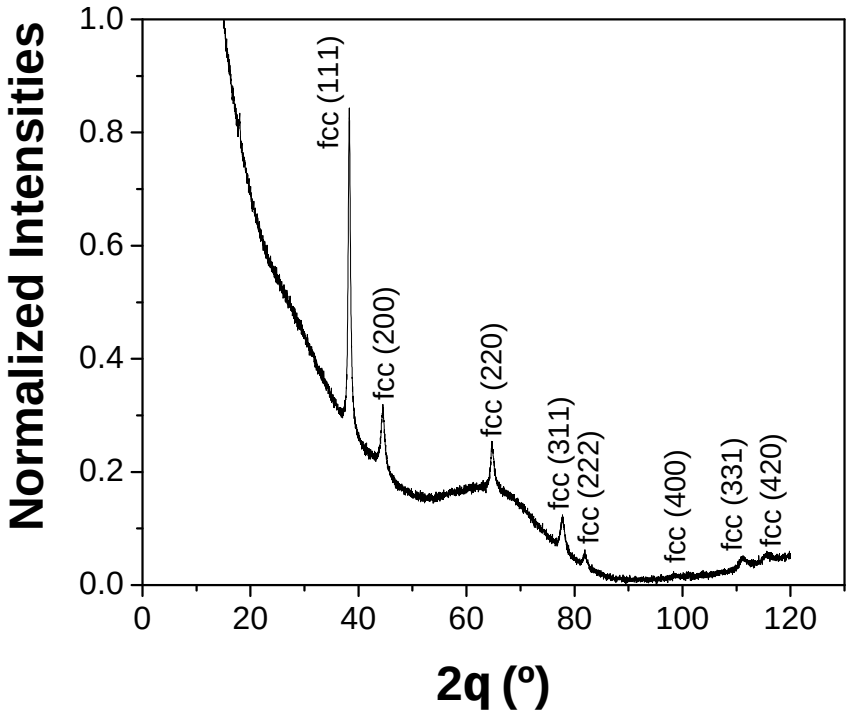


FIGURE 8.3: XDR diffraction patterns of a sample with a thin film deposited through sputtering and 6 min of Au electrodeposition at -1.0 (V vs. Ag/AgCl).

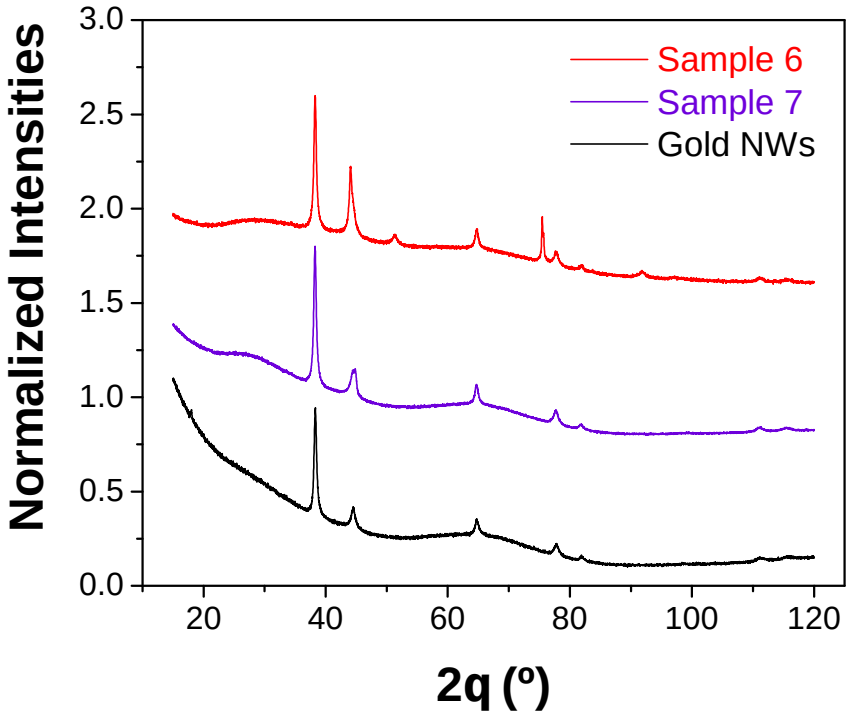


FIGURE 8.4: XDR diffraction patterns of the NWs samples 6 and 7 fabricated using solutions with different concentrations of Co and Fe. and a sample of only sputtered Au and Au NWs for comparison.

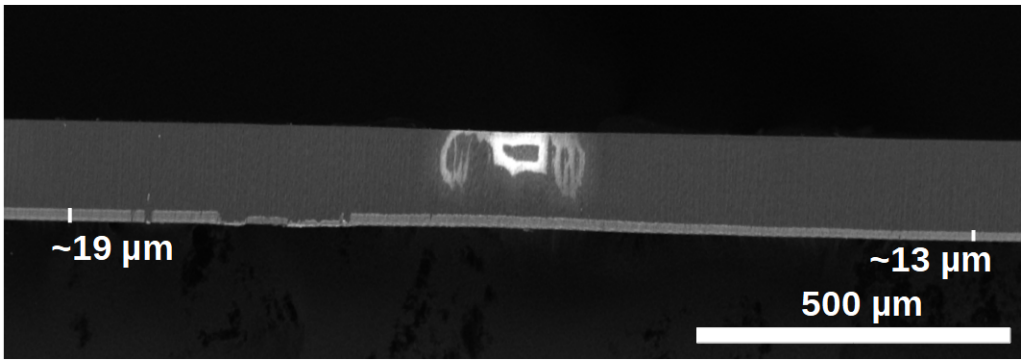


FIGURE 8.5: SEM image, using backscatered electrons, of the multisegmented Au/FeCo NWs electrodeposited using the solution $Fe_{10}Co_{90}$.

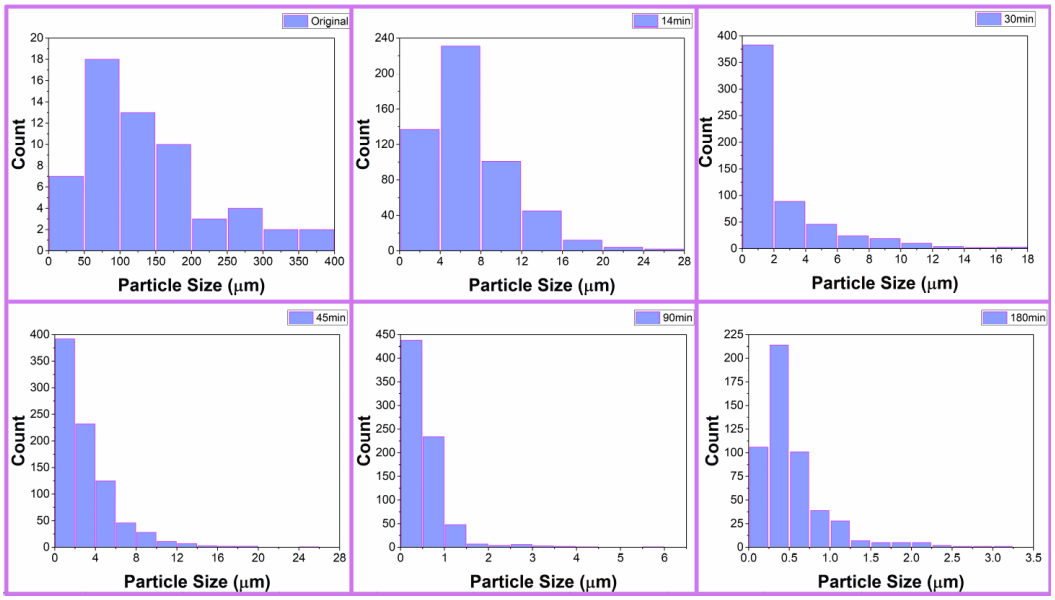


FIGURE 8.6: Histograms with the particle size distribution of each $LaFe_{11.9}Mn_{0.27}Si_{1.29}H_x$ samples.

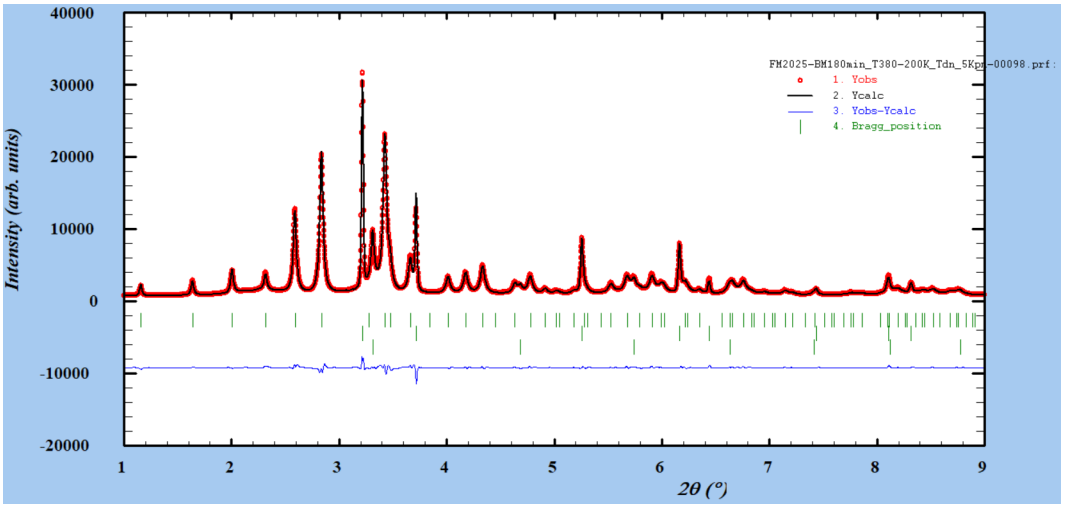


FIGURE 8.7: XRD pattern (in red) and Rietveld refinement (in black) for the sample of $LaFe_{11.9}Mn_{0.27}Si_{1.29}H_x$ ball milled for 180 min, at temperature 26.3 K.

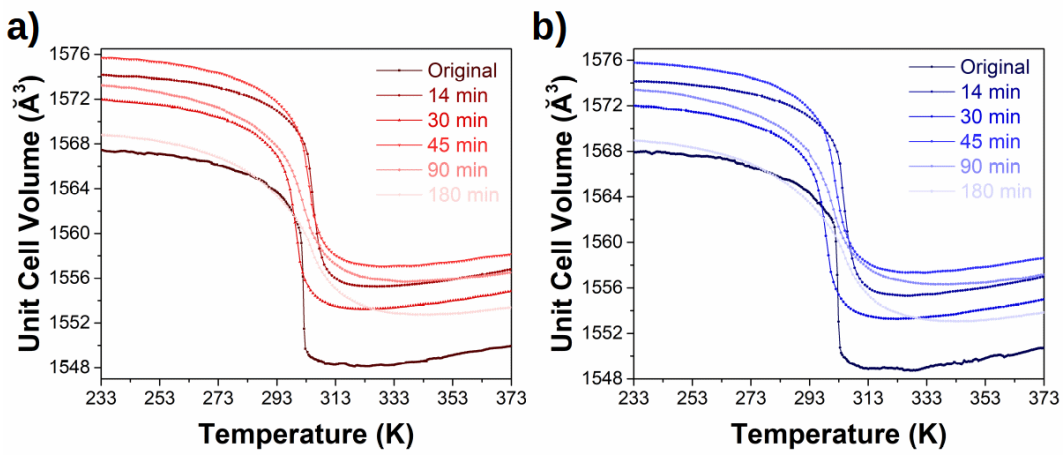


FIGURE 8.8: Unit cell volumes in the temperature range from -40 to 100 ºC, obtained through sequential Rietveld refinements for all $LaFe_{11.9}Mn_{0.27}Si_{1.29}H_x$ samples, in a) heating and in b) cooling

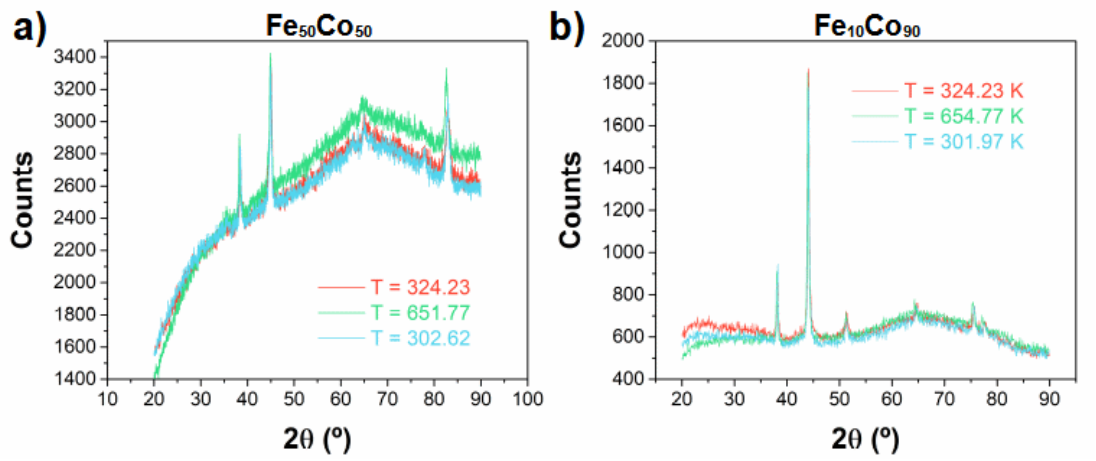


FIGURE 8.9: XRD patterns of the samples with stoichiometries of $Fe_{50}Co_{50}$ and $Fe_{10}Co_{90}$, corresponding to the first measurement, the measurement at the highest temperature, and the last measurement.

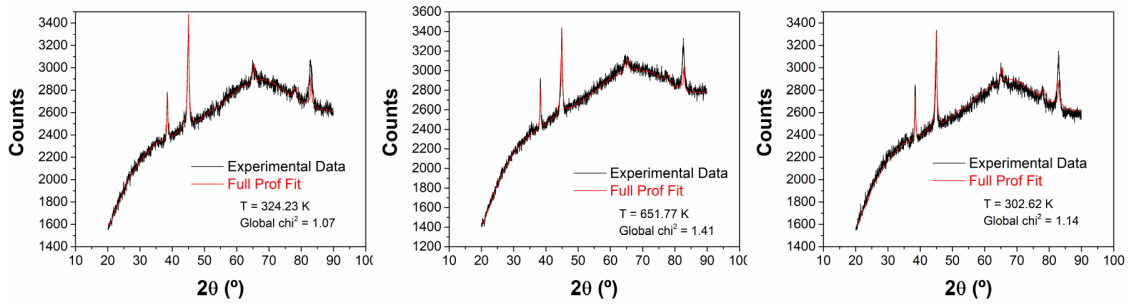


FIGURE 8.10: Rietveld fits examples obtained for the sample with stoichiometry of $Fe_{50}Co_{50}$ at different temperatures. XRD patterns correspond to the first measurement, the measurement at the highest temperature, and the last measurement.

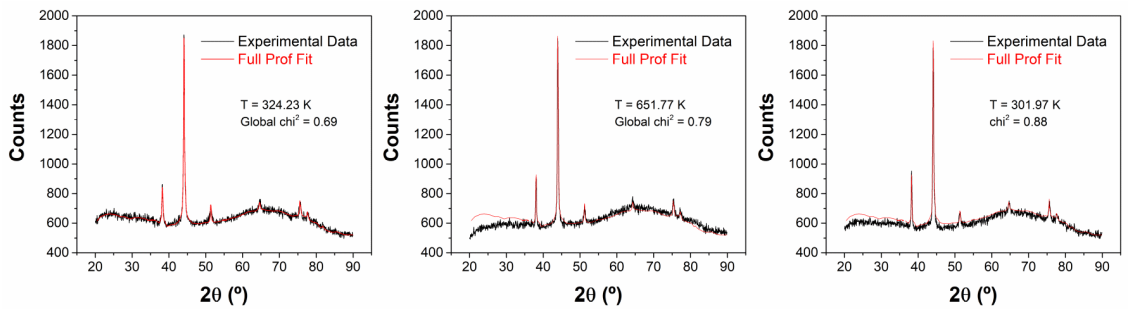


FIGURE 8.11: Rietveld fits examples obtained for the sample with stoichiometry of $Fe_{10}Co_{90}$ at different temperatures. XRD patterns correspond to the first measurement, the measurement at the highest temperature, and the last measurement.

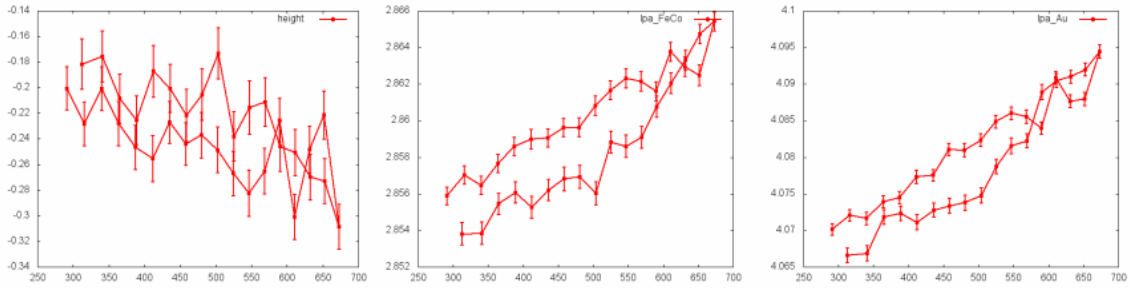


FIGURE 8.12: Preliminary results obtained for the sample with stoichiometry $Fe_{50}Co_{50}$ with Rietveld fits. These include the height of the sample, lattice parameter of the FeCo and the lattice parameters of the Au.

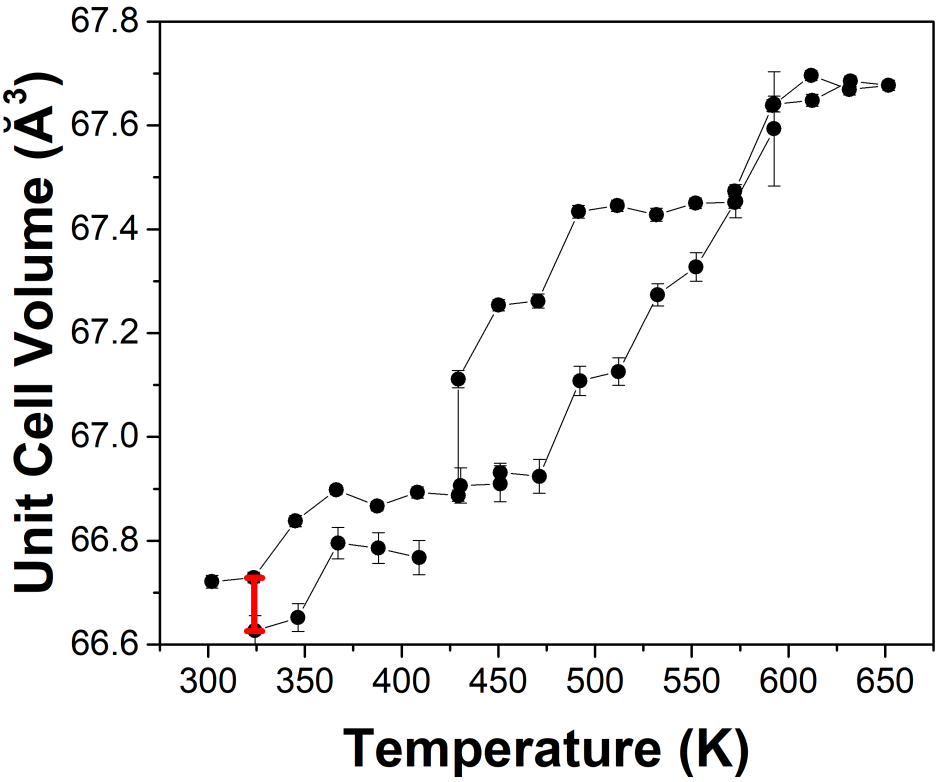


FIGURE 8.13: Unit cell volume of the Au obtained from the sequential Rietveld fits of the sample with stoichiometry $Fe_{50}Co_{50}$.

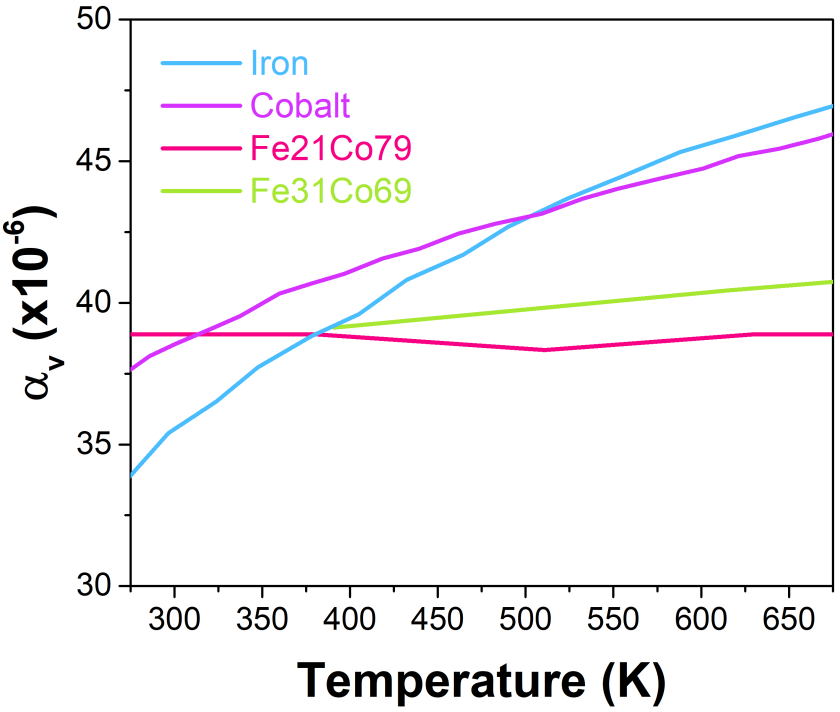


FIGURE 8.14: Bulk FeCo alloys thermal expansion from the literature such as for Fe and Co [86, 87], and $Fe_{21}Co_{79}$ and $Fe_{31}Co_{69}$ [14].

Bibliography

[1] K. Takenaka, "Progress of research in negative thermal expansion materials: Paradigm shift in the control of thermal expansion," *Frontiers in Chemistry*, vol. 6, 07 2018. [Cited on pages xv, 1, 6, 7, 8, 9, 10, 12, 13, 14, and 15.]

[2] J. Attfield, "Mechanisms and materials for nte," *Frontiers in Chemistry*, vol. 6, 08 2018. [Cited on pages xv, 1, 5, 6, 7, 8, 12, 13, 15, and 16.]

[3] J. Grima, V. Zammit, and R. Gatt, "Negative thermal expansion," *Xjenza*, vol. 11, 01 2006. [Cited on page 1.]

[4] J. Chen, L. Hu, J. Deng, and X. Xing, "Negative thermal expansion in functional materials: Controllable thermal expansion by chemical modifications," *Chemical Society reviews*, vol. 44, 04 2015. [Cited on pages xv, 1, 7, 9, 10, 11, 13, 14, and 16.]

[5] E. F. Wasserman, "Chapter 3 invar: Moment-volume instabilities in transition metals and alloys," *Handbook of Ferromagnetic Materials*, vol. 5, pp. 237–322, 1990. [Cited on pages 1, 2, 9, 10, and 31.]

[6] T. Mary, J. Evans, T. Vogt, and A. Sleight, "Negative thermal expansion from 0.3 to 1050 kelvin in ZrW_2O_8," *Science*, vol. 272, pp. 90–92, 04 1996. [Cited on pages 2 and 9.]

[7] Q. Li, H. Zhu, L. Hu, J. Chen, and X. Xing, "Negative thermal expansion in nanosolids," *Accounts of Chemical Research*, vol. 52, 08 2019. [Cited on pages 2, 15, and 16.]

[8] A. Popova, "Synthesis and characterization of iron-cobalt nanoparticles," *Journal of Physics Conference Series*, vol. 345, pp. 2030–, 02 2012. [Cited on pages 2 and 31.]

[9] D. Hunter, W. Osborn, K. Wang, N. Kazantseva, J. Hattrick-Simpers, R. Suchoski, R. Takahashi, M. Young, A. Mehta, L. Bendersky, S. Lofland, M. Wuttig, and

I. Takeuchi, "Giant magnetostriction in annealed $Co_{1-x}Fe_x$ thin-films," *Nature communications*, vol. 2, p. 518, 11 2011. [Cited on pages xvi, 2, 31, 32, and 33.]

[10] Y. Han, H. Wang, T. Zhang, Y. He, J. M. D. Coey, and C. Jiang, "Tailoring the heterogeneous magnetostriction in Fe–Co alloys," *Journal of Alloys and Compounds*, vol. 699, pp. 200–209, 03 2017. [Cited on pages xvi, 2, 32, 33, 34, 35, and 58.]

[11] S.-i. Yamaura, T. Nakajima, T. Satoh, T. Ebata, and Y. Furuya, "Magnetostriction of heavily deformed FeFe binary alloys prepared by forging and cold rolling," *Materials Science and Engineering: B*, vol. 193, 12 2014. [Cited on pages xvi, 33, 34, 58, and 62.]

[12] R. Zhang, C. Zhou, K. Chen, K. Cao, Y. Zhang, F. Tian, A. Murtaza, S. Yang, and X. Song, "Near-zero magnetostriction in magnetostrictive FeCo alloys," *Scripta Materialia*, vol. 203, p. 114043, 2021. [Cited on pages 2, 33, 57, and 65.]

[13] Y. Song, N. Shi, S. Deng, X. Xing, and J. Chen, "Negative thermal expansion in magnetic materials," *Progress in Materials Science*, vol. 121, p. 100835, 2021. [Cited on pages 2, 10, 11, and 16.]

[14] M. Takahashi, F. Ono, and K. Takakura, "The invar characteristics on CoCo alloys," *AIP Conference Proceedings*, vol. 29, no. 1, pp. 562–563, 1976. [Online]. Available: https://aip.scitation.org/doi/abs/10.1063/1.30451 [Cited on pages xvi, xx, 2, 36, 97, and 116.]

[15] C. Sousa, D. Leitao, M. Proenca, J. Ventura, A. Pereira, and J. Araujo, "Nanoporous alumina as templates for multifunctional applications," *Applied Physics Review*, vol. 1, p. 031102, 01 2014. [Cited on pages xv, xvi, 2, 19, 20, 21, 22, 23, 26, and 27.]

[16] N. Wang, Y. Cai, and R. Zhang, "Growth of nanowires," *Materials Science and Engineering: R: Reports*, vol. 60, pp. 1–51, 2008. [Cited on pages 2 and 19.]

[17] W. Miller, C. Smith, D. Mackenzie, and K. Evans, "Negative thermal expansion: A review," *Journal of Materials Science*, vol. 44, pp. 5441–5451, 10 2009. [Cited on pages xv, 6, 7, 8, and 9.]

[18] F. Gillery and E. Bush, "Thermal contraction of β-eucryptite ($Li_2O-Al_2O_3-2\,SiO_2$) by x-ray and dilatometer methods," *Journal of the American Ceramic Society*, vol. 42, pp. 175 – 177, 06 1959. [Cited on page 8.]

[19] H. Schulz, "Thermal expansion of beta eucryptite," *Journal of the American Ceramic Society*, vol. 57, pp. 313 – 318, 06 1974. [Cited on page 8.]

[20] J. S. O. Evans, T. A. Mary, and A. W. Sleight, "Negative thermal expansion in a large molybdate and tungstate family," *IEEE Journal of Solid-state Circuits*, vol. 133, pp. 580–583, 1997. [Cited on page 9.]

[21] A. Pryde, K. Hammonds, M. Dove, V. Heine, J. Gale, and M. Warren, "Origin of the negative thermal expansion in ZrW_2O_8 and ZrV_2O_7," *Journal of Physics: Condensed Matter*, vol. 8, no. 50, pp. 10 973–10 982, Dec. 1996. [Cited on page 9.]

[22] A. Phillips, A. Goodwin, G. Halder, P. Southon, and C. Kepert, "Nanoporosity and exceptional negative thermal expansion in single-network cadmium cyanide," *Angewandte Chemie (International ed. in English)*, vol. 47, pp. 1396–9, 02 2008. [Cited on page 9.]

[23] G. Shirane and A. Takeda, "Phase transitions in solid solutions of $PbZrO_3$ and $PbTiO_3$ (i) small concentrations of $PbTiO_3$," *Journal of the Physical Society of Japan*, vol. 7, no. 1, pp. 5–11, 1952. [Cited on page 9.]

[24] K. Takenaka and H. Takagi, "Giant negative thermal expansion in ge-doped anti-perovskite manganese nitrides," *Applied Physics Letters*, vol. 87, pp. 261 902–261 902, 12 2005. [Cited on pages 9, 10, and 11.]

[25] R. J. Weiss, "The origin of the invar effect," *Proceedings of the Physical Society*, vol. 82, no. 2, pp. 281–288, aug 1963. [Online]. Available: https://doi.org/10.1088/0370-1328/82/2/314 [Cited on page 10.]

[26] R. Huang, Y. Liu, W. Fan, J. Tan, F. Xiao, L. Qian, and L. Li, "Giant negative thermal expansion in $NaZn_{13}$-type $La(Fe, Si, Co)_{13}$ compounds," *Journal of the American Chemical Society*, vol. 135, 07 2013. [Cited on pages xv, 10, 11, and 12.]

[27] C. Wang, Y. Sun, Y. Wen, L. Chu, and M. Nie, "Investigation of lattice contraction in mn(3)xn(x=zn, cu, sn)," *Materials Science Forum - MATER SCI FORUM*, vol. 638-642, pp. 2195–2200, 01 2010. [Cited on page 11.]

[28] A. Fujita, S. Fujieda, K. Fukamichi, H. Mitamura, and T. Goto, "Itinerant-electron metamagnetic transition and large magnetovolume effects in $La(Fe_xSi_{1-x})_{13}$

compounds," *Phys. Rev. B*, vol. 65, p. 014410, Nov 2001. [Online]. Available: https://link.aps.org/doi/10.1103/PhysRevB.65.014410 [Cited on page 11.]

[29] S. Li, R. Huang, Y. Zhao, W. Li, W. Wang, C. Huang, P. Gong, Z. Lin, and L. Li, "Broad negative thermal expansion operation-temperature window achieved by adjusting FeFe magnetic exchange coupling in $La(Fe,Si)_{13}$ compounds," *Inorganic chemistry*, vol. 54, 07 2015. [Cited on pages 11 and 100.]

[30] L. Jia, J. Sun, H. Zhang, F. Hu, C. Dong, and B. Shen, "Magnetovolume effect in intermetallics $LaFe_{13x}Si_x$," *Journal of Physics: Condensed Matter*, vol. 18, p. 9999, 10 2006. [Cited on pages 11 and 102.]

[31] X. Xing, J. Deng, J.-C. Chen, and G. Liu, "Novel thermal expansion of lead titanate," *Rare Metals*, vol. 22, pp. 294–297, 12 2003. [Cited on page 13.]

[32] J. Chen, X. Xing, R. Yu, and G. Liu, "Thermal expansion properties of lanthanum-substituted lead titanate ceramics," *Journal of the American Ceramic Society*, vol. 88, pp. 1356 – 1358, 04 2005. [Cited on page 13.]

[33] J. Forrester, E. Kisi, K. Knight, and C. Howard, "Rhombohedral to cubic phase transition in the relaxor ferroelectric PZN," *Journal of Physics-condensed Matter - J PHYS-CONDENS MATTER*, vol. 18, 05 2006. [Cited on page 13.]

[34] J. Chen, X. Xing, G. Liu, J. Li, and Y. Liu, "Structure and negative thermal expansion in the pbtio3–bifeo3 system," *Applied Physics Letters*, vol. 89, pp. 101 914 – 101 914, 10 2006. [Cited on page 13.]

[35] J. L. Chen, X. Xing, C. Sun, P. Hu, R. Yu, X. Wang, and L. Li, "Zero thermal expansion in $PbTiO_3$-based perovskites." *Journal of the American Chemical Society*, vol. 130 4, pp. 1144–5, 2008. [Cited on page 13.]

[36] A. Say, O. Mys, A. Grabar, Y. Vysochanskii, and R. Vlokh, "Thermal expansion of $Sn_2P_2S_6$ crystals," *Phase Transitions - PHASE TRANSIT*, vol. 82, pp. 531–540, 07 2009. [Cited on page 13.]

[37] I. Shmytko, N. Afonikova, and V. Torgashev, "Anomalous states of the structure of $(NH_4)_2SO_4$ crystals in the temperature range 4.2–300 k," *Physics of the Solid State*, vol. 44, pp. 2309–2317, 12 2002. [Cited on page 13.]

[38] M. Azuma, W.-T. Chen, H. Seki, M. Czapski, S. Olga, K. Oka, M. Mizumaki, T. Watanuki, N. Ishimatsu, N. Kawamura, S. Ishiwata, M. Tucker, Y. Shimakawa, and J. Attfield, "Colossal negative thermal expansion in binio3 induced by intermetallic charge transfer," *Nature communications*, vol. 2, p. 347, 06 2011. [Cited on page 13.]

[39] P. A. Alekseev, J.-M. Mignot, E. V. Nefeodova, K. S. Nemkovski, V. N. Lazukov, N. N. Tiden, A. P. Menushenkov, R. V. Chernikov, K. V. Klementiev, A. Ochiai, A. V. Golubkov, R. I. Bewley, A. V. Rybina, and I. P. Sadikov, "Magnetic spectral response and lattice properties in mixed-valence $(Sm_{1-x}Y_x)S$ solid solutions studied with x-ray diffraction, x-ray absorption spectroscopy, and inelastic neutron scattering," *Phys. Rev. B*, vol. 74, p. 035114, Jul 2006. [Online]. Available: https://link.aps.org/doi/10.1103/PhysRevB.74.035114 [Cited on page 13.]

[40] J. Arvanitidis, K. Papagelis, S. Margadonna, K. Prassides, and A. Fitch, "Temperature-induced valence transition and associated lattice collapse in samarium fulleride," *Nature*, vol. 425, pp. 599–602, 11 2003. [Cited on page 13.]

[41] S. Margadonna, K. Prassides, M. Chondroudi, J. R. Salvador, and M. G. Kanatzidis, "Temperature-induced abrupt volume inflation in the mixed-valence ternary zintl phase $Yb_8Ge_3Sb_5$," *Chem. Commun.*, pp. 5754–5756, 2005. [Online]. Available: http://dx.doi.org/10.1039/B511606F [Cited on page 13.]

[42] Y. Long, N. Hayashi, T. Saito, M. Azuma, S. Muranaka, and Y. Shimakawa, "Temperature-induced AA intersite charge transfer in an a-site-ordered $LaCu_3Fe_4O_{12}$ perovskite," *Nature*, vol. 458, pp. 60–3, 04 2009. [Cited on page 14.]

[43] S. Xu, Y. Hu, Y. Liang, C. Shi, Y. Su, J. Guo, Q. Gao, M. Chao, and L. Er-Jun, "Negative thermal expansion of Ca_2RuO_4 with oxygen vacancies," *Chinese Physics B*, vol. 29, 04 2020. [Cited on page 14.]

[44] T. Qi, O. Korneta, S. Parkin, L. De Long, and G. Cao, "Negative volume thermal expansion via orbital and magnetic orders in $Ca_2Ru_1-xCrxO_4$ $(0 < x < 0.13)$." *Physical review letters*, vol. 105, p. 177203, 10 2010. [Cited on page 14.]

[45] T. Qi, O. Korneta, S. Parkin, J. Hu, and G. Cao, "Magnetic and orbital orders coupled to negative thermal expansion in mott insulators $Ca_2Ru_1-xMxO_4$ (m = mn and fe)," *Physical Review B*, vol. 85, 01 2012. [Cited on page 14.]

[46] X.-G. Zheng, H. Kubozono, H. Yamada, K. Kato, Y. Ishiwata, and C.-N. Xu, "Giant negative thermal expansion in magnetic nanocrystals," *Nature nanotechnology*, vol. 3, pp. 724–6, 01 2009. [Cited on page 16.]

[47] W.-H. Li, S. Y. Wu, C. Yang, A. Lai, K. Lee, H. Huang, and H. Yang, "Thermal contraction of Au nanoparticles," *Physical review letters*, vol. 89, p. 135504, 10 2002. [Cited on page 16.]

[48] Q. Li, H. Zhu, L. Zheng, H. Liu, Y. Ren, N. Wang, J. Chen, J. Deng, and X. Xing, "Local chemical strain in PtFe alloy nanoparticles," *Inorganic Chemistry*, vol. 57, 08 2018. [Cited on page 16.]

[49] J. Belo, A. Pires, I. Gomes, V. Andrade, J. Sousa, R. Hadimani, D. Jiles, Y. Ren, X. Zhang, J. Araujo, and A. Pereira, "Giant negative thermal expansion at the nanoscale in the multifunctional material $Gd_5(Si, Ge)_4$," *Physical Review B*, vol. 100, p. 134303, 10 2019. [Cited on page 16.]

[50] Z. Sun, X. Song, and L. Xu, "Effects of sintering temperature on microstructure, nitrogen deficiency and densification of spark plasma sintered $Mn_3Cu_{0.5}Ge_{0.5}N$," *Ceramics International*, vol. 37, pp. 1693–1696, 07 2011. [Cited on page 16.]

[51] D. T. Ho, S.-Y. Kwon, H. Park, and S. Kim, "Negative thermal expansion of ultrathin metal nanowires: A computational study," *Nano Letters*, vol. 17, 07 2017. [Cited on page 16.]

[52] G. Mo, Q. Cai, L. Jiang, W. Wang, K. Zhang, W. Cheng, X. Xing, Z. Chen, and Z. Wu, "Thermal expansion behavior study of Co nanowire array with in situ x-ray diffraction and x-ray absorption fine structure techniques," *Applied Physics Letters - APPL PHYS LETT*, vol. 93, 10 2008. [Cited on page 17.]

[53] Y. Wang, J. Yang, C. Ye, X. Fang, and L. Zhang, "Thermal expansion of Cu nanowire arrays," *Nanotechnology*, vol. 15, p. 1437, 08 2004. [Cited on page 17.]

[54] X. J. Xu, G. Fei, W. Yu, L. Zhang, X. Ju, X. Hao, D. Wang, and B. Wang, "In situ x-ray diffraction study of the size dependent thermal expansion of silver nanowires," *Applied Physics Letters*, vol. 89, pp. 181 914 – 181 914, 11 2006. [Cited on page 17.]

[55] O. Filatov and O. Soldatenko, "Size dependence of thermal expansion of silver nanowires," *Applied Nanoscience*, vol. 10, 06 2020. [Cited on page 17.]

[56] H. Zhu, Q. Li, C. Yang, Q. Zhang, Y. Ren, Q. Gao, N. Wang, K. Lin, J. Deng, J. Chen, L. Gu, J. Hong, and X. Xing, "Twin crystal induced near zero thermal expansion in SnO_2 nanowires," *Journal of the American Chemical Society*, vol. 140, 06 2018. [Cited on page 17.]

[57] W. Lee, R. Ji, U. Gösele, and K. Nielsch, "Fast fabrication of long-range ordered porous alumina membranes by hard anodization," *Nature materials*, vol. 5, pp. 741–7, 09 2006. [Cited on pages xvi, 22, and 24.]

[58] K. Nielsch, J. Choi, K. Schwirn, R. Wehrspohn, and U. Go, "Self-ordering regimes of porous alumina: The 10% porosity rule," *Nano Letters*, vol. 2, p. 677, 07 2002. [Cited on page 24.]

[59] P. Sourav and P. Sabyasachi, "Charge transfer vs. mass transfer mechanism in electrodeposition of copper thin films: A structural exploration," 2012. [Cited on pages xvi, 26, and 27.]

[60] X. Zhou, Y. Wang, Z. Liang, and H. Jin, "Electrochemical deposition and nucleation/-growth mechanism of NiNi multiple coatings," *Materials*, vol. 11, p. 1124, 07 2018. [Cited on page 27.]

[61] A. Bewick and B. Thomas, "Optical and electrochemical studies of the underpotential deposition of metals: Part ii. phase transitions and two-dimensional nucleation," *Journal of Electroanalytical Chemistry and Interfacial Electrochemistry*, vol. 85, no. 2, pp. 329–337, 1977. [Cited on page 28.]

[62] B. Scharifker and G. Hills, "Theoretical and experimental studies of multiple nucleation," *Electrochimica Acta*, vol. 28, pp. 879–889, 07 1983. [Cited on pages 28, 62, and 74.]

[63] X. Zhou, Y. Wang, Z. Liang, and H. Jin, "Electrochemical deposition and nucleation/-growth mechanism of NiNi multiple coatings," *Materials*, vol. 11, p. 1124, 07 2018. [Cited on pages 28 and 29.]

[64] L. Mendoza-Huizar, C. H. Rios Reyes, and M. Rivera, "Electrodeposition of cobalt nanoclusters from ammonical chloride solutions onto hopg electrodes. a kinetical and morphological study," *Journal of the Chilean Chemical Society*, vol. 62, pp. 3621–3626, 09 2017. [Cited on page 28.]

[65] M. Palomar-Pardavé, B. Scharifker, E. Arce, and M. Romero-Romo, "Nucleation and diffusion-controlled growth of electroactive centers: Reduction of protons during cobalt electrodeposition," *Electrochimica Acta*, pp. 4736–4745, 08 2005. [Cited on pages 28, 29, and 108.]

[66] C. Bran, E. Palmero, Z.-A. Li, R. Real, M. Spasova, M. Farle, and M. Vázquez, "Correlation between structure and magnetic properties in Co_xFe_{100-x} nanowires: The roles of composition and wire diameter," *Journal of Physics D Applied Physics*, vol. 48, p. 145304, 03 2015. [Cited on pages xvi, 31, 41, 42, 72, and 73.]

[67] N. Mansouri, N. Cherief, E. Chainet, F. Charlot, T. Encinas, S. Boudinar, B. Benfedda, L. Hamadou, and A. Kadri, "Electrodeposition of equiatomic FeNi and FeCo nanowires: Structural and magnetic properties," *Journal of Magnetism and Magnetic Materials*, vol. 493, p. 165746, 08 2019. [Cited on pages xvi, 31, 38, 39, 40, and 41.]

[68] W. Lu, P. Huang, C. He, and B. Yan, "Compositional and structural analysis of FeCo films electrodeposited at different temperatures," *International Journal of Electrochemical Science*, vol. 7, pp. 12 262–12 269, 12 2012. [Cited on page 31.]

[69] X. Zhou, J. Huang, F.-M. Zhang, Y. Zhao, Y. Zhang, and Y. Ding, "Iron-cobalt bimetal oxide nanorods as efficient and robust water oxidation catalyst," *Dalton Trans.*, vol. 46, 03 2017. [Cited on pages 31 and 99.]

[70] C. Sun, H. Wang, S. Ji, X. Wang, V. Linkov, X. Tian, L. Yao, J. Zhao, and R. Wang, "Layer-structured FeCo bihydroxide as an ultra-stable bifunctional electrocatalyst for water splitting at high current densities," *Sustainable Energy Fuels*, vol. 5, pp. 2747–2752, 2021. [Online]. Available: http://dx.doi.org/10.1039/D1SE00380A

[71] Q. Wu, T. Li, W. Wang, and Y. Xiao, "High-throughput chainmail catalyst FeCoFeCo nanoparticle for oxygen evolution reaction," *International Journal of Hydrogen Energy*, vol. 45, no. 51, pp. 26 574–26 582, 2020. [Online]. Available: https://www.sciencedirect.com/science/article/pii/S0360319920325854

[72] X. Fu, Y. Liu, X. Cao, J. Jin, Q. Liu, and J. Zhang, "FeCoFeCo embedded graphene as high performance catalysts for oxygen reduction reaction," *Applied Catalysis B: Environmental*, vol. 130-131, pp. 143–151, 2013. [Online]. Available: https://www.sciencedirect.com/science/article/pii/S0926337312005073 [Cited on page 31.]

[73] C. Li, M. Wu, and R. Liu, "High-performance bifunctional oxygen electrocatalysts for zinc-air batteries over mesoporous Fe/Co−N−C nanofibers with embedding feco alloy nanoparticles," *Applied Catalysis B: Environmental*, vol. 244, pp. 150–158, 2019. [Online]. Available: https://www.sciencedirect.com/science/article/pii/S0926337318310890 [Cited on page 31.]

[74] N. Arroyo-Curras, J. Hall, J. Dick, R. Jones, and A. Bard, "An alkaline flow battery based on the coordination chemistry of iron and cobalt," *Journal of the Electrochemical Society*, vol. 162, pp. 378–383, 01 2015. [Cited on page 31.]

[75] Y. Ustinovshikov and B. Pushkarev, "Ordering and phase separation in alloys of the FeFe system," *Journal of Alloys and Compounds - J ALLOYS COMPOUNDS*, vol. 424, pp. 145–151, 11 2006. [Cited on pages xvi, 32, and 57.]

[76] D. Nam, S. Kim, Y. Jeon, and Y. K. Kim, "Microstructure and magnetic properties of CoFe nanowires and helical nanosprings," *IEEE Transactions on Magnetics*, vol. PP, pp. 1–1, 05 2017. [Cited on page 37.]

[77] A. Esmaeily, D. M. Venkatesan, A. S. Razavian, and J. M. D. Coey, "Diameter-modulated ferromagnetic CoFe nanowires," *Journal of Applied Physics*, vol. 113, 03 2013. [Cited on pages xvi, 37, and 38.]

[78] G. Han, B. Zong, P. Luo, and Y. Wu, "Angular dependence of the coercivity and remanence of ferromagnetic nanowire arrays," *Journal of Applied Physics*, vol. 93, pp. 9202–9207, 06 2003. [Cited on page 39.]

[79] H. Su, S.-l. Tang, R.-l. Wang, Y.-q. Chen, C. Jia, and Y.-w. Du, "$Fe_{48}Co_{52}$ alloy nanowire arrays: Effects of magnetic field annealing," *Chinese Journal of Chemical Physics*, vol. 22, p. 82, 03 2009. [Cited on pages xvi, 40, and 41.]

[80] [Cited on pages 53, 96, and 102.]

[81] T. Du, B. Varaprasad, Z. Guo, A. J. Gellman, J.-G. J. Zhu, and D. E. Laughlin, "Tem-based study of oxidation of FeCo high moment alloy at elevated temperatures," *Journal of Magnetism and Magnetic Materials*, vol. 539, p. 168347, 2021. [Cited on page 57.]

[82] A. Monshi, M. R. Foroughi, and M. Monshi, "Modified scherrer equation to estimate more accurately nano-crystallite size using xrd," *World Journal of Nano Science and Engineering*, vol. 2, pp. 154–160, 09 2012. [Cited on page 57.]

[83] F. De Jesús, A. Bolarín-Miró, C. Cortés-Escobedo, G. Torres-Villaseñor, and P. Vera, "Structural analysis and magnetic properties of FeCo alloys obtained by mechanical alloying," *Journal of Metallurgy*, vol. 2016, pp. 1–8, 07 2016. [Cited on pages 57 and 58.]

[84] I. Ohnuma, H. Enoki, O. Ikeda, R. Kainuma, H. Ohtani, B. Sundman, and K. Ishida, "Phase equilibria in the Fe−Co binary system," *Acta Materialia*, vol. 50, p. 379, 01 2002. [Cited on page 57.]

[85] T. Sourmail, "Near equiatomic feco alloys: Constitution, mechanical and magnetic properties," *Progress in Materials Science*, vol. 50, no. 7, pp. 816–880, 2005. [Online]. Available: https://www.sciencedirect.com/science/article/pii/S0079642505000204 [Cited on page 59.]

[86] Y. S. T. C. Y. Ho, "Properties of selected ferrous alloying elements," 1981. [Cited on pages xx, 97, and 116.]

[87] K. Thurnay, "Thermal properties of transition metals," May 1998. [Cited on pages xx, 97, and 116.]

[88] K. Li, Y. Li, W. Peng, G. Zhang, F. Zhang, and X. Fan, "Bimetallic iron–cobalt catalysts and their applications in energy-related electrochemical reactions," *Catalysts*, vol. 9, no. 9, 2019. [Online]. Available: https://www.mdpi.com/2073-4344/9/9/762 [Cited on page 99.]

[89] T. Lopes, L. Andrade, H. Aguilar, and A. Mendes, "Characterization of photoelectrochemical cells for water splitting by electrochemical impedance spectroscopy," *International Journal of Hydrogen Energy*, vol. 35, 10 2010. [Cited on page 99.]

[90] H. Zhang, Y. Long, E. Niu, X. P. Shao, J. Shen, F. X. Hu, J. R. Sun, and B. G. Shen, "Influence of particle size on the hydrogenation in $La(Fe,Si)_{13}$ compounds," *Journal of Applied Physics*, vol. 113, no. 17, p. 17A911, 2013. [Online]. Available: https://doi.org/10.1063/1.4794975 [Cited on page 100.]

[91] M. Krautz, K. Skokov, T. Gottschall, C. Teixeira, A. Waske, J. Liu, L. Schultz, and O. Gutfleisch, "Systematic investigation of mn substituted $La(Fe,Si)_{13}$ alloys and their hydrides for room-temperature magnetocaloric application," *Journal of Alloys and Compounds*, vol. 598, p. 27–32, 06 2014. [Cited on page 100.]